ScuDo
Scuola di Dottorato ~ Doctoral School
WHAT YOU ARE, TAKES YOU FAR

Doctoral Dissertation
Doctoral Program in Physics (30^{th}cycle)

Passive shielding of space radiation for human exploration missions

Simulations and Radiation Tests

By

Martina Giraudo

******

Supervisor(s):
Prof. Laura Gozzelino

Doctoral Examination Committee:
Dr. Emanuele Scifoni, Trento Institute for Fundamental Physics and Applications
Dr. Michael Sivertz, Brookhaven National Laboratory
Prof. Roberto Cirio, Università di Torino
Prof. Dario Daghero, Politecnico di Torino
Prof. Andrea Lavagno, Politecnico di Torino

Politecnico di Torino
2018

Declaration

I hereby declare that, the contents and organization of this dissertation constitute my own original work and does not compromise in any way the rights of third parties, including those relating to the security of personal data.

Part of this thesis' work has been done at Thales Alenia Space, using Thales Alenia Space infrastructures and in the framework of the ROSSINI2 study.

The ROSSINI2 study has been supported by European Space Agency (ESA) under the contract RFP IPLPTE/LF/mo/942.2014 and with the generous support of NASA and BNL, providing beam time at the NSRL facility.

The following publications/book chapters have been submitted as part of this thesis work:

- Contribution to two chapters of the book "Space Safety and Human Performance", Editors: Barbara Kanki Jean-Francois Clervoy Gro Sandal, Editor-in-Chiefs: Tommaso Sgobba, Hardcover ISBN: 9780081018699, Imprint: Butterworth-Heinemann, Published Date: 20th October 2017
- 2 additional publications, written with the ROSSINI2 team, will be submitted

Martina Giraudo
2018

* This dissertation is presented in partial fulfillment of the requirements for **Ph.D. degree** in the Graduate School of Politecnico di Torino (ScuDo).

I would like to dedicate this thesis to my family, who made me who I am.

Acknowledgements

First of all I would like to sincerely thank my tutor, Laura Gozzelino, for all the support and advices she gave me. I appreciate all her continuous help, ideas and time, which contributed to make my Ph.D possible.

This thesis would not have been possible without Emanuele Tracino and his contribution to getting me where I am today. I would like to sincerely thank him, together with Roberto Destefanis and Cesare Lobascio, without their trust and support I would not have found myself involved in the ROSSINI and ROSSINI2 projects.

Then I want to extend my thanks to several scientists, who contributed to the work presented in this thesis. Thanks to Uli Weber and Chris Schuy for their infinite patience with me. To Chiara La Tessa for the so many skype calls she had to answer during these 3 years and to Marco Durante, for making ROSSINI possible. To Cary Zeitlin and Tatsuhiko Sato for all their valuable advises. To Alessandra Menicucci for believing that an inexperienced young graduate could take the lead of the project and to Giovanni Santin for all the reviews and suggestions he gave to the ROSSINI2 collaboration.

Finally, thanks to the NASA Space Radiation Laboratory (NSRL) staff at BNL, I will always remember my permanence there with a smile.

Abstract

Space radiation is one of the main showstoppers for human exploration of deep space. When leaving the protection provided by Earth's atmosphere and magnetic field, the astronaut crew find themselves immersed into a complex radiation field, originated by the interaction of different high-energy radiation sources with the spacecraft's walls, and characterized by many particle species with a broad range of energies. The biological effects of the long-term radiation exposure is largely uncertain and could give rise not only to late solid cancers and leukemia, but also to early effects to cardiac and nervous tissues, possibly undermining mission success.

An available countermeasure to defend the astronauts from radiation is passive shielding, i.e. the interposition of shielding materials between the radiation sources and the exposed subjects. However, the majority of space radiation is practically impossible to completely stop: the high energetic particles constituting the space environment have the capability to penetrate several meters of materials, generating a harmful component of secondary particles, further contributing to the radiation dose.

The ability of a material to attenuate the incoming space radiation and the nature of the generated secondary particles largely depends on the traversed material itself, in particular on the ratio between its charge and mass atomic numbers, Z/A. The lower is this ratio, the higher the material's capability to attenuate the incoming radiation will be, both through electromagnetic and nuclear interactions.

While the radiobiology community is focusing on the biological effects, radiation physics is trying to lower uncertainties characterizing the radiation interactions with materials, performing radiation measurements of various nature.

In this framework I focused my PhD activity on the study of materials which could be used in space as shielding layers and multipurpose structures have been evaluated and selected under different criteria. At first, their ability to shield different

kinds of space radiation were calculated with the aid of 1D Monte Carlo simulations, also followed by an evaluation of their structural and thermal proprieties, cost, availability and compatibility with the space environment. Simulations, in particular, were performed both to support the material selection process both to produce guidelines for design.

The selected materials were then procured to be tested under different radiation beams and different set-ups, in single and multi-layers configurations, in an attempt to reproduce space exposure conditions. At the same time, the radiation tests have been reproduced by means of Monte Carlo simulations, to compare the experimental results and the simulations' outputs, confirming the codes' ability to reproduce radiation measurements involving High Z-number and high Energy (HZE) particles. For some materials, suggestions were provided on which nuclear model was better reproducing the data.

The performed experimental campaign suggested that a candidate shielding material suitable for Galactic Cosmic Rays (GCR) should be tested with at least two beams with different characteristics, since the results indicated that some materials good at shielding 972 MeV/nuc ^{56}Fe ions performed very poorly when irradiated with high energetic alphas. Furthermore, among the material types included in this investigation work, Lithium Hydride resulted the best option to stop space radiation, when only radiation shielding properties are considered.

At the end of the experimental campaigns, on the basis of the test results, a 3D simulation activity has started and is still on-going and a modular space habitat model has been created. Monte Carlo simulations have been carried out, reproducing different Moon exposure scenarios with the goal of calculating crew radiation exposure during a Moon surface mission. This work reports results only for a standard aluminum habitat, with only Moon soil used as shielding material. However, future simulations will include Lithium Hydride and possibly others materials as shielding layers, to evaluate their effectiveness in reducing the dose in a realistic exposure scenario. Preliminary results show that even with a heavily shielded spacecraft (the habitat taken in consideration in this work is providing from every direction at least 30 g/cm^2 of aluminum equivalent) radiation exposure approaches values close to the existing annual radiation exposure limits.

Part of this thesis' work was done at Thales Alenia Space, using Thales Alenia Space infrastructures and in the framework of the ROSSINI2 study. The ROSSINI2

study has been supported by European Space Agency (ESA) under the contract RFP IPLPTE/LF/mo/942.2014 and with the generous support of NASA and BNL, providing beam time at the NSRL facility.

Contents

List of Figures

List of Tables

Chapter 1

Planetary and interplanetary radiation environment

Part of the review done in the following sections has been published in November 2017 as a chapter of the book *"Space Safety and Human Performance"* by Barbara G. Kanki, Jean-Francois Clervoy and Tommaso Sgobba.

1.1 Introduction

The high level of radiation met during a deep space exploration mission makes the radiological risk one among the most dangerous issues which could lead the astronauts to diseases or death, electronics to malfunctioning and spacecraft materials to deteriorated conditions. Furthermore, while on Earth generally the radiation cancer risk comes from the well known low-Linear Energy Transfer (LET), the long term health effects of High Z number and high Energy (HZE) space ions are still unclear so that large uncertainties characterize the subject.

During space exploration missions, spacecraft and crew will be exposed to three main natural sources of radiation: localized trapped particle belts, periodic occasional Solar Particle Events (SPEs) and background Galactic Cosmic Rays (GCRs). Each contribution is characterized by different radiation types and energies, and undergoes different interactions while traversing space materials, electronics and biological tissues, leading therefore to different effects.

Additionally, the radiation environment is modified when traversing materials, also as a function of the material itself. This means that different spacecraft structures and habitats, exposed to the same external radiation field, will probably have different internal radiation fields.

Predicting the total damage to the crew consequently becomes a very complicated process and not always feasible with sufficient accuracy, dealing with mixed complex radiation field.

In the following sections a brief overview of the radiation space environment of interest for human space exploration missions is given, followed by a description of different possible exposure scenarios.

1.2 Space radiation environment

The space radiation environment of interest for the scope of this work is characterized by two main sources of radiation: periodic SPEs and background GCRs. Trapped particle belts, the third source of radiation dose in space are also described for the sake of completeness.

1.3 Radiation belts

Trapped radiation belts, also referred as Van Allen radiation belts, consist of energetic charged particles, mainly protons and electrons, trapped and confined in toroidal regions by the Earth's magnetic field lines. These regions are ranging from altitudes of about 1000 up to 60,000 kilometers above the Earth's surface.

Different processes can origin trapped particle belts. Albedo neutrons, generated by cosmic rays' interaction with the atmosphere, decay into protons, while electrons are injected as the result of geomagnetic storms reaching Earth.

Once charged particles are produced or have reached the Earth's magnetic field, they gyrate and travel along the field lines conserving their magnetic moments. Since the magnetic moment of a particle remains constant when the particle is moving into a magnetic field, when the charged particle is gyrating and moving towards regions with higher magnetic field (the Earth's magnetic field poles in this case), the

component of velocity parallel to the direction of travel decreases, until the particle stops and is bounced back. This effect, called magnetic mirroring, is the cause of particles' trapping in magnetic fields.

Two main electron belts exist around the Earth, the inner and the outer belt, separated by the so called slot region, and peaking at about 3000 km and 25,000 km, respectively. Electron energies vary from few keV up to 10 MeV.

A single proton belt is instead found, with its peak at around 3000 km of altitude, with proton energies between 100 keV and several hundred MeV.

Trapped radiation belts are usually modeled as static particle distributions, however they have temporal and spatial variations in response to geomagnetic storms and solar particle events, and because of the day/night asymmetry in the planetary magnetic field, respectively. A region of lower magnetic field intensity is found over the South Atlantic, due to the magnetic and geographical poles displacement, where charged particles are able to reach lower altitudes. This singularity is called South Atlantic Anomaly (SAA) and spacecraft crossing this region receive higher doses of radiation [10].

Nowadays the old radiation belt models made by National Aeronautics and Space Administration (NASA), AP-8 and AE-8 [11], which completely cover the region of radiation belts, are still used for engineering applications. They are static models and consider only variations due to the solar cycle. Others existing models, for electrons and protons, listed according to their publication date, are:

- CRRESELE [12]
- update of AE-8 MIN
- IGE-2006/POLE [13]; [14]
- AE-9 [15]
- CRRESPRO [16]
- low altitude model based on SAMPEX/PET data (for solar minimum conditions) [17]
- AP-9 [15]

Figure 1.1 and Figure 1.2 show the distributions of electrons >1 MeV and protons > 10 MeV, respectively, at 500 km of altitude, as predicted by NASA models. The higher fluence above the SAA can be clearly noticed.

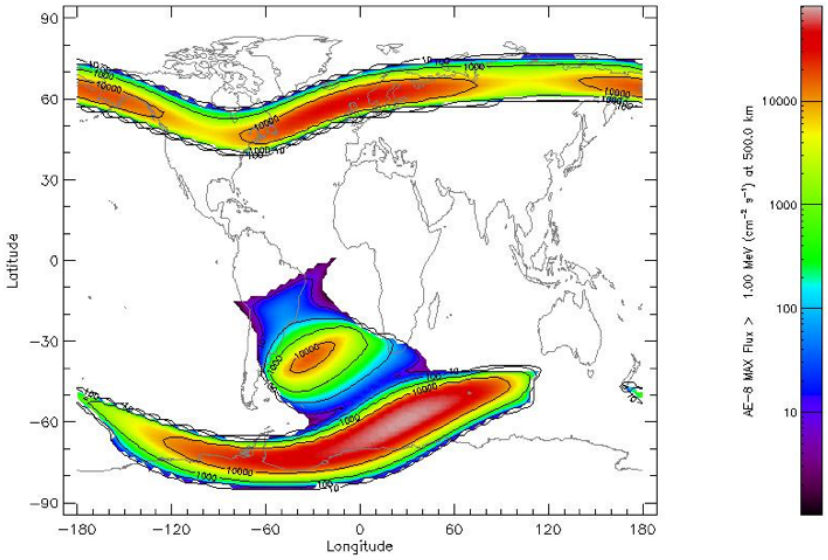

Fig. 1.1 AE-8 MAX Flux > electrons 1 MeV ($cm^{-2}s^{-1}$) at 500 km - Data obtained from the Spenvis ESA tool.

Trapped particle belts are not only Earth's prerogative. They have been detected also around other planets or satellites with a magnetic field intense enough to trap charged particles. Jupiter, for instance, has an extensive magnetosphere and, consequently, its own radiation belts, which also interact with Jupiter's satellites. The magnetosphere is about 2 orders of magnitude larger than Earth's and on the night side it extends to the orbit of Saturn [18]. The resulting particle belts are influenced by the satellites orbiting around the planet and at Europa's orbit, which is located inside Jupiter's radiation belt, high radiation fluxes are recorded. These belts could seriously affect space missions, such as the JUpiter ICy moons Explorer (JUICE) mission, selected by the European Space Agency (European Space Agency (ESA)) in May 2012, and investigating three of Jupiter's Galilean satellites, Ganymede, Europa and Callisto [19].

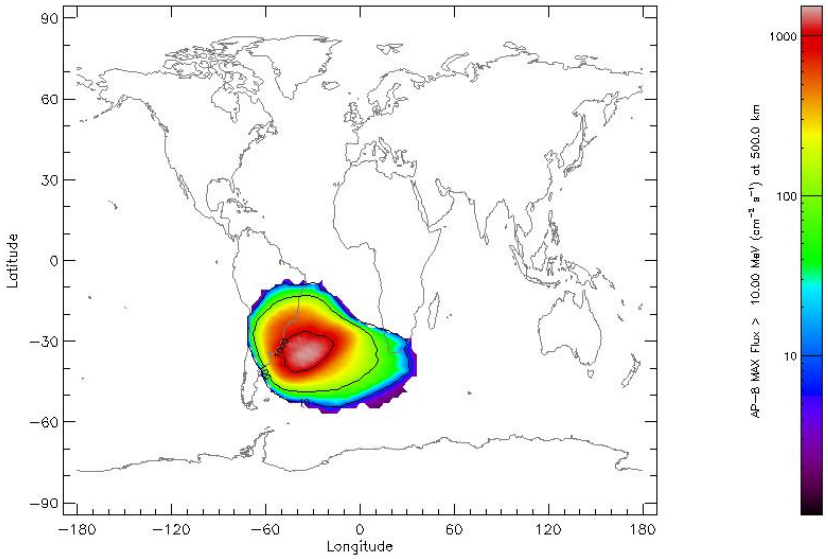

Fig. 1.2 AP-8 MAX Flux protons > 10 MeV ($cm^{-2}s^{-1}$) at 500 km - Data obtained from the Spenvis ESA tool.

1.4 Solar Particle Events

SPEs feature a large amount of particles emitted by the Sun and then accelerated by magnetic fields. They have been recorded at Earth since 1942 [20].

Many of the large SPEs can be associated with solar flares, which consist in sudden brightening of the chromosphere, but only about half of them are certainly associated with solar flares. Coronal Mass Ejections (CME) could also be source of very large SPEs. Regardless of their origin, in the worst cases, billions of tons of matter are emitted from the Sun within few hours. The emitted particles then propagate interacting with the solar wind, along the interplanetary magnetic field lines.

Depending on the region of the Sun originating the particle emission, some SPEs may results invisible from Earth: for this reason, missions in deep space will need to be equipped with particles detectors (x-rays and particle monitors) to be able to detect the SPE onset independently from Earth based observations [20].

SPEs can potentially lead to high fluxes and fluences of protons in the energy range from 10s to 100s of MeV. Protons are accompanied by heavy ions too.

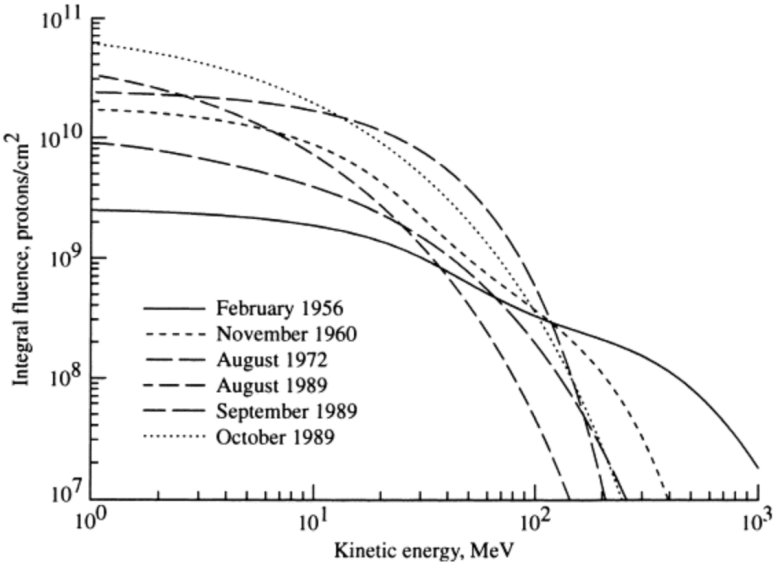

Fig. 1.3 Proton fluence spectra of the largest recorded SPEs [1].

Since the space age has started, three main large SPEs have been observed: February 1956, August 1972 and October 1989. Their flux, limited to particles with energy higher than 30 MeV, was calculated to be greater than 10^9 particles > 30 MeV cm$^{-2}s^{-1}$: in few days the total fluence of particles with energies above 30 MeV as an entire solar cycle of exposure to background GCRs was delivered. If a human interplanetary mission had taken place at that time without enough shielding, the consequent exposure would have led to serious health effects to the crew, including acute radiation sickness and, ultimately, death.

The spectra of the most energetic SPEs ever recorded are shown in Figure 1.3, from [1].

On rare occasions, very energetic events can be detected at Earth ground level by sudden increases in neutron radiation counters. For instance, on February 23, 1956, a neutron count rate 3600 times the background one was recorded as a strong SPE hit Earth, reported in Figure 1.4. This particular SPE spectrum, however, is not usually considered reliable because not coupled with satellite measurements, as for later events.

Investigations on anomalously hard spectra SPEs have also been performed by different groups, studying the ice core data from Antarctica and records of ^{14}C levels in tree rings [21]. The existence of a large cosmic event in AD774 or AD775 has

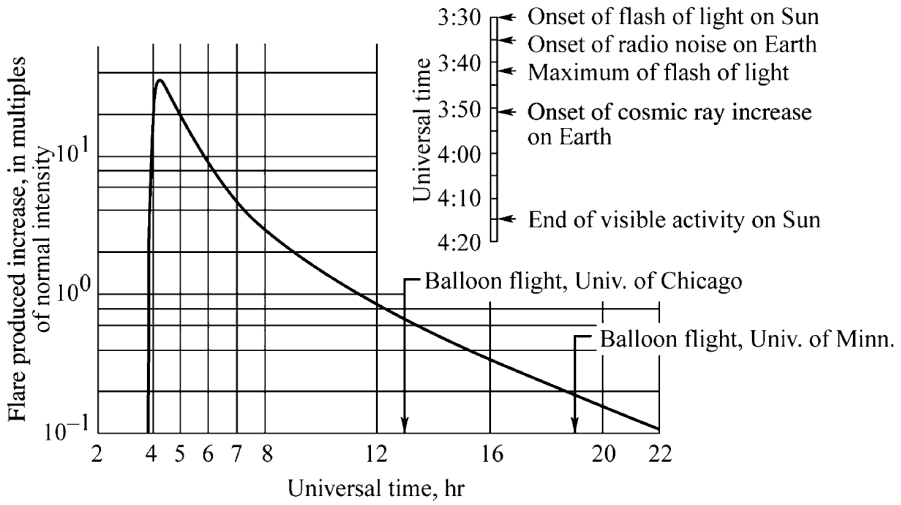

Fig. 1.4 Ground level neutron monitor event seen at Durham, NH on February 23, 1956 [2].

been recently confirmed. Such event would have had a proton (>30 MeV) fluence of about 4.5 x 10^{10} cm^{-2}, with a hard spectrum similar to the one of the February 1956 event [22].

It is reasonable to expect that such extreme events may occur again: their impact on space systems and on powered ground structures could be disastrous.

SPEs occur most frequently during periods of solar maximum of the solar cycle; however no systematic pattern has been discovered so far to predict them. Crew and space systems exposure to this kind of events is difficult to foreseen, due to the large variability in spectra distributions. Their particle and energetic spectra can generally be described with power law and exponential forms. Usually a first wave of energetic particles arrives at a given point in space, almost at the speed of light, followed then by a slower and more intense wave.

SPEs deliver most of the radiation total dose to an average shielded spacecraft, causing biological effects in humans and posing a hazard to solar cell and electronics present on board. A significant number of spacecraft damages and malfunctioning occurred during missions has been clearly tracked to such events.

August 72 event, as can be noticed in Figure 1.3, has been characterized by a very high proton fluence in the region 70-100 MeV, which can potentially contribute to radiation dose to Blood Forming Organs (BFO) for low shielded spacecraft, therefore resulting in a potential life-threatening hazard.

Since SPEs can be partially or totally shielded by the Earth magnetic field, they are mainly a concern for planetary (Moon and Mars) and interplanetary space missions. However, as they propagate in the Earth's magnetic field they can also affect lower orbit satellites, space systems and even powered systems on ground, if intense enough. For the International Space Station (ISS) orbit, they could be lethal for astronauts involved in Extra Vehicular Activities (EVA), if they have not enough time to reach a designated shelter providing adequate shielding.

Solar protons penetration in the Earth's magnetosphere is a function of their magnetic rigidity (particle momentum divided by its charge). At polar latitudes, some solar particles can reach the lower portion of the atmosphere, at latitudes in the range of 55-65 degrees most of the particles are stopped, while below that latitude only the most energetic particles can penetrate.

As regards the radiobiological impacts, SPEs have the potential to give rise to concerns of both acute and chronic effects for interplanetary manned missions.

1.5 Galactic Cosmic Rays

GCR! (**GCR!**)s are the main showstopper to space exploration: this radiation component is almost impossible to shield and it is characterized by very high values of LET. This leads to almost unavoidable harsh and less known effects on biological systems.

GCRs are a continuous flow of charged particles reaching the solar system from outside the heliosphere and arriving at Earth's orbit with an isotropic distribution.

The majority of them is constituted by atomic nuclei, whose orbital electrons have been stripped off, and the remaining 2% by electrons and photons, as measured by different balloons and space missions

Their origin is still a mystery: most likely they have been accelerated in blast waves of supernova remnants and have been traveling for several millions of years before reaching the solar system. The very high energy part may arrive from outside our Galaxy, generated during gamma ray bursts, quasars or from active galactic nuclei [3].

The atomic component ranges from hydrogen to uranium and their energies range from 10 MeV/nuc up to 10^{12} MeV/nuc. In particular, they are approximately comprised by 85% of hydrogen, 14% of helium and the residual 1% of heavy ions, the so-called High Energy High Z number (HZE) particles. Figure 1.5 reports the cosmic ray differential energy spectra[1] measured for hydrogen, helium, carbon and iron ions in different solar conditions, as taken from [3].

When approaching Earth, like for SPEs, GCRs start interacting with Earth's atmosphere and magnetic field and their ability to penetrate the magnetosphere is therefore limited. As the particle ability to penetrate the magnetic field is determined by its magnetic rigidity, for each approaching direction to each point an onset value of this parameter exists, called geomagnetic cutoff, below which the particle cannot reach that point. This phenomenon attenuates the GCRs flux, as well as SPEs, reaching Earth.

During magnetic storms, the geomagnetic cutoff is modified, generally decreasing, so that more particles can reach a certain point compared with magnetic quiet conditions. Additionally, at higher latitudes, GCRs access to Earth is higher.

These behaviors have been known since the Thirties, thanks to experiments in which ion chambers were flown on air balloons at different latitudes and neutrons monitors were places in different points at Earth's surface.

Inside the heliosphere, the solar activity can modify the GCRs spectra below 10 GeV/nuc, thanks to the spiral heliospheric magnetic field carried by the solar wind. As the solar activities undergoes its 11-years cycle, the GCRs flux is varying, anti-correlated with the number of sunspots and the solar cycle. In particular, the GCRs flux is seen to be at its maximum during solar minimum periods [23], with the low energy part being subjected to a variation of a factor 2. Solar modulation can be noticed in the measurements reported in Figure 1.5 [3]: observing H, He and Fe it is possible to see two sets of data for each ion, each corresponding to solar minimum/maximum condition.

Solar modulation reaches its maximum for protons around 100 MeV, while it is still about 20-25% at energies of 4 GeV/nuc [24].

[1] The differential energy spectra in this thesis work is expressed as the number of particles dN in the energy range from E to $E + dE$ transversing a unit surface area dA and arriving from direction Ω within a solid angle $d\Omega$ in a time interval dt. It is therefore expressed in the following units: $m^2 s^1 sr^1 (MeV/nuc)^1$

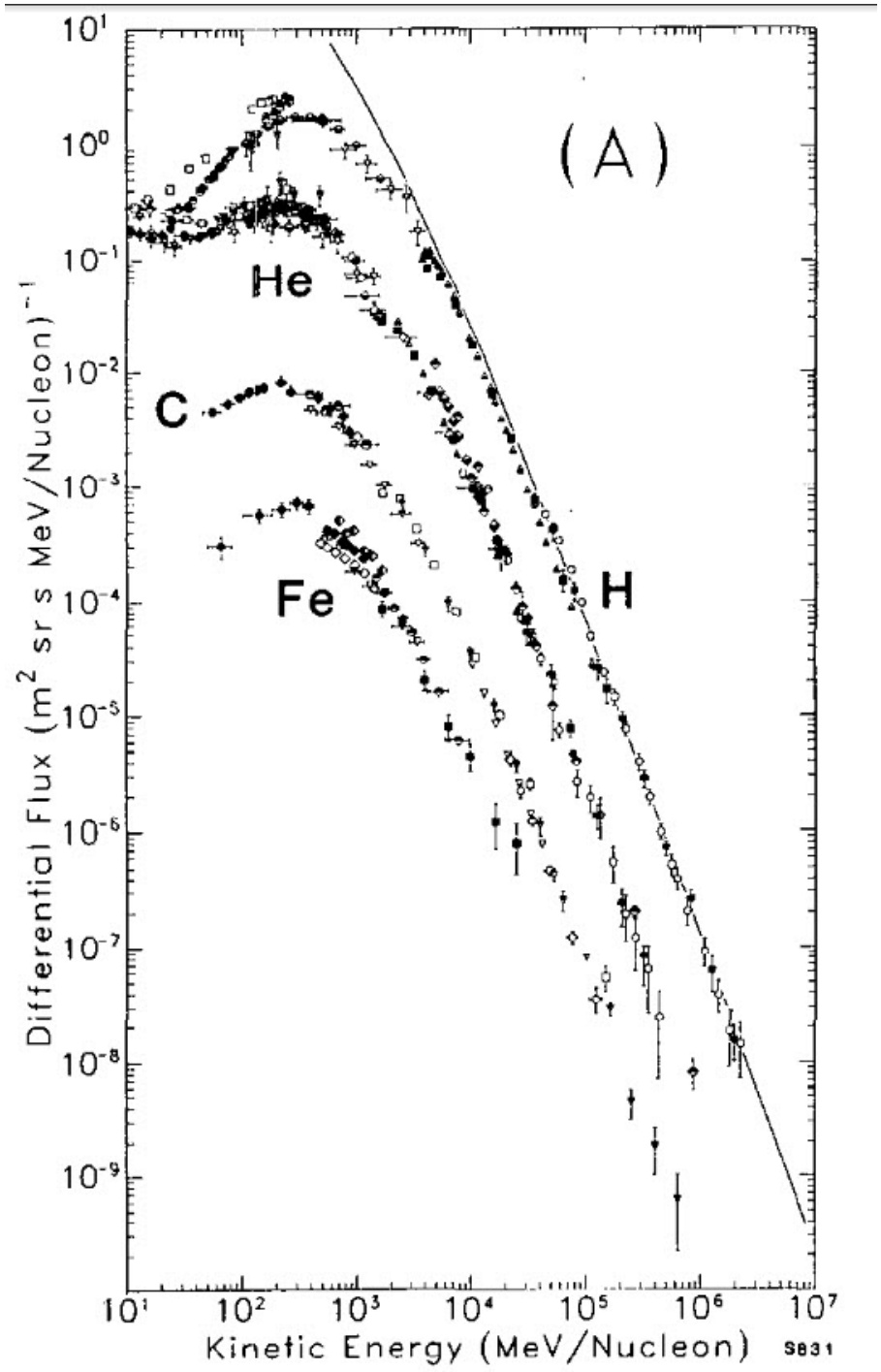

Fig. 1.5 Cosmic ray energy spectra measured for the elements H, He, C, and Fe in different solar conditions, as reported in [3].

The intensity of the GCRs flux slowly increases with the radial distance from the center of the heliosphere. A diffusion process takes place, where the incoming GCRs charged particles interact with the outward propagating solar wind particles, whose intensity depends on the solar activity and decreases as the distance from the Sun increases.

For instance, for 300 MeV/nuc Helium the increase is about 12% AU^{-1}, where AU stands for Astronomic Units, [25], leading to an overall increase of the GCRs fluence rate of about 5% at the orbit of Mars [26].

Forbush decreases (FD), probably linked to interplanetary CMEs, interplanetary shocks and co-rotating interaction regions, are extreme examples of the influence of solar activity on the GCRs flux: the GCRs flux intensity suddenly decreases in few hours, to be then back again to nominal values in about one week.

A certain number of theoretical models have been developed since the discovery of GCRs to describe their behavior and trend. New models are based on the standard diffusion-convection theory of solar modulation and differ from each other mainly in their definition of the local interstellar spectrum.

The models reproducing GCRs distribution most used in the engineering domain are the CREME96 model [27] and the ISO-15390 model [28]. Current models are believed to have uncertainties of about 25% [20].

At near-Earth interplanetary orbit the GCRs flux is about 4 particles $cm^{-2}s^{-1}$ in solar minimum periods [10]. Observing the low value of GCRs flux, it is therefore clear that GCRs doses exposure not pose hazards for acute effects but their chronic effects are the real issues to be addressed to make human space exploration possible for long periods of time.

Unfortunately, high level of uncertainties exists when dealing with biological effects of this kind of radiation environment, due to unknown biological response in human beings and to difficulties into reproducing this kind of exposure.

Many other relevant biological data are indeed still needed. There is in fact a large amount of studies on the effects of low-LET radiation (such as photons and neutrons) because of the Life Span Studies (LSS) following for decades the Japanese atomic bombs survivors, but on the other hand no data on GCRs long term exposure exist for humans.

GCRs exposure could lead to different kinds of effects, not only stochastic effects (i.e. cancer and leukemia), but also cardiovascular and neurological effects. Considering their high energies, it follows that is very difficult, if not practically impossible, to shield this radiation component. Not only high energy GCRs are usually not stopped when going through thin spacecraft walls, but they produce showers of secondary particles, too.

Secondary radiation, mainly consisting in neutrons and high speed charged fragments, is very difficult to stop. Neutrons, having no charge, can travel many meters inside materials.

For all these reasons, GCRs are one of the main obstacles standing in the way of long duration human interplanetary travels.

1.6 Induced secondary radiation

As mentioned in the previous section, when primary radiation particles found in space traverse spacecraft materials and interact with matter, they can generate harmful secondary radiation through nuclear and electromagnetic processes. Sometimes the results of this interaction produce more biologic damage than parent primary radiation. For instance, GCRs primary ions in the interaction with materials can break up into smaller and faster fragments which can then penetrate deeply inside matter. The spectra of this secondary radiation is largely variable and depends on the source and on the interposed materials.

Generated neutrons, which have no charge, are very penetrating radiation, difficult to shield, and they are thought to be a major contribution to exposures in lunar or Martian habitat [29]. Neutrons can moreover produce additional charged secondary particle interacting with nuclei. They are an important source of exposure not only for manned missions but for scientific missions too, where they can effectively contribute to the total dose and generate detector background noise.

Also leptons, mesons and photons are produced and transported in a GCRs environment and they affect the overall dose predictions [30].

Accurate knowledge of involved physics processes is necessary to fully determine the secondary radiation field created inside a habitat from the interaction of primary radiation with the spacecraft materials. A lot of data on cross sections are missing for

many species of ions into materials and a recent review of existing nuclear physics experiment data for space radiation can be found in [31].

Chapter 2 includes a dedicated section about the main involved physics processes and radiation effects.

1.7 Radiation exposure scenarios

In the following paragraphs, different exposure scenarios of interest for space exploration are described.

As regards the Near Earth Orbit (NEO), the energy distribution of particles depends on the orbit inclination and the spacecraft altitude. In interplanetary space the distance from the Sun determines the solar proton flux intensity, in the case of SPEs, and the GCRs attenuation, influenced by the magnetic field intensity.

On planets and their satellites, about half of the particles' flux is shielded by the planet itself, but additional secondary radiation is generated by the interaction with the planet's surface.

If an atmosphere or a magnetic field is present, additional protection will be provided, too. Finally, for bodies surrounded by a magnetic field, additional exposure will arrive from charged radiation trapped in particle belts.

1.7.1 Low Earth Orbit

Low Earth Orbit (LEO) refers to orbits with altitude ranging from 300 to 1600 km, where particles of different origin are encountered: protons, electrons, heavy ions, neutrons and others.

For low altitude LEO orbit, such as for the ISS, whose orbit altitude ranges from 360 and 440 km, the radiation environment includes electrons, protons, ions and secondary neutrons. In addition, inside the ISS, the interaction of the external environment with the station walls produces a secondary radiation field, whose properties vary as a function of the position inside the ISS, depending on the kind and the amount of material available.

Peaks in radiation exposure will be registered when traversing the SAA. As regards equatorial orbits, the main contribution to radiation exposure will be given by passages through the SAA.

As the orbit altitude or inclination increases, so does the SPEs and GCRs contribution to the dose.

1.7.2 Beyond LEO

In deep space, no shielding or attenuation comes from the planets and their magnetic fields and atmospheres. SPEs and GCRs will hit the spacecraft with fluxes depending on the position in the solar system.

The measurements of the Radiation Assessment Detector (RAD) which flew on the Mars Science Laboratory (MSL) unmistakably showed that radiation will be a major health hazard for interplanetary missions. MSL recorded an average dose rate on the transit to Mars of 0.46 mGy/day and a dose-equivalent rate of 1.84 mSv/day [32]. In a 2 years' period (2012 – 2013), the measured dose due to GCRs was the greatest part of the total dose, while SPEs were estimated to contribute only to 5% of the total dose during the trip to Mars.

Considering the fluxes of the different radiation sources, during an interplanetary mission in deep space every cell nucleus in the crew's bodies will be hit by a proton or secondary electron (generated by the interaction of GCRs with the body itself) every few days, and by a GCR ion about once a month [33].

It is straightforward understanding that this leads to a very high risk of harmful radiation effects. Being the incident HZE particles highly ionizing, these interactions could result into serious harm to the hit cell.

1.7.3 Moon scenario

Moon is considered to be the necessary exploration step to be enable long duration human presence in deep space.

The Moon surfaces is an aggressive and intimidating environment to live and work. The lack of atmosphere (it is essentially very thin) results in no protection from solar wind, radiation and micrometeoroids, causing the presence of a very thin

layer of a charged dust everywhere on the surface. The so created charged dust must be prevented from entering habitats and vehicles, therefore requiring peculiar design adjustments to be included in the habitat design, such as airlocks and dust removal systems.

Another effect of the atmosphere privation is huge temperature differences between lunar dawn and lunar noon, from about -230 °C to about 125 °C [34].

Seismic experiments have been carried out to measure seismic activities on the Moon, assumed to be seismically stable compared to Earth [35].

Nevertheless, exposure to space radiation is probably the most limiting factor to the long-term human permanence on the Moon.

Base locations should be carefully chosen, and many factors will have to be taken in consideration, such as:

- Orbit accessibility
- Lighting requirements
- Surface aspects
- Resources utilization (eventually presence of extractable elements)
- Radiation protection (higher protection for instance in basins)

Furthermore, all materials used to build structures on the Moon should be able to withstand:

- Extreme temperatures variations
- Debris impacts
- Intense sunlight exposure (no filtered by an atmosphere, as on Earth)
- Intense mixed radiation field
- Sputtering created by the presence of a constant solar wind flux.

For sure, when considering the high cost for transporting material from Earth to the Moon, the possibility of using supply of In Situ Re Utilization (ISRU) to build a Lunar outpost is very promising. On the other hand, if lunar soil will be used as building material, many complex technologies will need to be developed and improved, such as robotic excavation or 3D printing in vacuum.

During planetary mission on the Moon surface, the crew and the spacecraft will undergo exposure to different kinds of radiation. The satellite itself is shielding about half of the incoming particle flux met in deep space. On the other hand, being the satellite without an atmosphere nor a magnetic field, no magnetic cut-off attenuation is provided for SPEs and GCRs, allowing even lower energy particles to reach the Moon surface and interact with it. Because of this, if the crew is not sufficiently shielded, for instance during an EVA operation far from the Moon base, a SPE could be lethal.

In addition, both sources interact with the Moon soil, producing a complex and dynamic secondary mixed radiation field through electromagnetic and nuclear processes. This field is made by leptons and hadrons in a widespread energy range, which contributes to the total dose of radiation. Neutrons, in particular, are very difficult to stop, traveling several meters in matter, and they are found around planetary bodies as albedo. However, they decay in a relatively short time, about 11 mins, so they are not found in deep space.

The annual GCRs exposure on the surface is estimated to be around 0.380 Sv in solar minimum and 0.11 Sv in solar maximum periods. On the other hand, a worst case SPE could lead to an exposure of 1 Sv in a very short time [36].

Moreover, the Moon surface itself emits radiation due to the presence of ^{40}K, ^{235}U and the decay chains originating from ^{238}U and ^{232}Th [37].

Exposure doses are going to vary depending on the soil composition of the considered area. Habitats placed inside craters or depressions will be of course more shielded than surface habitats.

In case of worst case SPE, [38] shows the reduction of the effective dose [Sv] due to February 1956 SPE varying the thickness of regolith. Behind 50 cm of regolith, the effective dose was found to be 27 mGy, still alarming being about 25% of the radiation limit for LEO (1 Sv).

In conclusion, missions on the Moon will have to face radiation risks linked to acute and chronic radiation exposure.

Radiation shelters should be designed to protect from SPEs and all the architecture for long term habitation should be optimized to mitigate secondary radiation.

1.7.4 Mars scenario

Human exploration of Mars is considered the main goal of Space Agencies (ISECG, 2013). To allow the feasibility of this kind of missions, knowledge of the energetic particle environment on the planet surface is a key asset.

In future missions to Mars not only the crew could be exposed to large SPEs and background GCRs throughout the long transit to and from Mars, but also during the surface phase.

With respect to the Moon, Mars has an atmosphere, but its density is much lower than Earth's. The degree of shielding provided by the atmosphere to a future crew on the surface will range from about 2.2 $g\ cm^{-2}$ at 25 km of altitude to 30.5 $g\ cm^{-2}$ 7 km below the surface, in basins [21], using the NASA Mars atmosphere model [39], as compared to about 1000 $g\ cm^{-2}$ average for the Earth surface.

The daily radiation exposure on Mars surface will therefore depends on the time-varying space radiation conditions, on the altitude and the different hydrological and soil composition characteristics of the point of exposure. The latter will be responsible for different induced secondary radiation fields.

Three potential mission scenarios for exploration mission to Mars are generally considered: Mars Swing-by, Mars Short Surface Stay and Mars Long Surface Stay, with total duration of 600, 430, 1000 days, respectively (of which 0, 30, 600 days on Mars surface).

The mission itself, will have to be optimized to decrease exposure during the transit phase. Future potential nuclear powered spacecraft, for instance, could guarantee very fast transit, while a mission scheduled in solar maximum conditions will results in less background GCRs exposure.

Monte Carlo simulations show that the total dose received during short surface stays (30 days) during SPEs, as the recent April 2002 and December 2006 SPEs, would have led to annual skin and BFO total doses below the exposure limits [40]. Also, crew exposure simulated for the August 1972, September 1989 and October 1989 event would have not exceeded radiation limits for operations at average altitude on Mars [41].

However, it has been calculated that a very worst-case SPE, such as the Carrington-type event, could result in significant radiation injury for the crew, even if protected

by thick shelters (assumed as 40 $g\ cm^{-2}$ Aluminum shield). In this case, exposure during EVA at very high altitudes (for instance on the Olympus Mons) could be lethal for the crew, while in a thin and thick habitat (5 and 40 $g\ cm^{-2}$ Aluminum shield, respectively) at ground level, 0 km altitude, the total effective dose to the crew would still be very high (0.84 and 0.54 Sv, respectively) [42].

To summarize, many studies have been recently made on the crew exposure to SPEs on Mars, but the results are characterized by a large variability, depending on the initial considered SPE spectrum and exposure condition (altitude/location of exposure, stay duration, shielding conditions).

As regards GCRs, their flux on Mars surface will still be modulated by the solar activity. MSL recorded an average dose rate on the surface of 0.21 mGy/day and a dose-equivalent rate of 0.64 mSv/day [43]. Other studies concluded that GCRs crew exposure on average altitudes on Mars surface were unlikely to exceed space radiation recommended limits [41].

One has however to remember that nowadays radioprotection system is considering endpoints such as cancer, and information on long term effects of GCRs exposure on cardiovascular and central nervous systems are still ambiguous.

1.8 Space radiation shielding strategies

The "traditional" radioprotection system, the one used on Earth typically to protect people from low-LET radiation, relies on 3 main possible protection ways:

- Reduction of exposure time
- Increase of the distance from the radiation source
- Use of radiation shielding.

When dealing with space missions, it is clear that the goal is to be able to stay in space for long time, therefore reducing the mission duration is not an option. Planning a mission in solar minimum could reduce the number of encountered SPEs, while increasing the GCRs exposure, on the other hand during solar maximum GCRs flux, which is more harmful, would be greatly reduced. Nevertheless, the long term objective is to allow human permanence on space to be as long as possible.

Also acting on distance from the source is not going to work: GCRs, which are the main concern for space exploration, are isotropic in space. As regards solar radiation, instead, moving away from the Sun would slightly reduce the intensity of SPEs flux, which however can be shielded with relatively small amount of material.

Therefore, nowadays the use of shielding materials is the only convenient option to mitigate space radiation risk (the so defined "passive shielding approach").

Considering the large variability present in the space radiation environment, the shielding project must necessarily be related to the planned mission scenario. It is fundamental to understand the underlying mechanisms regulating the radiation interaction with matter, to select, when possible, the best combination of shielding materials to mitigate the exposure. Chapter 2 will deal with this topic.

Different shielding strategies can be defined at the moment.

What is generally done in current spacecraft is the creation of a safe area (shelter) in the space habitat, characterized by an increased wall thickness for shielding purposes, where astronauts can spend a great part of their time (e.g. crew quarter, where they usually rest) and take shelter in case of an intense solar event.

A uniform dedicated shielding structure around the entire space habitat can be employed too, reaching at least areal densities of about 25 g/cm^2 of shielding material. Of course this means launching a large amount of material to space, very expansive if launched from Earth. On the other hand, in future, the possibility of using planetary material for shielding could be a realistic option, therefore massive shielding could be produced too and employed for deep space and planetary habitat.

Finally, there is the possibility to use personal radiation shielding equipment, such as the PERSEO radiation shielding suit concept, described in [44].

In the following chapters details on fundamental considerations to make when selecting shielding materials are given.

Chapter 2

Space radiation interaction with matter and effects

2.1 Radiation interaction with matter

When high energy particles such as GCRs pass through matter, they can interact in many ways. In particular, they can release energy to the medium through electromagnetic interactions, for instance interacting with electrons of the medium, or nuclear processes, which originate secondary particles. Part of the incoming energy therefore will not be deposited in the medium as electromagnetic losses, but will be used to produce nuclear break-ups.

While the electromagnetic interaction are theoretically well defined and can be modeled with high confidence, the nucleus-nucleus collisions are very complex and at the moment no fundamental physical theory can be used to describe them and the calculations rely on experimental data. The main reason is due to the fact that these interactions are many-body problems and the particles participating in nuclear interactions are themselves made by other components: nuclei are made by nucleons, which contain quarks and gluons.

The radiation transport can either be treated in a deterministic way, with Boltzmann type transport equations, or by Monte Carlo codes. Boltzmann equation solutions cannot be applied to complex spacecraft geometries and for this reason Monte Carlo codes are used in the framework of this work, allowing a detailed simulation of the reality.

Boltzmann transport equation is based on the conservation principles for a certain particle j with fluence rate $\dot{\Phi}_j(x,\Omega,E)$ as:

$$\Omega\cdot\nabla\dot{\Phi}_j(x,\Omega,E)=\sum_k\int\int\sigma_{j,k}(\Omega,\Omega',E,E')\dot{\Phi}_k(x,\Omega',E')dE'd\Omega'-\sigma_j(E)\Phi_j(x,\Omega,E) \tag{2.1}$$

where $\sigma_j(E)$ and $\sigma_{j,k}(\Omega,\Omega',E,E')$ are the medium macroscopic cross sections and the latter represents all the processes by which a particle k with direction Ω and energy E can produce a particle j with direction Ω' and energy E'. The cross section is inclusive of all reactions and can be divided in collision with atomic electrons, scattering and nuclear reaction cross sections.

Theoretical models and cross sections describing scattering of particles, nuclear models and treatment of different kinds of radiation need to be included in a Monte Carlo code, to enable the interactions reproduction. One can imagine the huge amount of necessary data required, considering all the possible projectile-target combinations, radiation types, etc., when dealing with GCRs transport.

In the following paragraphs, some brief review is given on the main interactions that charged particles of interest undergo when passing through matter.

A complete description of the physics of radiation interactions with matter can be found in [45].

Finally, in the framework of this work, we refer to HZE particles as those having atomic number $Z>2$ and high energy.

2.1.1 Electromagnetic interactions of particles in matter

When charged particles are moving inside matter, they lose energy mainly by electromagnetic interactions, exciting and ionizing atoms with their passage. This process is called primary ionization and, if electrons are created with enough energy (δ-rays), a secondary ionization process can take place. The energy of emitted δ-rays increases with the energy of the primary incoming particle and at high energies they contribute to the energy deposition inside a medium even far away the primary particle's track.

This collision process is the dominant way through which massive charged particles lose their energy and it is a statistical phenomenon, as the collisions can be treated as a series of independent successive events.

The *energy-loss formula* [45] gives a theoretical expression for the energy lost by collision, dE/dx, in the medium by the incoming particle:

$$-\frac{dE}{dx} = \frac{2\pi n z^2 e^4}{mv^2}\left\{ln\left[\frac{2mv^2 W_m}{I^2(1-\beta^2)}\right] - 2\beta^2 - \delta - U\right\} \tag{2.2}$$

where m is the electron mass, n is the number of electrons per cm^3 of traversed medium (equal to $Z\rho N/A$, with ρ the material density in g/cm^3, N the Avogadro number and A and Z the atomic weight and number), z and $v = \beta c$ are the charge and the velocity of the incoming particle, respectively, W_m is the maximum energy which can be transferred to the atomic electrons of the medium, I the mean excitation potential of the medium atoms, δ the density-effect correction factor and U the shell correction term.

When considering heavy charged particles passing through a medium at non-relativistic velocities, the energy lost by collisions can also be referred as stopping power and Equation 2.2 can be simplified in the following way [45]

$$-\frac{dE}{dx} \approx 2\pi e^4 \rho N \frac{Z}{A} z^2 \frac{1}{E_k}\frac{m_p}{m} ln\left(\frac{2mv^2}{I}\right) \tag{2.3}$$

where m_p and $E_k = m_p v^2/2$ are the mass and the kinetic energy of the incoming particle, respectively. It is possible to see the dependence of the energy loss on z^2 and $1/v^2$, meaning that it is increasing with increasing charge and decreasing velocity of the incoming particle. In particular, the created ionization reaches a maximum when the particle has lost almost all of its energy; this maximum is called *Bragg Peak*. Examples of radiation dose deposit curves culminating in Bragg peaks are given in the following chapters.

With the term "heavy ions" atoms beyond helium are meant, with a net positive charge and which can change their charge state when traversing matter. Occasionally, they can interact also with the nuclei of the medium. As they slow down in matter, the probability to capture an electron increases, and at low velocity the electromagnetic interactions with target nuclei cannot be neglected anymore.

For high energy heavy ions, one can apply equation 2.2, also called electronic stopping power, because the dominant process is the interaction with the medium

electrons, but expedients must be applied to consider the fact that the primary charge changes while moving inside the medium.

Furthermore, when the energy is very low, the energy is mostly lost due to collisions with the medium nuclei and this energy lost is referred as nuclear stopping power. The nuclear stopping power increases as $1/\beta^2$.

Scattering processes taking place when the charged particle is moving inside matter are described by cross sections. Most of the electromagnetic cross sections are peaked in the forward directions and they fall off when the energy increases.

Finally, referring to Equation 2.3, it is possible to see how the electronic stopping power is proportional to $Z\rho/A$, where ρ is the medium density.

2.1.2 Nuclear interactions in matter

Hadrons (examples are nucleons and pions) are particles subjected to strong interactions, i.e. nuclear and subnuclear interactions. Understanding how hadrons interact with the nuclei of the medium they are traversing is of fundamental importance when studying shielding means in space applications.

When dealing with high energy hadrons moving into matter, particle creations and nuclear breakups (fragmentation) need to be considered. In particular, for high energies, such as the ones of GCRs, the production of a wide spectrum of secondary particles occurs, and they can in turn give rise to subsequent interactions.

Predicting total and absorption cross sections and secondary particle yields is fundamental when trying to design an effective shielding for space missions. Cross-section data exist on charge changing, elemental, isotopic for total, single and double differential with respect to momentum, energy and angle. A complete review of data interesting for space applications can be found in [31].

The inelastic interactions that characterize hadrons propagation through matter will lead to particle production. Generally, about half of the incoming energy is carried away by primary particles and the remaining part is instead shared between the produced secondaries, which can be relativistic hadrons, nucleons and spallation nucleons, break-up and recoiling fragments. Typically we use the term "projectile" or "target" fragments to describe particles emerging from a heavy-ion fragmentation

reaction. The former are generally maintaining the incident particle direction and velocity, while the latter are instead emitted isotropically and with low energies.

Nuclear absorption by fragmentation is the dominant nuclear process for heavy ions with energies greater than 100 MeV/nuc.

As already said, no fundamental theory exists to describe nucleus-nucleus collisions, and this is why many semi-empirical models exist to describe these interactions. For instance, different models exist to describe nuclear fragmentation after a hadron-nucleus collision, i.e. to describe the heavy ion fragmentation cross section. All of them are based on a two-step process, called cascade and evaporation, or abrasion and ablation: a fireball is formed after the incoming particle hits the nucleus and the resulting secondaries depend on the kind of collision. Peripheral collisions generally lead to small mass removal from the target, while central collisions result also into the destruction of the involved nuclei.

When nucleons are knocked-out the nucleus, a nuclear interaction called spallation process occurs. Internuclear cascade models can describe the physical processes inside nuclei, after the incoming particle is "temporarily absorbed" inside the nucleus, forming an intermediate state and interacting with other nucleons, leading to the production of highly excited nuclei with different decays modes, such as multifragmentation, vaporization, fission or evaporation. After that, the nucleus de-excitates. In this process nucleons can be ejected or light nucleons can aggregate to form deuterons, tritiums, alpha particles, etc. Also fission can occur if the nucleus is heavy enough.

The knocked-out products produced by protons and neutrons reactions and the projectile fragments of GCRs still present a moderate LET, and in addition have a usually high range, enabling them to create radiation built-up far away from the incoming particle track.

The momentum distribution of the fragments is forward peaked and can be described with a Gaussian distribution.

Evaporation processes can take place when the remaining nucleons in the excited nucleus stay trapped inside the nucleus after the emissions of some of them with energies higher than the binding one. During evaporation, the remaining nucleons aggregate to form different kinds of states (d, t, ^{3}He, ^{4}He, etc) and the nucleus "evaporates".

The evaporation low-energy products constitute a high-LET component of the produced secondary particles, important for the radiobiological damage.

In the GCRs case, all these interactions lead to a light particles build-up which characterizes the secondary environment inside a space habitat. In particular, generally the most penetrating among the produced fragments have a lower LET than the one of the incident ion, as dE/dx goes with Z/v^2, and v is almost the same. On the other hand, the high LET fragments have very short ranges.

Quantitative approaches to describe in details the hadronic interactions with matter use Monte Carlo codes. For these codes, it is fundamental to quantify the total and absorption cross section, to determine in a first instance whether an interaction has taken place or not.

In particular, the cross section for nucleus-nucleus interactions can be described by the energy-dependent versions of the Bradt-Peters equation [46], Equation 2.4:

$$\sigma_{abs} = \pi r_0^2 c_1(E)[A_p^{1/3} + A_T^{1/3} - c_2(E)]^2 \tag{2.4}$$

with r_0 is the nucleus radius, $c_1(E)$ and $c_2(E)$ are energy dependent parameters and A_p and A_T are the projectile and target atomic mass numbers, respectively.

Many versions exist of this formula. For instance, NASA uses for its codes the Wilson and Townsend formula to describe the nucleus-nucleus interactions giving rise to charge chance (cc) in the primary particle, which is a modified version of Equation 2.4 ([47]):

$$\sigma_{cc} = \pi r_0^2 [A_p^{1/3} + A_T^{1/3} - 0.2 - 1/A_p - 1/A_T]^2 \tag{2.5}$$

To a first approximation, considering that the nuclear radius is proportional to $A^{1/3}$, it is possible to assume that the probability of a nuclear interaction is proportional to the cross sectional surface area for nuclear collisions (from 2.4 it goes as $A^{2/3}$) normalized by the number of nucleons encountered (A), hence proportional to $A^{-1/3}$. It follows that the lower the atomic mass number A, the higher is the probability of a nuclear interaction to take place.

2.2 Quantities of interest

Some paragraphs follow where a description is given of the quantity of interest that will be calculated through our simulations and tests as described in the following chapters.

2.2.1 Absorbed dose, Equivalent Dose, Dose Equivalent and particle fluence

The absorbed dose D, expressed in Gray (Gy = J/kg):

$$D = \frac{d\varepsilon}{dm} \tag{2.6}$$

is calculated in the volume of interest, where $d\varepsilon$ is the mean energy imparted in a volume of mass dm by ionizing radiation. This quantity takes into consideration only the energy deposition in matter, but nothing is said on the effects this energy deposition has on biological tissues.

Therefore another quantity, the equivalent dose measured in Sv (again J/kg), is introduced because the absorbed dose is not considering that different types of radiation have different effects on human tissues and organs, with some of them producing greater biological damages than others for the same amount of imparted energy.

According to the International Committee of Radiation Protection (ICRP) [48] equivalent dose is a dose quantity representing the stochastic health effects (probability of cancer induction and genetic damage) of low levels of ionizing radiation on the human body, obtained from absorbed dose in tissue multiplied by a radiation weight factor, w_r, dependent on the type and energy of the considered radiation.

The radiation weight factors for different radiation types can be found in Table 2.1.

Radiation type	Radiation weighting factor, w_r
Photons	1
Electrons and Muons	1
Protons and charged pions	2
Alpha particles, heavy ions	20
Neutrons	refer to Eq. 2.7

Table 2.1 Radiation weighting factor, w_r

As concerns neutrons, the following function is considered in ICRP Publication 103 [49] for the calculation of neutron radiation weighting factors:

$$w_r = \begin{cases} 2.5 + 18.2e^{-[ln(E_n)]^2/6}, & E_n < 1MeV \\ 5.0 + 17.0e^{-[ln(2E_n)]^2/6}, & 1MeV \leq E_n \leq 50MeV \\ 2.5 + 3.25e^{-[ln(0.04E_n)]^2/6}, & E_n > 50MeV \end{cases} \tag{2.7}$$

This approach is the one usually applied in case of typical "ground exposures", where low-LET radiation is generally involved, in particular photons and neutrons. Examples of ground exposures are nuclear plants accidents or exposures following explosions of nuclear bombs.

Obviously, a $w_r = 20$ for alphas and heavy ions, as defined in the ICRP publication 60 [50], does not reflect the variation of Relative Biological Effectiveness (RBE)[1], indication of the biological impact, with the type and energy of heavy ions: Figure 2.1 [4] shows different ionization density tracks of protons, alpha particles and heavy ions up to iron and compare them with a mammal cell dimension. The ionization density increases as the ion charge increases; it is proportional to the deposited energy and therefore to the potential of creating biological damage to the cell.

Furthermore, in [5], Sato et al. showed how the heavy ions body-mean quality factors vary with energy (see Figure 2.2). For this reason another approach, using quality factors, Q, instead of the w_r, is employed under the assumption of a general dependence of RBE on either LET or on a factor dependent on the effective charge number of a particle (including a velocity dependent screening correction) and the speed of the particle scaled to the speed of light, $Z*^2/\beta^2$ [51] [52]. In particular,

[1]RBE is calculated as the ratio of the absorbed doses of two types of radiation producing the same specified biological effect under identical irradiation conditions and considers therefore the differences in biological effects. It depends on exposure scenarios, considered tissue or organ, dose rate, etc

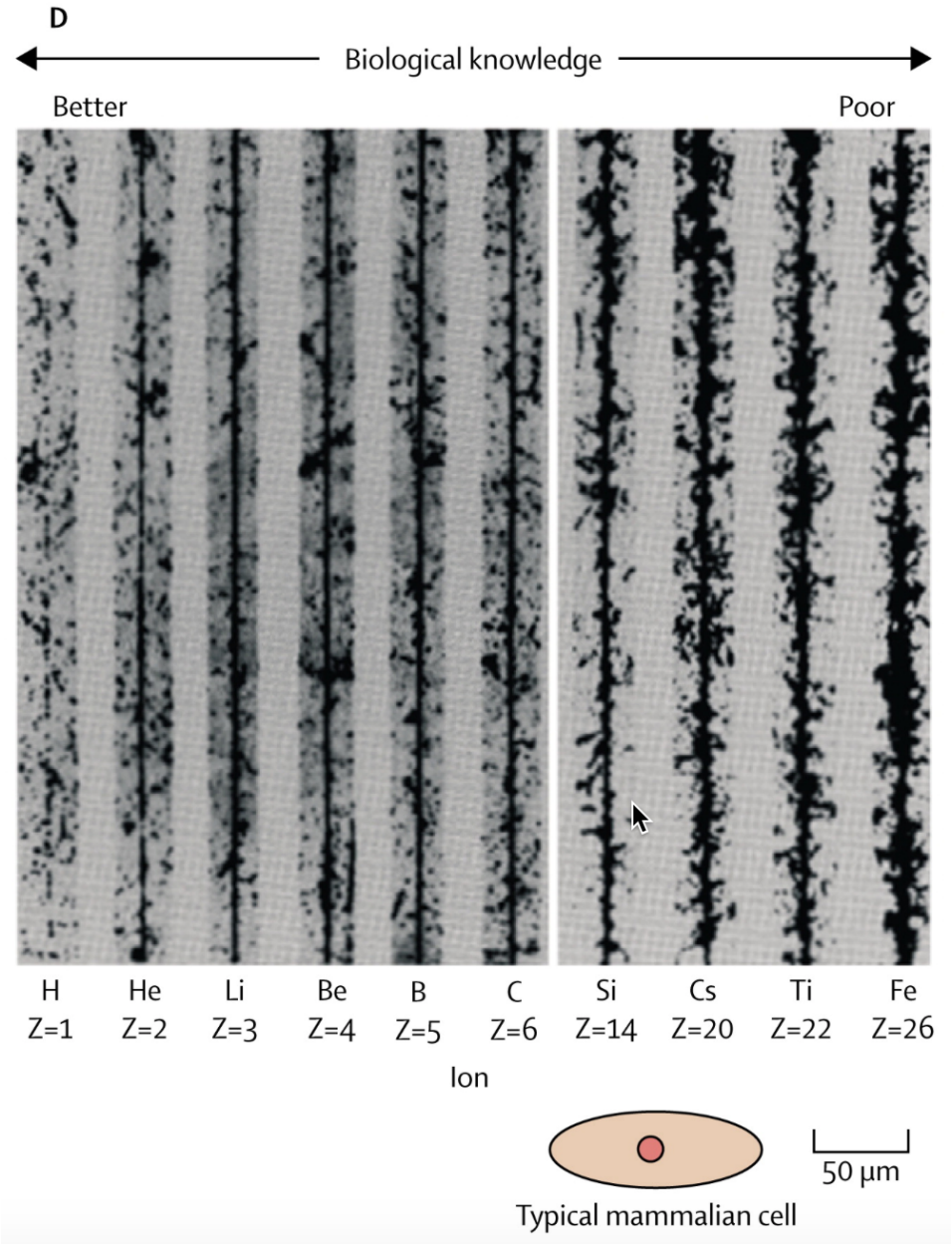

Fig. 2.1 Tracks of different ions, from H to Fe, in nuclear emulsions, showing increasing ionisation density (LET=dE/dx) as the electric charge, Z, increases. Pictures copied from [4].

this parameter describes the track density of ionization caused by a particle, due to $\delta-$rays production, considering therefore the difference between the track structures arising from differently charged particles.

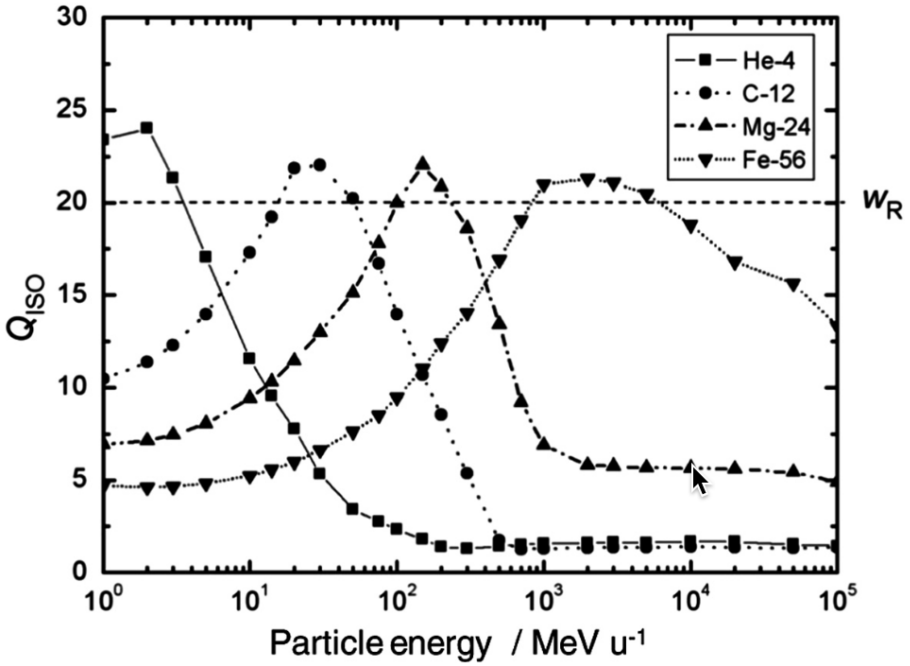

Fig. 2.2 Radiation weighting factor (w_r) and energy dependent body-averaged quality factors ($Q(E)_{ISO}$) for ^{4}He, ^{12}C, ^{24}Mg, and ^{56}Fe (under the assumption of an isotropic incidence) versus the ion energy, from [5].

In conclusion, long cosmic ray exposures, where doses coming from heavy ions may be significant, should be handled in a different way than the typical "ground exposure" [49] and, for estimation of the radiation risk for astronauts, another approach is generally used, applied by space agencies, where the organ dose equivalent, $H_{T,Q}$, is defined (in Sv too):

$$H_{T,Q} = Q_T D_T \tag{2.8}$$

where D_T is the absorbed dose, previously defined in Eq. 2.6, into a certain organ or tissue T. This organ dose equivalent is generally used as a surrogate for the equivalent dose (meant as $D * w_r$) in space dosimetry [26] and is defined as the product of the absorbed dose with a quality factor Q at that point, where the quality

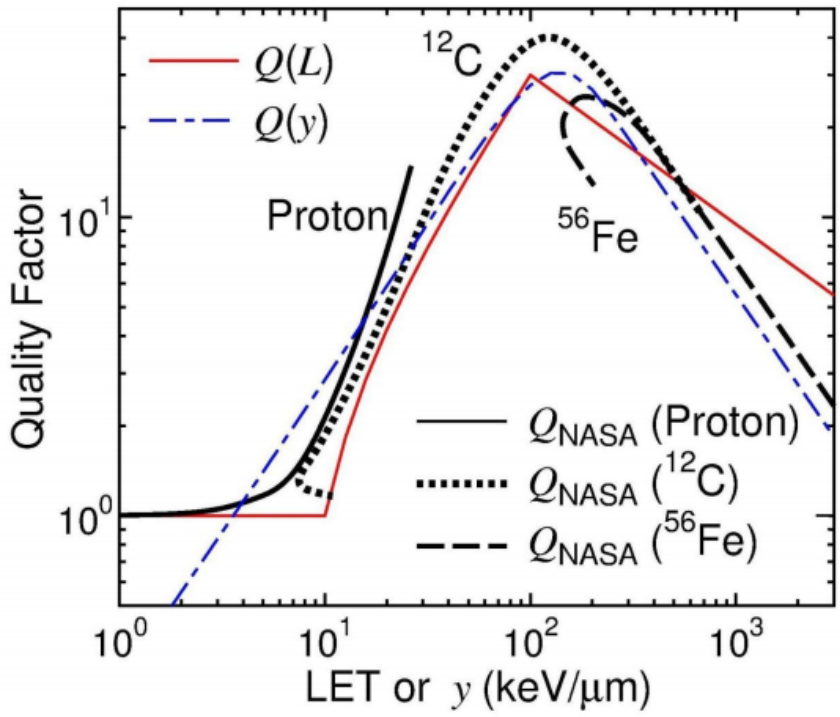

Fig. 2.3 Comparison between different values obtained for quality factors for solid cancer: NASA values for protons, carbon and iron ions - Q(L,E) , ICRU Report 40 microdosimetric approach Q(y) and the traditional one, based on the LET, Q(L), for different ions. [6].

factor is traditionally a function of the unrestricted LET [2] in water, as defined in ICRP Publication 60 [50].

When using the Q(L) function, Q_T is calculated as:

$$Q_T = \frac{1}{m_T D_T} \int_{m_T} \int_{L=0}^{L=\infty} Q(L) D_L dL dm_T \tag{2.9}$$

where m_T is the mass of the considered organ or tissue and D_L the dose released with a certain LET, L. When instead Q(Z,E) is used (dependent on the $Z*^2/\beta^2$ factor), integration over energy instead on LET is performed.

Finally, the *effective dose equivalent* is calculated as per ICRP Publication 103 [49]:

$$H_E = \sum_T w_T H_{T,Q} \tag{2.10}$$

where w_T are the tissue weighting factors, for males or females. Risk estimations, however, should be based on absorbed dose or dose equivalent in a certain tissue or organ, and not on the effective dose equivalent.

All the above mentioned concepts apply for the case of exposure to low doses, such as a GCRs exposure. When, on the other hand, high doses are involved, for instance in case of exposure to a SPE, another approach should be followed, using the RBE relative of a specific effect in a specific tissue/organ and multiplying it by the absorbed dose in the tissue/organ (in Gy). This resulting dose is expressed in Gy-equivalent and it is not used in this work.

Fluence (Φ) over volumes inside habitat is often calculated for 3D simulations and is defined as the number dN of particles incident on a sphere of cross-sectional area da. Using a sphere, the area perpendicular to the direction of each particle is accounted in a way that all particles passing through this volume of space are included.

$$\Phi = \frac{dN}{da} \tag{2.11}$$

In this work's Monte Carlo simulations, information about the deposited energy is registered through each step along the particles trajectory inside the target. Therefore, to calculate the absorbed dose D in a certain region the energy deposited for each step in the volume is summed up and divided by the mass of the region. To compute the

[2] the transfer energy including the energies of all emitted $\delta-$rays independent of their range

dose equivalent ($H_{T,Q}$) in the region, the deposited energy in each step is multiplied by the corresponding quality factor, which is calculated by applying the selected Q(LET) relationship.

2.3 Radiation biological effects

As mentioned above, one of the most serious challenges for space exploration missions in deep space concerns the radiobiological effects on astronauts' health. While the physiology of microgravity effects has been widely studied during long-term missions to space stations, acute and late risks caused by space radiation exposure during and after exploration missions are not conclusively known.

In this section a brief summary of the main biological information available in literature on radiation effects on biological tissues is given.

In principle, it is necessary to report that further studies are needed to better understand the effects on biological systems of the wide assortment of atomic numbers, LET, energies and fluencies of the particles encountered in space. The majority of information on radiation damage comes in fact from follow-up studies of the Japanese population irradiated as a consequence of the atomic bomb explosions of Hiroshima and Nagasaki. These people were subjected to low-LET radiation and the radiation protection models built on these data are not always applicable to space exposures. As a consequence, risk assessment needs often to rely on simplified experimental models and biophysical calculations.

The effect of major concern when biological systems are exposed to radiation is DNA damage. This can happen as a consequence of the direct interaction of radiation with DNA strands or indirectly, for instance when the DNA chain is damaged by radiation-produced radicals formed from water molecules found in the cell.

Low-LET radiation is mainly giving rise to the so called "indirect damage", i.e. radiation is not directly damaging the DNA interacting with its molecules, but initially interacts with the water present into the cell. As a consequence of this initial interaction, free radicals are produced and they are attacking and damaging the DNA. When cells are irradiated with low doses of low-LET radiation, several breaks of a single strand of DNA can take place and they are usually immediately repaired using

the opposite strand as a template. A mutation can occur when the repair process is incorrect, potentially giving rise to stochastic effects as solid cancer or leukemia.

High-LET radiation (e.g. GCR ions found in space) on the other hand is able to produce a larger amount of damage to the DNA molecules. When high-LET radiation passes through biological tissues, a densely ionizing track of damage is produced and this can cause complex damages in the DNA strands, including double strand breaks[3], believed to be the most important lesions produced in chromosomes by radiation, potentially leading to chromatin snapping into two sections. The double strand breaks are very difficult to repair and their interactions can cause a series of negative biological effects, such as cell killing, carcinogenesis and mutation. Misrejoining of separated sections generally leads to large DNA deletions and chromosome aberrations, thus often the cell cannot survive or reproduce. Cell death is in particular very alarming: in fact, exposure to HZE radiation seems to lead more frequently to cell death. One reason of this can be found on the poor capability of the cell to repair the HZE damage, generally much more intense than for low-LET radiation [4].

Space radiation effects are usually classified into two main categories, stochastic effects and deterministic effects. Also, in recent time, another classification can be found in literature, categorizing them in late effects or early effects, based on the time of appearance of the effect. Early effects refer to the DNA damage itself.

A recent and complete review of the space radiation biological effects and on the development of effective countermeasures is found in [53].

2.3.1 Stochastic and deterministic space radiation effects

The stochastic effects (including the majority of late effects) are identified as the effects for which the probability and not the severity of the effect increases with increasing radiation exposure (e.g. cancer and leukemia).

[3] In a double strand break the DNA chain is cut in two and it is not possible to use the opposite strand as template to repair the DNA chain. In this case some bases can be lost and the DNA chain, if repaired, can be sewed up with some of the bases missing leading to complicated erroneous chromosome rearrangements

On the contrary, deterministic effects are effects for which a threshold radiation dose exists for them to happen and their effects usually worsen with the dose (e.g. skin erythema gets worse with the amount of radiation dose absorbed by the skin).

The main biological effects which can rise following space radiation exposure are chronic consequences such as cancer, leukemia, degenerative tissue effects. Acute effects could happen only in case of crew exposure to a very intense SPE, without adequate protection (i.e. shielding). Such scenario has the capability to cause massive damages to the crew and potentially lead to acute radiation syndrome (for details, refer to paragraph 2.3.2).

Even if cancer is considered at the moment the dominating stochastic effect and cancer mortality risk estimates are the base of the actual radioprotection system, also other non-cancer effects could become important, in particular when interplanetary long duration missions are considered. The non-cancer effects of interest in these cases are acute and late damage to the Central Nervous System (CNS), cardiovascular and respiratory system diseases, cataract formation [51].

More information are needed to be able to calculate risk of these kinds of effects, and recent works include [54] and [7]. In particular, heavy ions effects to the CNS have been observed in mice irradiated with iron beams and include behavioral deficits, possibly the induction of Alzheimer's disease, deficits in memory and spatial learning, cell loss. Of course, these effects are of great concern, having the ability to impact mission success.

Exposure to space environment is also able to alter the immune system response [55], but also in this case, data on exposure to HZE radiation are very scarce.

Finally, there are several studies suggesting that HZE-induced cancers are more lethal to the ones caused by low-LET particles. This is still not accounted in current risk models, which treat all radiation induced cancers as similar to background cancers in the population.

2.3.2 Acute Radiation Syndrome

Acute Radiation Syndrome (ARS) is a condition originating after a whole body exposure to a high dose of radiation. In space it could happen in case of SPE

exposure behind tiny shields or during EVA operations. It consists of several effects, which could last up to several months and may lead to the death of the individual.

The onset and the type of the symptoms depend on the exposure dose and ARS can be subdivided in three categories (whose onset depends on the dose): the hematopoietic syndrome, the gastrointestinal syndrome and the CNS syndrome, with only the first two as a realistic consequence in space.

The hematopoietic syndrome is characterized by a drop in the number of blood cells, caused by damages to the progenitor cells of the red marrow. Changes in the blood can be detected after whole-body exposure of just 0.25 Gy, while the syndrome, with the illness that may lead to fatal consequences, occurs at around 2 Gy of received dose. In space, for very high exposures, the effects could include also nausea, vomiting and diarrhea (gastrointestinal syndrome).

Protecting the BFO also using personal selective shielding, such as radiation suits with thicker protection in the BFO areas, can prevent ARS. A recent work on this subject can be found in [44], where the authors propose different suit designs and calculate the increase in protection given to the astronaut wearing them.

2.3.3 Space radiation limits

In space two kinds of radiation limits are defined: short term limits to prevent clinically significant non-cancer effects and career limits to prevent the incidence of late effects.

In the first group performance degradation, in-flight illness, skin damage, cataracts and death are included and limit doses are expressed in Gray equivalent [Gy-eq] (dose in Gy multiplied by the RBE), while the second group regroup all the stochastic effects (such as cancer, leukemia), and the limit doses are expressed in Sv.

At the moment only limits applicable in LEO missions exist, due to the still high uncertainties characterizing the knowledge on non-cancer risks and high-LET radiation cancer induction. Moreover, different limits exist among the different space agencies. Some of the agencies (e.g. NASA) have gender and age dependent limits, while others use single values of allowed dose.

NASA career limits are calculated to consider a 3% Risk of Exposure Induced Death (REID) from cancer, and they include new limits for central nervous system

and heart disease risks. There is an additional requirement for which the risk limit must be calculated with a 95% confidence level.

Career effective dose limits (in Sv) as recommended by different space agencies are reported in [51].

As regards deep space, through their risk models NASA is producing an estimation of "safe days in deep space", defined as the maximum number of days with 95% Confidence Level (CL) to be below the NASA 3%REID limit. Calculations are usually made for both solar minimum and maximum conditions, with 20 g/cm^2 aluminum shielding, differentiating between astronauts' age and gender. Estimations for a never-smoker population are also available, considering that astronauts are conducting a healthier life than the average US population. Two of the most recent works on the subject are found in [7] and [54]. For instance, a 45 year old woman, never smoker, can reach about 300 "safe days" in space to be below career exposure limits for REID. Some of the results reported in [7] are shown in Figure 2.4.

Finally, as in traditional radiation protection, the As Low as Reasonably Achievable (ALARA) principle is generally observed when trying to ensure the astronauts crew safety.

This thesis work is focused on the attenuation of GCRs detrimental effects, and therefore neither ARS nor other acute effects are further considered. Calculations will be made for chronic exposures and results will be produced in Sv/year, to consider the late effects.

2.4 General references for this Chapter

When trying to summarize the principles of particle physics guiding this work, the following book has been taken as reference: Leroy, C. and Rancoita, P.G., "PRINCIPLES OF RADIATION INTERACTION IN MATTER AND DETECTION", 2004 by World Scientific Publishing Co. Pte. Ltd., ISBN 981-238-909-1

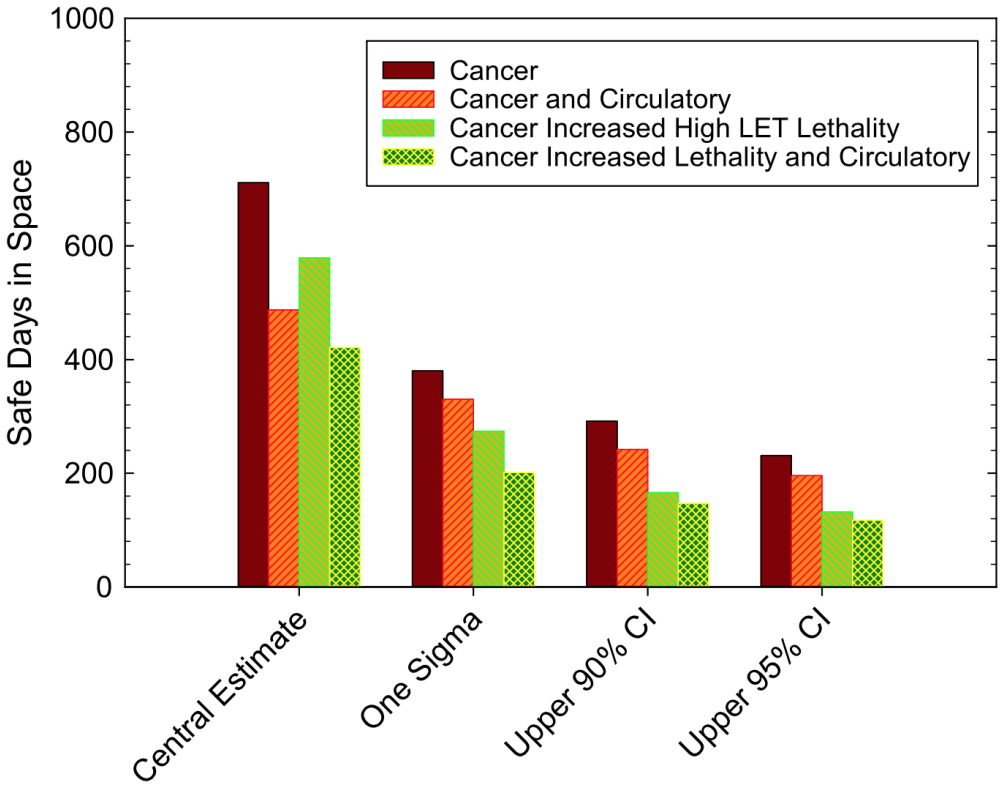

Fig. 2.4 Predictions of the number of "safe days" in space to be below career exposure limits for REID using different assumptions on allowable uncertainties in the NSCR-2014 model without or with additional fatal risk contributors. Prediction are for a 45 year old female never smokers in the NSCR-2012 and NSCR-2014 models. Picture taken from [7].

Chapter 3

Space radiation shielding materials selection

One of this work's objectives is to select and test, under radiation beams, materials which could be used as shielding on board of a spacecraft or in a planetary habitat. In addition, considering that everything on board is contributing to the final radiation field inside the spacecraft itself, also materials present in large quantities are considered in this selection (such as aluminum alloys).

The idea behind this work is also to compare radiation test results with Monte Carlo simulations (Chapter 5), to verify the ability of the codes to reproduce radiation interactions with space materials and, therefore, to increase our confidence in the results of 3D realistic simulations of space exposures (Chapter 6).

This chapter summarizes the work done at the beginning of the ESA funded ROSSINI2 project to select and procure materials for future radiation tests. In particular, a trade-off was carried out considering different selection criteria and also taking into account their ability to attenuate space radiation, using the results of 1D Monte Carlo space radiation simulations, described in a dedicated chapter (Chapter 4).

From a large number of materials initially considered, a list was produced from the trade-off, with a ranking of suggested materials to be tested. Of course, considering procurement time and costs constraints, it was not always possible to acquire the desired material. For this reason during the project additional materials,

not initially considered in the trade-off, were added as replacement of the ones which could not be procured.

In the following paragraphs a description is initially given of the rationale behind materials selection, including information on the trade-off method and trade-off criteria, and the materials selected to undergo testing are described.

3.1 Material selection for space radiation shielding

The selection of candidate materials was mainly guided by basic principles of nuclear physics discussed in the previous chapter. From Equation 2.3 it is possible to see that the incoming ion mass stopping power is proportional to Z/A and therefore materials characterized by a high Z/A ratio are better into stopping charge particles than others.

In addition, the number of nuclear interactions is proportional to σ/A, with σ being the total nuclear reaction cross section of the material, proportional as a first approximation to $A^{2/3}$ (refer to Equation 2.4). This means that the rate of nuclear interaction into matter is proportional to $A^{-1/3}$. As a consequence, when selecting materials for radiation shielding in deep space exploration missions, low A number materials with sufficient density should be preferred to heavier ones with similar properties.

Atom	Z	A	Z/A
H	1	1	1,000
He	2	4	0,500
Li	3	7	0,429
Be	4	9	0,444
Be	5	11	0,455
C	6	12	0,500
N	7	14	0,500
O	8	16	0,500
Al	13	27	0,481
Ti	22	48	0,458
Fe	26	56	0,464

Table 3.1 Z/A ratio for a subset of atoms

Table 3.1 reports the Z/A ratio for some atoms and can be used as a primary guideline for this selection. However, considering only radiation protection properties

is not enough and a well-considered selection needs to be carried out among the several candidate materials to understand which ones are the best choice evaluating many aspects. For instance, materials need to be safely usable in space: the use of a potentially explosive material, even if very performing for radiation protection, would constitute a hazard and would not be acceptable in space.

Due to the large number of criteria and materials which need to be considered, the Analytic Hierarchy Process (AHP) [56] was selected as trade-off method. AHP is characterized by a series of pairwise comparisons, relying on the judgments of selected experts to derive priority scales. With this method, decisions are made in an organized and possibly objective way, under quantifiable conditions, which marks a choice or another as better or worse. Every alternative is indeed judged in relation to all the others, and at the end of the process a ranking of all the possible choices is provided.

The main steps of the procedure are:

1. Problem definition, together with criteria identification
2. Criteria ranking, comparing them to each other
3. Trade-off alternative definition (in this case, the possible shielding materials)
4. For each previously defined criterion a trade-off of the alternatives is done
5. For all the alternatives, at the end of the previous step, a score is provided from the point of view of each criterion and then, considering the criteria relative weights, a global ranking is obtained.

A detailed description of the method can be found in [56].

3.1.1 Trade-off criteria

The criteria evaluation has been carried on with the support of a team of experts from Thales Alenia Space, finally leading to the choice of the following ones:

Reliability of the simulations taking into account the capability to reliably simulate the material with Monte Carlo tools. The quality of nuclear cross-section is

evaluated inside this criterion, together with the ability to implement the physical structure. For instance, dusts and porous materials are more complicate to simulate than homogeneous structures.

Simulation results a global score is assigned to each material to take into account dose-reduction for thicknesses compatible with their use in space. Simulations results of dose attenuation have been considered as trade-off criteria. Details and results of the simulations of the interaction of the space radiation environment with the materials are found in Chapter 4.

Multifuctionality meant as the capability of a material to perform other functions in addition to radiation shielding. For instance, carbon fibers could be used as structural materials while providing some degree of radiation shielding at the same time, water could be used as radiation shielding and as life support fluid.

Environment compatibility including the external, the internal and the launch environment compatibility. External compatibility is mainly intended as the compatibility with the vacuum and thermal excursion environment, while the internal one is the compatibility with the cabin air composition, pressure, temperature and humidity. Finally, launch environment compatibility is meant as the compatibility with the mechanical environment of a launcher including static loads, shocks, vibrations and possible fairing depressurization.

Availability considers the availability (in a short time) of the material on the European market. Cost is included in this voice: if the material cost is highly prohibitive the availability will be low. The fabrication time of the test samples is also included in this criterion.

Processability meant as the ability of a material to be processed without particular difficulties, including also the material compatibility with basic requirements, such as safety (not toxic or flammable materials), the possibility to be used without complicate means of cooling or containment, and so on.

TRL – Technology Readiness Level defined by an absolute number (from 1 to 9) instead of being defined through a pairwise comparison matrix. The ESA definition of TRL is taken from [57].

3.1.2 Trade-off materials

Several different categories of materials have been considered in the trade-off, starting with materials already used in space and innovative ones, in particular hydrides, polymers and structural materials.

Structural materials are the ones which can be used when building the primary and the secondary structure of a space vehicle.

Some of the evaluated materials can be considered as multifunctional, for instance water can be used as radiation shielding and as life support system reserve.

Polymers are very interesting from a radiation protection point of view, being characterized by low atomic numbers. They are widely used for space applications and they can be employed to form composite structures. To be used in space, they must respect very stringent requirements, due to the hostility of the space environment.

The hydrogen containing materials are known to better perform in a high energy ionizing radiation environment. This is due to the high electric stopping power of hydrogen, which unfortunately cannot be effectively used pure, neither in the liquid nor in gaseous state. A way to deal with this problem is to produce high hydrogen content materials, where hydrogen is for instance embedded in polymeric lattices, the latter conferring structural strength and rigidity, or forming hydrides with other light elements (Lithium, Magnesium, etc..). These compounds can involve either thermoplastic or thermosetting polymers, leading to different configurations of the final product, that could be bulk solids, layers, films or fibers.

Lead and iron have also been considered as control materials to have an immediate validation of the process. Their final ranking is supposed to be low if the trade-off has been carried out in a correct way.

3.1.3 Trade-off results

The previously described criteria have been compared to each other and a weight has been assigned to each one of them. In our case, the effectiveness of shielding radiation (simulation results), the environmental compatibility and the processability of a material were considered the most important criteria.

Under these assumptions, the ranking reported in Figure 3.2 shows the trade-off results.

The trade-off activities are not further described in this work, being outside the scope of this Thesis.

It is possible to notice that some materials are already used in space missions, such as Aluminum, Kevlar, High Density PolyethylenE (HDPE). Others are potentially good materials but considered not interesting to be tested in the framework of this study; examples are: water, liquid hydrogen (H_2-liq), and $LiBH_4$. Finally some materials not yet used in space mission applications were considered for further investigations in accelerators, such as Lithium Hydride, LiH, and combinations of epoxies and polymers.

After the trade-off was over, a procurement phase started in which in Thales Alenia Space we selected materials to be tested in particles accelerators, using the trade-off results as reference. We were not able to procure all the materials considered in the trade-off and for this reasons additional ones were selected halfway this thesis' work. Furthermore, some space materials and multi-layers configurations were also considered, to study the radiation attenuation properties of existing and future space structures, with or without additional shielding.

Simulations, described in the following Chapter, were however made for each material considered in the trade-off.

3.1.4 Selected materials for radiation test

The following section reports a brief summary of the properties of the principal materials selected for radiation testing.

Hydrides selection

In the framework of ROSSINI2 study a collaboration started between Thales Alenia Space and University of Turin (UNITO): lightweight hydrides for radiation shielding applications have been reviewed and selected. Several chemical elements can form hydrides, whose stability depends on the pressure and temperature conditions. Among those, despite still sensitive to moisture in different measures, LiH, NaH, MgH_2 and CaH_2 show high hydrogen content, coupled with a reasonable chemical

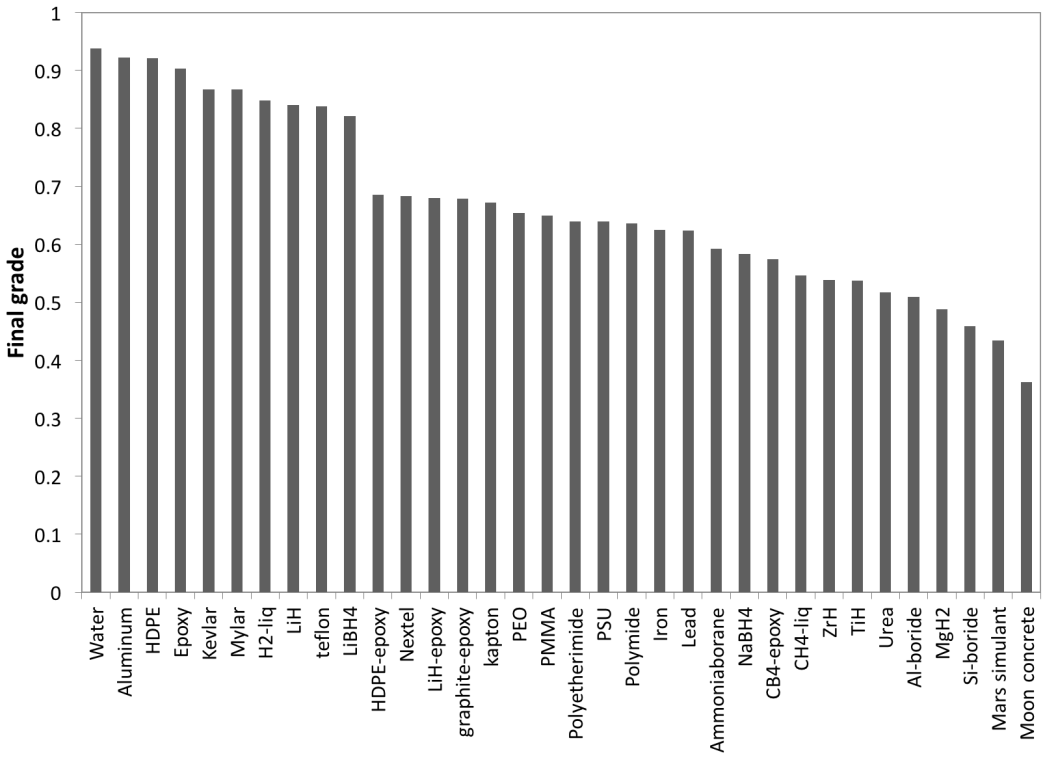

Fig. 3.1 Trade-off results between the considered materials

stability and with limited toxicity issues. Considering the analysis made by UNITO and the results of the 1D radiation shielding Monte Carlo simulations (the reader can refer to Chapter 4), only compounds containing Lithium were selected for the preparation of the radiation test samples. Moreover, a result of the simulation work (Chapter 4) was that mixing hydrides containing elements lighter than Carbon with HDPE should lead to enhanced shielding performances with respect to plain HDPE, which is the major competitor of hydrides in this field. Some early works on this subject can be found in the United States Patent Application No. 20140178291 [58]. Preparation of ten pellets containing compressed powder of LiH to provide samples to be tested as radiation shielding materials has been made, while the original idea of preparing also some samples of $LiBH_4$ has been then discharged for safety reasons. Pellets were packaged in a sealed Polyethylene (PE) bags to prevent contact with moisture.

In the Tables 3.2 and 3.3, the pellet properties, also used as reference to reproduce the material in Monte Carlo simulations against experimental data, are reported.

Fig. 3.2 Final packaging of the LiH pellets, made by UNITO. PE is surrounding the LiH to prevent contact with moisture present in water

Materials for spacecraft structures

Different kinds of materials were provided and/or manufactured to reproduce typical space habitats configurations and to test them under different kinds of radiation. Being one of the ROSSINI2 project goal to study the effects of layering on the radiation field found inside a typical deep space or planetary habitat, each material has been kept separated from the others, to allow the mounting and consequent testing of different arrangements.

Table 3.4 reports the space materials which have been selected for the irradiation test campaigns.

Materials number 1 and 2 are aluminum honeycomb structures, used in space to allow the minimization of the amount of material to reach minimal weight and minimal material cost while keeping relative high out-of-plane compression properties and out-of-plane shear properties. There are many shapes and features possible for honeycombs and in the framework of this study two different samples are provided, of the same Aluminum alloy, Al5056, and with different hexagonal cells densities.

Test sample number 3 is a piece of foam Zotek F30 of 200x200x25.4 mm, with an aeral density of 0.03 g/cm^2. It is used in the spacecraft internals, both in inflatable and in rigid module configurations.

Sample	Weight (g)	Diameter (cm)	Height (cm)	Vol (cm^3)	Dens (g/cm^3)
1	19,9	6,5	1,1325	37,5798	0,5295
2	19,7	6,5	1,1350	37,6628	0,5231
3	19,3	6,5	1,1125	36,9162	0,5228
4	20,0	6,5	1,1325	37,5798	0,5322
5	20,0	6,5	1,1350	37,6628	0,5310
6	19,4	6,5	1,1000	36,5014	0,5315
7	20,0	6,5	1,1250	37,3310	0,5357
8	19,8	6,5	1,1150	36,9991	0,5351
9	20,0	6,5	1,1200	37,1650	0,5381
10	19,6	6,5	1,1075	36,7503	0,5333

Table 3.2 LiH pellets properties, made by UNITO

Sample Height (cm)	Sample Density (g/cm^3)	Total Aeric Density (g/cm^2)
1,1215	0,5312	5,9579

Table 3.3 LiH pellets average properties, used in Monte Carlo simulations

Aluminium 2024 (Al2024) (test samples number 4 and 6) has been chosen because it is one of the most used materials in space. Pure Aluminum is widely characterized from a radiation point of view, however Al2024 contains only about 92%wt of it (Table 3.5). Al2024 is used both to guarantee structural resistance and to protect the spacecraft from debris and micrometeoroids. 3 pieces of 0.508 mm of thickness and 5 of 1 mm each are provided, to test multilayered configurations where this materials is employed in different ways. Furthermore 10 additional samples (with a 2 mm thickness) have been procured to allow the material characterization in terms of dose reduction.

Samples 5 and 7 are Carbon fiber–reinforced plastic (CFRP), or often simply carbon fiber, an extremely strong and light fiber-reinforced plastic which contains carbon fibers. CFRP can be expensive to produce but it is used whenever high strength-to-weight ratio and rigidity are required. It could be used instead of Aluminum as primary structure in a spacecraft, and in the framework of this project it is interesting to study the differences in radiation shielding capability of these two options. The CFRP panels were made in the production department of Thales Alenia Space Italia, Torino, using carbon fibers and impregnating them in Hexcel resins.

N	Name	x [mm]	y [mm]	z [mm]	Dens [g/cm^3]	Thick [g/cm^2]
1	Al 5056	200	200	57	2.64	-
2	Al 5056	200	200	60	2.64	-
3	Zotek F30	200	200	25.4	0.03	0.076
4	Al 2024	200	200	0.508	2.78	0.141
5	T3001k	200	200	0.6	1.5	0.09
6	Al 2024-T8	200	200	1	2.78	0.278
7	T3001k	200	200	1	1.5	0.15
8	Kevlar Resins	300	300	6	1.1667	0.7
9	PPSU	192	192	31	1.290	3.99
10	Nextel 8	100	100	7	1.1429	0.8
11	Kevlar layer	300	300	-	-	0.028
-	Bladder	300	300	-	-	-
12	Nextel 4	100	100	3.5	1.1429	0.4
13	VECTRAN	100	100	-	1.4	-
14	Moon Simulant	-	-	-	1.7	-
15	Moon Concrete	100	100	10	1.64	1.64
16	PBI	100	100	30	1.30	3.90

Table 3.4 Space materials selected for the irradiation test campaign

Al2024 %wt				
Al	Si	Fe	Cu	Mn
92.4	0.5	0.5	4	0.6
Mg	Cr	Ni	Zn	Ti
1.5	0.1	0	0.25	0.15

Table 3.5 Aluminum 2024 average mass percentage composition (%wt)

2 pieces of 0.6 mm of thickness and 2 of 1 mm were provided, to be able to test multilayered configurations.

Sample number 8 is a Kevlar-Resin plate made of 18 layers of Kevlar fabric 129, style 812 (0.028 g/cm^2 per layer), plus CIBA 914 Epoxy Resin, having an impregnation mass percentage in the range from 30 to 38% of total composite mass. The slab is the one used in the radiation tests described in [59]. The chemical composition and the correspondent elemental weight fractions are reported in Table 3.6.

Sample 9 is Polyphenylsulfone (PPSU), a material characterized by high thermal and mechanical capacity, high impact strength, the ability to be flame retardant and with a good chemical and radiation resistance. It could be used as internal outfitting

Kevlar %wt			
$C_{14}N_2O_2H_{10}$			
C	N	O	H
70.58	11.76	13.43	4.23

Table 3.6 Kevlar average mass percentage composition (%wt)

in spacecraft, also when structural properties are needed, and, consequently treated, as external window materials.

Nextel (samples 10 and 12) is a reinforcement fiber used in the Micrometeoroid and Orbital Debris Protection Systems (MDPS) of typical spacecraft. It has good abrasion resistance, high thermal insulation and thermal mechanical properties, high electrical resistance at elevated temperature. In space Nextel is used as micrometeorite shield and for impact protection from outer space debris, door seals, shuttle tiles, and many others. Its properties used in the simulations are reported in Table 3.7.

Nextel %wt			
Al	Si	B	O
32.6	11.3	4.3	51.6

Table 3.7 Nextel average mass percentage composition (%wt)

Sample 11 is considered as characteristic of the internal layer found in inflatable habitats. It is made of two different layers: a Kevlar fabric style 312 layer (0.028 g/cm^2) and a Coretech layer (0.668 mm) composed by PolyUrethane (PU) and Polytetrafluoroethylene (PTFE) layers, (PU/PTFE/PU). The majority of the bladder can be thought as made by PU (about 0.6 mm) and in the Monte Carlo simulations the PTFE layer has been ignored. Coretech is water repellent and is guaranteeing the insulation (courtesy of the Thales Alenia Space STEPS2 project).

Vectran fibers (Sample 13) are known for their thermal stability at high temperatures, high strength and modulus, low creep, and good chemical stability. The density of the single fiber considered in this project is 1.4 g/cm^3.

Sample 16, PolyBenzimIdazole (PBI) $(C_{20}H_{12}N_4)_n$, is a high performance polymer, with a very high melting point (up to 400 Celsius degree) and exceptional thermal and chemical stability, already used in the sixties by NASA for aerospace and defense applications. In particular, it was used as astronauts' clothing on Apollo

missions, thanks to its non-flammable properties. In the framework of ROSSINI2 project 3 PBI tiles (10 x 10 x 3 cm) with a density of 1.30 g/cm^3 have been procured.

Finally, two different moon simulant materials have been used in the framework of ROSSINI2 (samples 14 and 15).

Johnson Space Center (JSC)-1A Moon regolith simulant dust (sample 14) has been tested in flaks of thin plastic, with a density of 1.76 g/cm^3 (dust not pressed). Its composition has been reported in Table 3.8.

JSC-1A moon regolith simulant %wt											
O	Si	Ti	Al	Fe	Mg	Ca	Na	K	Mn	P	Cr
42.72	19.36	0.97	8.50	12.79	2.88	9.53	1.87	0.88	0.19	0.28	0.02

Table 3.8 Mass composition of JSC-1A moon regolith simulant dust (%wt)

A moon concrete made of moon simulant and chemical binder has been provided (sample 15, courtesy of E. Dini) [60]. This simulant has been named DNA and is based on a natural volcanic material that can be found close to the Bolsena Lake (Italy), whose chemical composition is similar to that of JSC-1A. Ten 10x10x1 cm tiles have been produced using a special 3D printer, with a density of 1.64 g/cm^3. The Lunar Simulant composition is found in Table 3.9.

Moon concrete simulant %wt										
O	Si	Ti	Al	Fe	Mg	Ca	Na	K	Mn	P
42.83	19.82	0.79	8.58	10.33	3.87	9.33	2.00	2.13	0.17	0.15

Table 3.9 Mass composition of Moon concrete simulant dust (%wt)

These materials have been sometimes tested alone on the beam line, in "single material" configuration, varying the sample thickness when many samples of the same material were available. Other times, multilayers configurations have been created, to simulate and test a realistic space exposure situation under radiation beams. Details on the tested multilayers configurations are given in the dedicated chapter (Chapter 5).

Other materials

Also other two materials have been selected for testing.

Three different versions of a material defined Active Nanostructured Magnetic Attenuation Composite (ANMAC), ANMAC-N1, ANMAC-N2 and ANMAC-N10 have been produced by DEMOKRITOS laboratories. A complete concept description can be found in the relative patent, in [61]. Each type of the material was produced as multilayered tiles, alternating polyethylene and layers of nano- and micro-sized Neodymium-Iron-Boron magnetic particles, with random magnetic orientation. Our interest was to show the possible material ability to better stop radiation compared to plain polyethylene and compared to the same ANMAC multilayer, but without magnetizing the Neodymium-Iron-Boron particles.

In the framework of a collaboration between Politecnico di Torino (POLITO) (Polymer laboratories - DISAT) and Thales Alenia Space Italia, some polymeric composites based on epoxies, but with slighter higher hydrogen content, were produced. After the samples' characterization in terms of thermal and electrical properties, samples of 6 cm of diameter of the selected material were made for radiation shielding measurements. The selected material was obtained dispersing Plasticyl HDPE 1501 nanotubes in epoxy resin bisphenol-A-diglycidyl ether, with a 3% concentration.

Chapter 4

Monte Carlo simulations for shielding materials selection

Reliable Monte Carlo simulations are a necessary tool in the framework of this work to determine which materials are interesting to be tested together with the best testing arrangements (e.g. size of the samples). Moreover, it is extremely useful to compare the simulation results with radiation test data and to investigate eventual discrepancies. Finally, Monte Carlo simulations will allow providing estimations of the crew radiation exposure during a space missions, if reliable radiation models describing the GCR and SPE energy spectra are used together with detailed geometric modeling of the surrounding habitat and shielding.

Simulations of radiation interaction with matter have been performed not only on different materials, but also on different configurations. Test beams, SPE and GCR environment were modeled and the obtained results have been used both to support the trade-off activities, described in the previous Chapter, and to carry on future activities, such as radiation tests (Chapter 5) and Moon habitat design (Chapter 6).

Monte Carlo simulation codes Geant4 (interfaced through GRAS) [62], and PHITS [63] have been selected. These codes provide important and powerful tools for medical, radiation protection, space and many other application fields. Their accuracy is affected by epistemic uncertainties, depending on the software implementation, and on the selection of proper physics lists, models of interaction and so on.

An introduction is given in this chapter on Monte Carlo methods for radiation transport, followed by a description of the simulation framework used in this work

and its validation. After that, the simulations made for the material selections are described and finally some additional results are shown.

4.1 Monte Carlo methods for radiation transport

Monte Carlo simulations are implementations of the Monte Carlo methods, techniques using random numbers to solve problems. Repeated random sampling is used to determine the properties of a certain physical phenomenon and being radiation transport a stochastic process, it can be treated with this method.

In the framework of this work, where the goal is to transport cosmic radiation inside a spacecraft and to calculate the fluence/deposited dose in determinate volumes, the main steps of the Monte Carlo code application are the following. For detailed descriptions of this method one can refer to [64].

An event, i.e. a certain ion or proton, is generated according to a certain energy distribution, which could be built after a SPE spectrum, the alpha particles GCR spectrum, and so on. This event can be generated with random position, direction, energy and time and travels in line segments of random length until an interaction takes place. Particles are followed step-by-step when moving in a medium and at each step nuclear and electromagnetic processes are simulated. Generally, seven or eight variables can be used to define the state of the generated event.

For each kind of considered particle, many independent variables exist to define the problem, and they are random variables, which can be described using a Probability Density Function (PDF). Examples are how long the particle travels before an interaction, whether the interaction takes place, which kind of interaction and with which atom, the outcome of the interaction, such as scattering angles or produced secondary particles yields etc. For instance, when considering the simplest case of a photon traveling inside matter, the photon can exchange energy with an electron in the atom, consequently scattered changing direction, or it can be absorbed, terminating its virtual history. Relative probabilities, based on experimental data and theoretical formulas, are assigned to each possible event, in this case scattering or absorption. For the general case, the expected length of the traveled track before an interaction occurs is calculated by polling all the applicable processes at each step. Energy dependent cross sections are included in the codes and used to determine the

mean free path for a given process, which is the inverse of the macroscopic cross section. The code tracks each generated particle, and, if any, its secondary particles, until they are finally absorbed.

One can imagine the complexity of a code taking into account all the possible interactions of all radiation types inside a medium. Examples of complex physics implemented in a Monte Carlo code can be found in the Geant4 Physics Reference Manual, available online [8].

Importance sampling is generally used in these codes, i.e. to improve convergence more samples are inserted in the region where the probability density function describing the problem is largest. For instance, when generating primary protons according to a SPE spectrum, more protons will be generated with lower energies, according to the quasi-exponential energy spectrum.

For the central limit theorem, the Monte Carlo estimate is distributed around the true value as a Gaussian, therefore the convergence goes as $1/\sqrt{n}$ in any dimension, with n being the number of events contributing to the quantity, for instance the number of particles depositing dose in a certain volume. For each desired quantity, the relative standard error can be estimated by $1/\sqrt{n}$. However, many codes do not estimate systematic errors due to nuclear model uncertainties.

Several Monte Carlo codes have been developed to simulate radiation transport through matter. They differ in the types of nuclear databases used and in how they treat nuclear interactions, secondary radiation and geometries modeling. Considering the complexity of a space radiation simulations, not all the codes can be used to realistically reproduce the phenomenon.

In this work, Geant4 Radiation Analysis in Space (GRAS) interface to GEometry ANd Tracking (Geant4) and Particle and Heavy Ion Transport code System (PHITS) codes have been used. A brief description of the tools follows.

Environmental models are usually the boundary conditions for these codes and the geometric level of complexity is generally high.

4.1.1 GRAS/Geant4

GRAS v3.3 [65] [66] is an interface to Geant4 [8], a Monte Carlo simulation toolkit for studying the transport of particles through matter considering several kinds of

interactions and physical processes in complex geometries. One can find details on the code and its physics models in [8]. Geant4 offers different models to treat several physical processes including ionization, Bremsstrahlung, photoelectric effect, Compton scattering, elastic and inelastic hadronic interaction, nuclear capture, and particle decay.

To treat complex geometries, GRAS code can use the Geometry Description Markup Language (GDML) format [67] files as input.

GRAS analysis types include cumulative effects, such as Total Ionizing Dose (TID) or Non Ionizing Energy Loss (NIEL) dose. Specific modules have been developed for the evaluation of the effects of radiation to humans: “Dose Equivalent” analysis, based on LET quality factors, and “Equivalent Dose”. Other possible modules are "Fluence of primary or secondary particles crossing a volume boundary", "Dose", "LET" and “Track Length” modules. All analyses can be applied to any user-defined set of volumes or surfaces, chosen among those present in the geometry model. Results are saved as histograms or “tuples” (tabular data for a post-analysis), while basic summary quantities are also output in simple text format (.csv).

Radiation interactions with matter and the consequent energy deposition by the particles and their fragment products are considered in Geant4 by different combinations of standard models, such as ElectroMagnetic (EM), BInary Cascade Model (BIC), Statistical MultiFragmentation Model (SMF) and Fermi Breakup Model (FB) [68]. Standard electromagnetic physics in Geant4 covers the energy range from 250 keV to 1 PeV, including various processes such as ionization and multi-scattering as well as elastic and inelastic processes for recoil and fragmentation reactions. BIC model is used to study the interaction of particles with atoms and nuclei of the target and is valid for ions with mass number greater than one and energy less than 10 GeV/nuc. SMF model deals with multifragment break-up of excited residual nuclei for energies greater than 3 MeV/nuc and statistical weights determine the relative probability of different break-up channels. FB model treats the decay of cold or excited fragments whose mass number is less than 16, with lifetimes longer than their decay time, predicting the final state of excited nuclei.

In the framework of this project many pre-compiled physics lists have been used for the Geant4/GRAS simulations and the results have been compared. Among those, one can find:

- QGSP BIC and QGSP BIC HP
- QGSP BERT and QGSP BERT HP
- Shielding
- FTFP BERT and FTFP BERT HP
- FTFP INCLXX and FTFP INCLXX HP
- QGSP INCLXX and QGSP INCLXX HP
- QBBC EMY

In Table 4.1 a legend is given for acronyms of the physics models while Figure 4.1 gives a picture where the applicability of each model is reported, in terms of particles and energies.

FTF	Fritiof string model
QGS	Quark-gluon-string model
P	Precompound model
BERT	Bertini intranuclear cascade model
INCLXX	Liege intranuclear cascade model
BIC	Binary cascade model
HP	High precision neutron model
QBBC-EMY	Binary Cascade and Electromagnetic Option 3
Shielding	FTFP BERT HP with Ion Quantum Molecular Dynamics model

Table 4.1 Geant4 physics model acronyms

A validation of the simulation set-up against experimental data has been performed and also the differences among different compatible physics list/options have been investigated before starting with the simulations campaigns.

4.1.2 PHITS

PHITS [69] is a general purpose Monte Carlo code for particle transport simulations which can deal with the transport of almost all particles and can be used in the field of space radiation to study the impact of the radiation environment on spacecrafts. PHITS is based on the Nuclear Meson Transport Code and Jet -Aa Microscopic Transport Model (NMTC/JAM) [70].

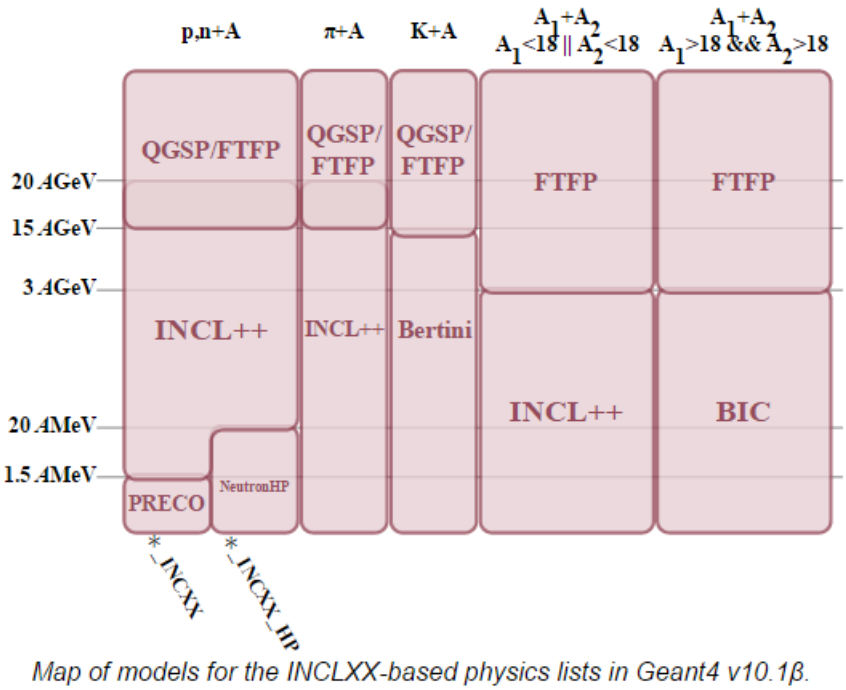

Fig. 4.1 Maps of models for the Geant4 INCLXX-based physics lists [8].

It is possible to estimate the particles average behavior calculating various physical quantities as flux and deposition energy in a certain region, using “tallies”, such as dose, flux, LET, secondary production, and many others, which can be computed in each region defined in the model. For neutron induced reactions in the low energy region, PHITS employs the cross sections from Evaluated Nuclear Data libraries. For high energy neutrons and other particles, two models are implemented, JAM and JAERI Quantum Molecular Dynamics (JQMD), to simulate the particles induced reactions up to 200 GeV and the nucleus-nucleus collisions, respectively. Figure 4.2 reports the applicability of each PHITS physics model, in terms of particles and energies.

In a PHITS simulation, the user has to specify the geometry of 3 dimensional virtual space and information of source particles, and then it is possible to tally various quantities by simulating particle motions in the virtual space. The 3D virtual space setup is built using General Geometry (GG) or Combinational Geometry (CG) concepts. In addition it is possible to use SimpleGeo [71], a free software developed by CERN, which is a Graphical User Interface (GUI) to create geometries in formats compatible with different Monte Carlo codes such as PHITS or FLUKA.

Furthermore, parallelization of runs in PHITS is allowed and output formats are .txt files for numeric values and .eps files for images.

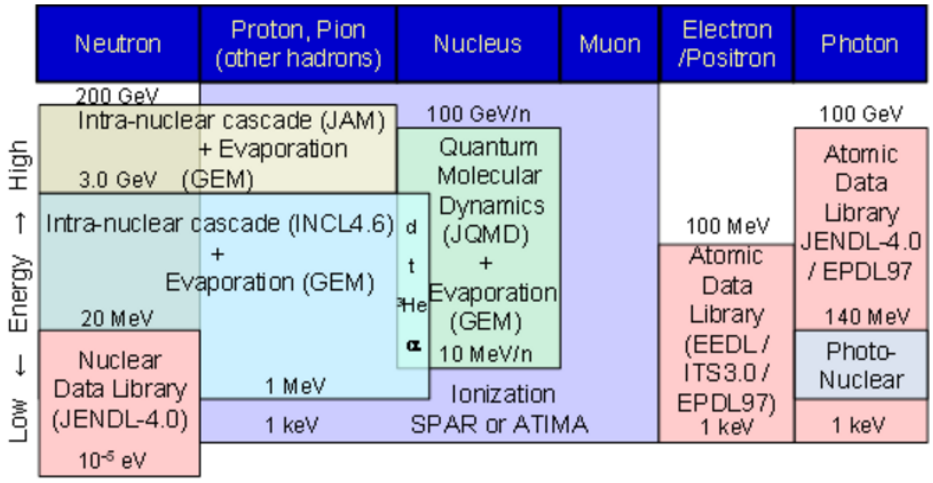

Fig. 4.2 Map of PHITS physics models and their applicability.

4.1.3 Simulations Errors

When the Monte Carlo method is applied to equations describing stochastic process, the random walk can be identified with the process itself. Furthermore, in this case, it is a Markovian process, as the destiny of a particle depends only on its present properties, not on previous simulation events. We are indeed dealing with "virtual" particles which are not interacting with each other, but only with the target material. Also, in the interaction, only the particles are modified, as the material in which they are moving remains constant in time.

When working on shielding design and optimization, generally the user is interested in the expectation values of the quantities (average of fluence and dose) at some space point or region (in a certain human organ, or in some electronic components) and a statistical error.

As statistical accuracy depends on the number of generated histories, in this work the number of generated primaries was always selected high enough to decrease the statistical errors to less than 1%. Before each simulation campaign, tests have been carried out to study dose and fluence variations in volumes of interest (for instance, verifying that a smooth depth-dose distribution was obtained).

In general, also other factors are able to affect the accuracy of the simulation, such as:

- errors on models and data from which the probability distribution functions are obtained, also including errors due to data interpolation
- simulation artifacts, as algorithms are not perfect
- errors and/or approximations on geometry and material models

In this thesis only statistical errors of the simulations are given, and they do not include neither errors on physics models and data-sets, nor on the beam/environment models used to generate the particles.

Different approaches were applied to error derivation for the two MC codes. PHITS already calculates the relative error for all the output quantities, and it can be used directly. On the other hand, Geant4 results are obtained from particle-by-particle data dumped in histograms, and errors are obtained as the standard deviation of the mean values.

4.2 Simulation framework

Simulations have been run on Thales Alenia Space Italia 8x Dell PowerEdge M620 blade servers using Intel Xeon E5-2670v2 processors, with 64 GB of memory per node, leveraging Mellanox FDR InfiniBand interconnects. 10 nodes are available and a total of 20 cores per node are present. The software/code versions used for this work are:

- Geant4.10.01 through its interface GRAS v3.03 as Monte Carlo tool
- PHITS v2.80
- Root v5.34/23 to carry on the data analysis [9]
- Python v2.7 to further analyze the data
- Fastrad v3.7 to create the complex geometrical model in a Geant4 compatible format (ability to export geometrical models into a gdml file)

4.3 Validation simulations

The simulation campaign started with an activity aimed to validate the simulation framework. To do so, comparisons between experimental Bragg curves[1] data available at NASA Space Radiation Laboratory (NSRL) website (https://www.bnl.gov/nsrl/userguide/bragg-curves-and-peaks.php) and PHITS and Geant4 simulations have been performed with protons and heavy ions of energies comparable with GCR and SPE spectra.

HDPE (with a density of $\rho = 0.97$ g/cm^3) has been selected as target because of the large amount of available data found in literature: at NSRL there is an array of HDPE, with varying thicknesses ranging from 16 cm down to 250 microns, that can be remotely inserted into the beam line and used at the beginning of each beam day to measure the beam kinetic energy.

For these first Bragg peak simulations, a simplified setup was created: HDPE was modeled as a single volume and then dose deposition was calculated into small slices inside the volume itself. Results were then normalized with respect to the dose deposited into the first thin slab. MC simulation statistical errors (not considering errors on nuclear models) are always lower than 0.1%, unless differently specified, and not reported in the plots. Error estimations of the experimental data were not available.

Typical Bragg peak curves are shown for 103 and 252 MeV protons in Figure 4.3. The solid symbols represent the experimental data obtained at NSRL, while the other curves were obtained with PHITS and Geant4 simulations. One can see that the range of 252 MeV protons in HDPE is about 37 cm.

The small differences between the experimental data and the normalized simulation results are mostly due to the fact that the modeled detector in our simulations is a simplistic approximation of the real one. Our detector has been assumed to be a slab of HDPE, therefore a small fraction of the protons not registered by the real detector, affected by the leakages of a reduced field of view, is instead present in the simulations, slightly increasing the normalized dose, in particular for lower energy particles.

[1] Bragg curves are graphs showing how the energy loss is changing versus the material thickness and the Bethe-Bloch equation is quantitatively describing that loss

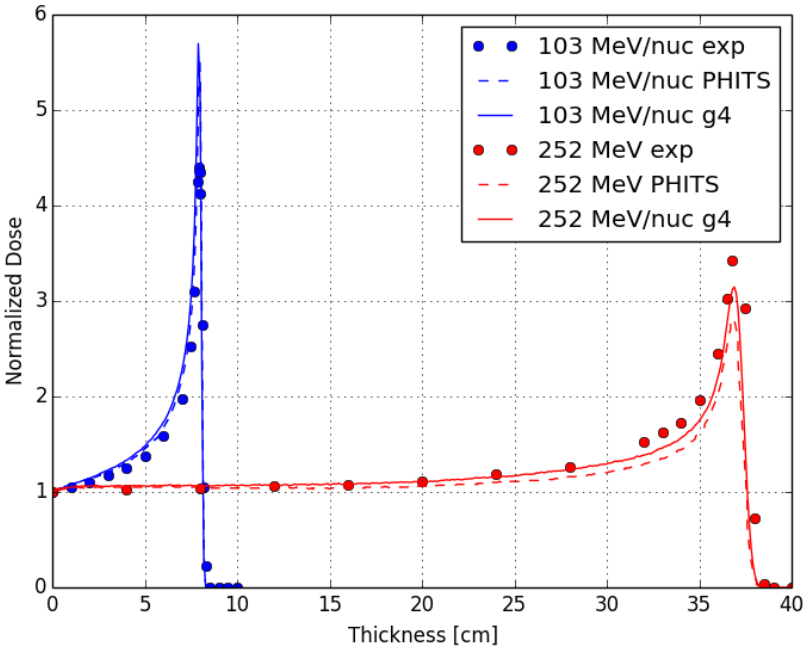

Fig. 4.3 Bragg curve of 103 and 252 MeV protons in HDPE as measured at NSRL and comparison with PHITS and Geant4 simulation results.

When considering heavy ion beams this phenomenon is less important: in this case the majority of the dose is released by the high energy primary ions, which are reluctant to change direction as much as protons do, so that a smaller number of primary particles escape the detector field of view, as can be noticed in Figures 4.4, 4.5 and 4.6.

Moreover, the Bragg curve for heavy ions is characterized by a tail that is not evident in the proton curve shown in Figure 4.3: this happens because the primary ions can be broken up into lower Z fragments when interacting with the target material nuclei and in general these lighter fragments will have a longer range than the primary ions, producing the so-defined "tail".

These curves are very useful to show the competing effects of ionization energy loss and fragmentation. When low energy beams are used, as in Figures 4.3 or 4.4, it is possible to see how the Bragg curve increases very quickly with target thickness due to the fact that as the energy of the incoming particle decreases, dE/dx increases. These are two examples in which ionization energy loss dominates over the particle behavior.

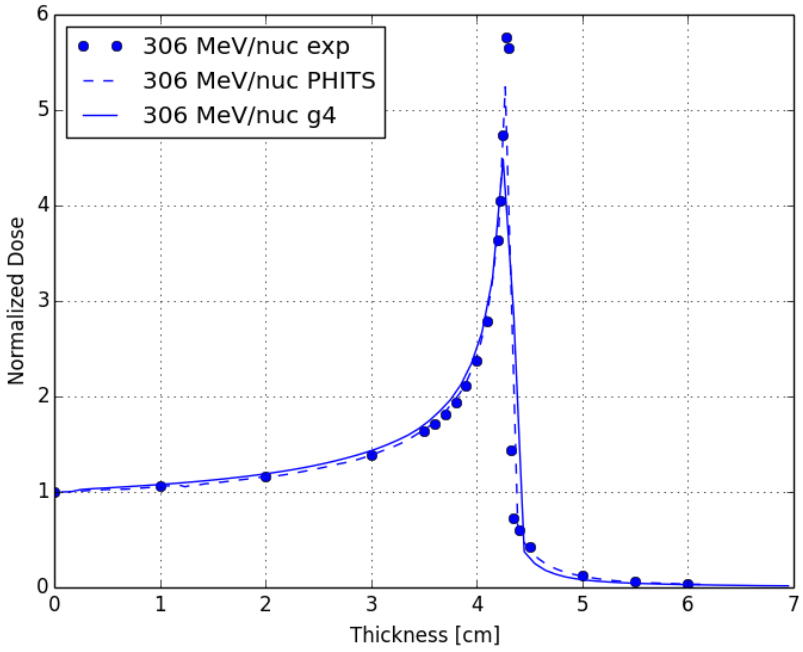

Fig. 4.4 Bragg curve of 306 MeV/nuc iron beam in HDPE as measured at NSRL and comparison with PHITS and Geant4 simulation results.

On the other hand, when the beam energy is higher, dE/dx is lower and the primary beam fragmentation begins to be important and is responsible of the steeper initial decrease of the Bragg curve for heavy ions. Also, the energy deposited by lower LET fragments is lower than the one released by the primary ions and this concurs to further decrease the curve. This phenomenon is visible for example for increasing iron beam energies in Figure 4.6, and even more evident for 963 MeV/nuc ^{56}Fe in Figure 4.7.

It is possible to see how PHITS is able to reproduce the dose deposition very well for different energies. On the other hand, Geant4 does not seem to be able to reproduce high energy iron beam well, as can be seen in Figure 4.7, where also one of the latest physics library, QBBC-EMY has been used. The reasons of this discrepancy are still under investigations, but probably they are due to nuclear fragmentation models implemented in Geant4. Simulations with Geant4 have also been carried out using different physics lists (among those recommended for HZE physics), however results are reported for different physics lists only when there is not an agreement between them.

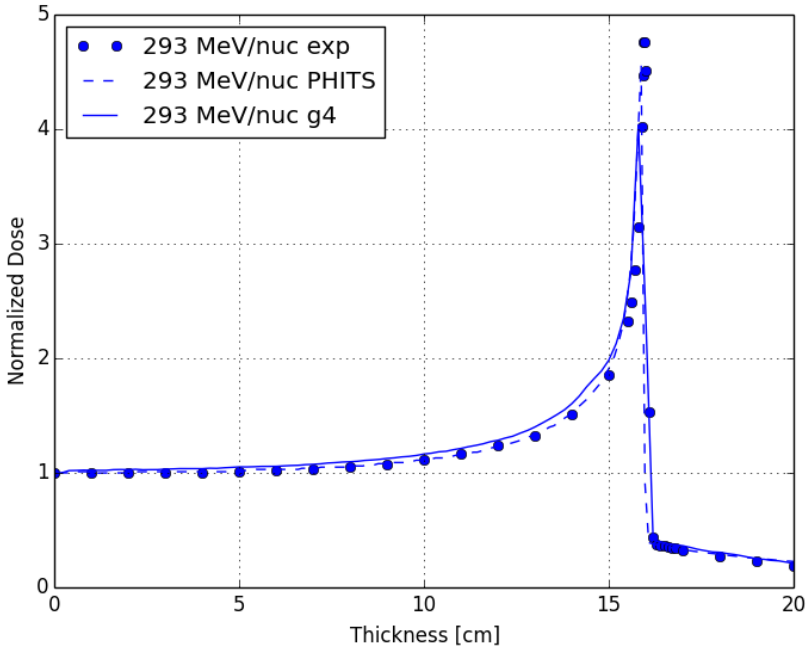

Fig. 4.5 Bragg curve of 293 MeV/nuc carbon beam in HDPE as measured at NSRL and comparison with PHITS and Geant4 simulation results.

4.4 Trade-off simulations

Single material simulations have been made to compare different materials from the point of view of the radiation shielding efficiency. The geometrical set up was kept constant varying the target material thickness, in g/cm^2. Fixed aerial densities values were used instead of thicknesses in cm to obtain a comparison of targets characterized by the same mass, since one of the most important cost parameters of a space mission is the total launched mass.

The simulations have been carried out using a pencil beam source, perpendicular to the target material surface. The beam angular distribution was assumed to be a delta Dirac function at zero θ (where θ is the angle between the beam direction and the normal to the surface). Different energy spectra were implemented, to reproduce GCR and SPE sources. Details on the different sources follow. Being SPEs easily shielded by passive shielding, the main focus of this work has been on the more problematic GCR population.

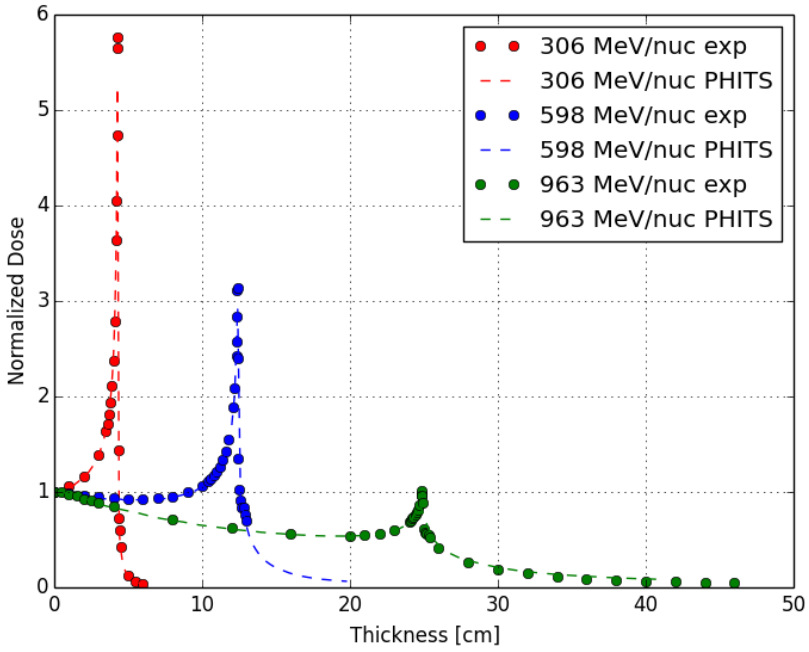

Fig. 4.6 Bragg curve of different energies iron beams in HDPE as measured at NSRL and comparison with PHITS simulation.

In the previous section it has been shown that when dealing with protons at typical SPEs energies the agreement between both the codes and the experimental data is very good. However, some differences were found when comparing simulations performed with high energy ions, as in the GCRs case. For this reason, PHITS code was selected as main dose reduction simulation code, presenting a better agreement with the experimental data. Geant4/GRAS, however, has been used anyway throughout this simulations work for a subset of materials to provide comparisons with PHITS.

In the following paragraphs, the description of the simulated sources and geometries is given, followed by the simulation results.

4.4.1 Galactic Cosmic Rays source

The reference mission scenario used in the framework of this work is a long duration deep space mission during a period of solar minimum, characterized by a higher flux of GCRs than a period of solar maximum. In this scenario, GCRs exposure becomes important. All the ions with atomic numbers ranging from Z=1 to 26 have

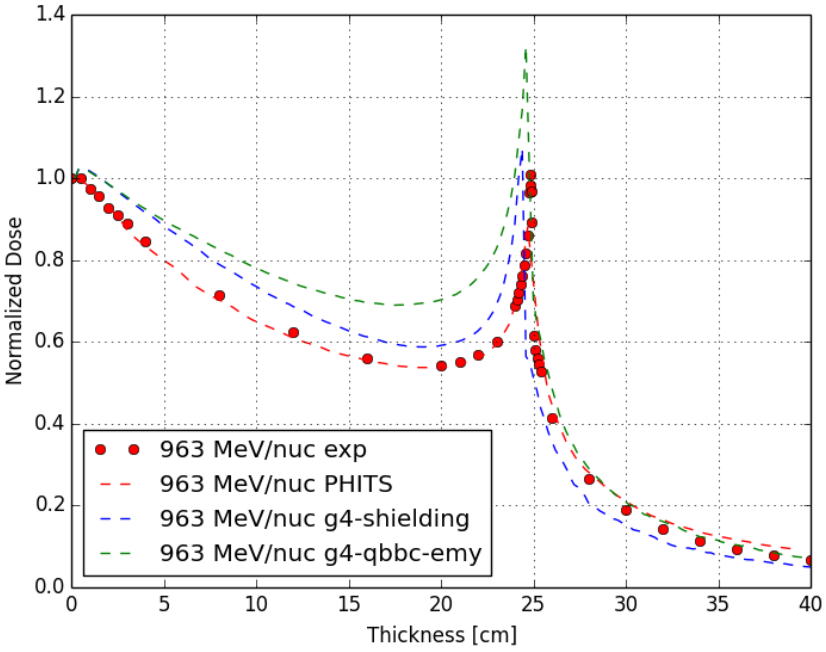

Fig. 4.7 Bragg curve of 963 MeV/nuc iron beam in HDPE as measured at NSRL and comparison against simulation performed with PHITS and different Geant4 physics lists.

been considered using the ISO model 15390 (suggested by ECCS 10-04 standard as reference GCRs model) at solar minimum without magnetic cut-off to consider the worst case situation. Figure 4.8 shows the spectra used in the simulations, while Figure 4.9 reports their abundances.

4.4.2 Solar Particle Events sources

A solar proton model calculated starting from the average fluxes obtained by satellites observations was chosen for ROSSINI2 SPE dose reduction calculations. Considering the limitations of King and Jet Propulsion Laboratory (JPL) models (data sets used in these models are in fact incomplete, since there are limits to proton energy range and neither model includes the full 3 solar cycles for which high quality space data are available), the Emission of Solar Protons (ESP) model was chosen [72], which predicts an initial distribution as a broken power law in the event fluence. ESP uses data from the last 3 complete solar cycles (20-22) and is the current model described in the ECSS standards (European Cooperation on Space Standardization).

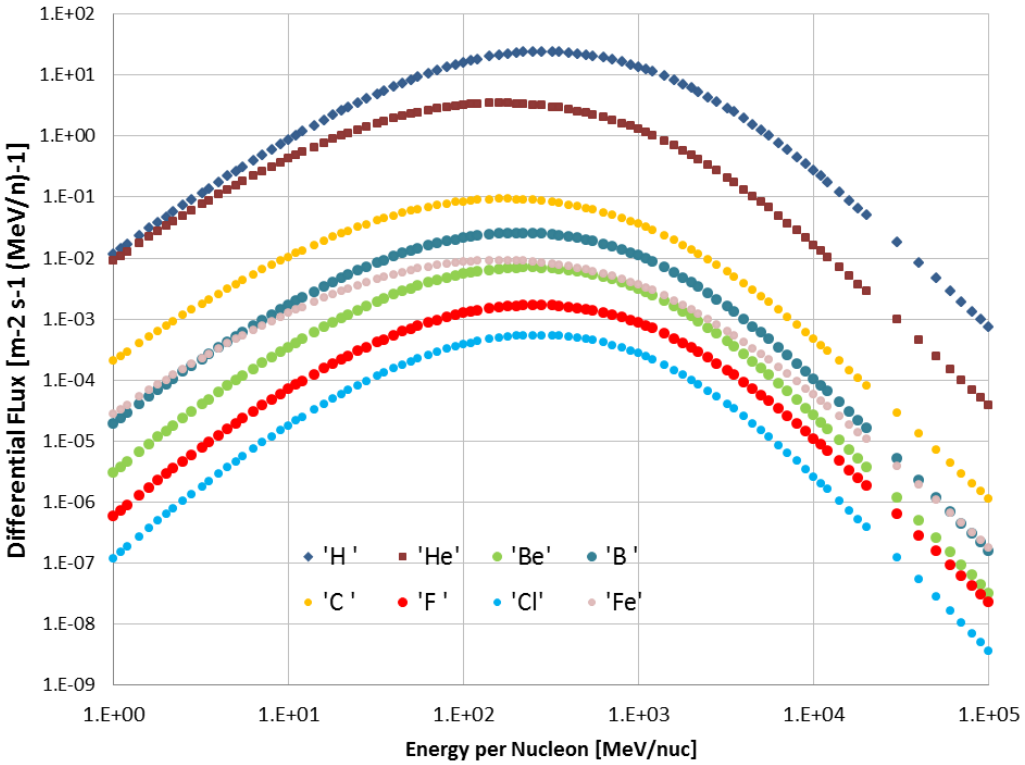

Fig. 4.8 GCR differential flux for selected ions, as per ISO15390 model.

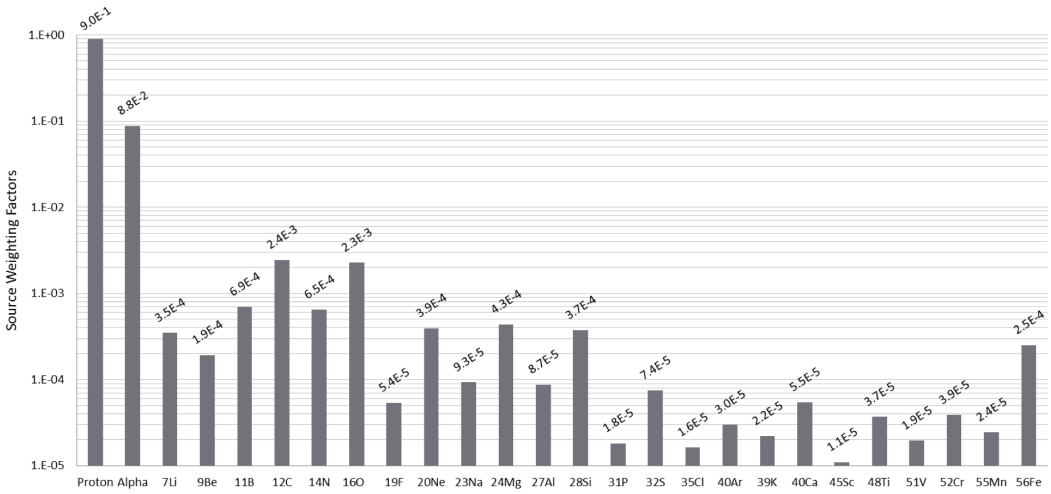

Fig. 4.9 Abundance of the different ions in GCRs composition used in the Monte Carlo simulations.

Figure 4.10 reports the proton differential fluence calculated using the Space Environment Information System (SPENVIS) for a 10 year mission in near-Earth deep space.

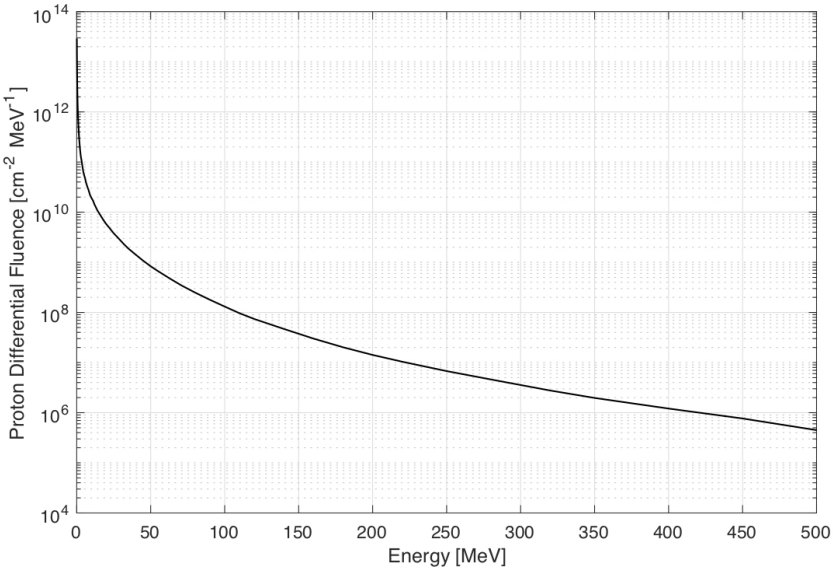

Fig. 4.10 ESP long term differential fluence of solar protons for a 10 years-long mission, 7 of which in solar maximum and 3 in solar minimum, with a confidence level of 95%, without considering the magnetic shielding of Earth's magnetic field - obtained with SPENVIS.

Another model was selected to be used for a subset of simulations, to consider the worst case exposure: the August 1972 event [73]. This event is considered as one of those delivering worst-case doses to typical spacecraft shielding (1-10 mm), where particles of energy 10-70 MeV give an important contribution. During this event a peak flux near the Earth in excess of 10^6 protons $cm^{-2}s^{-1}$ with energy above 10 MeV was recorded.

4.4.3 Materials and geometry

Table 4.2 contains the list of the principal materials considered at the beginning of the study, for the trade-off simulations. These simulations are considering a whole range of different material categories, to have indications on their radiation shielding properties, before proceeding with the material selection, described in the dedicated chapter.

Aluminum	Ammonia borane	Aluminum boride
Beryllium hydride	Epoxy	Kapton
Iron High density	Polyethylene	Lithium hydride
Kevlar	Lithium borohydride	Mylar
Lead	PEO	Mars simulant
Moon concrete	PMMA	Sodium borohydride
Nextel	Polyetherimide	Polymide
Silicon boride	Polypropylene	Silicon rubber
Titanium hydride	Polysulfone	Teflon
Water	Urea	Zirconium hydride

Table 4.2 List of the principal considered materials in ROSSINI2 study

In Figure 4.11 the set-up for dose reduction simulations is shown. The dose is registered into a simple virtual detector, made of a water slab 2 cm thick, placed behind the target made out of the material under study whose thickness is varying. The detectors is a cylinder of radius 20 cm. Also the target materials placed in front of the detector are simulated with a cylindrical shape.

Simulations were performed with at least 3 different radiation sources: mainly GCRs, but also, for a subset of materials, ESP solar protons and August '72 solar particle event, created as pencil beams.

Default options have been initially used for PHITS simulation and physics parameters. However, when simulating hydrides, some discrepancies have been found and, for this reason, part of the simulations have been carried out again, using optimized nuclear models.

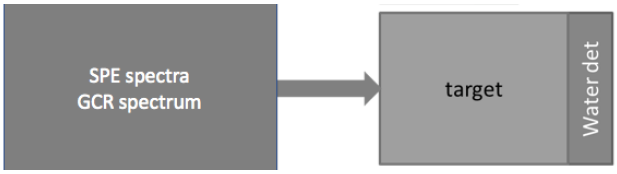

Fig. 4.11 Set-up for dose reduction simulations. Pencil beam have been reproduced perpendicular to the target surface.

In the following paragraphs results are given for each source.

4.4.4 Results

Doses have been calculated as absorbed energy in the detector volume for a normalized number of incoming particles (MeV/source - where source refers to the generated particles).

Results are here presented as dose normalized to the scenario without shielding layer, i.e. the dose registered in the detector after the shielding material divided by the dose registered in the unshielded detector:

$$D_N = \frac{D_t}{D_0} \tag{4.1}$$

where D_0 is the dose in the detector without any shielding material in front of the detecting volume, whereas D_t is the dose with the shielding material of a certain thickness t.

As both D_0 and D_t are characterized by a statistical error, also D_N will be. We can assume that D_0 and D_t have random and uncorrelated errors and therefore it is possible to perform error propagation obtaining the relative error on D_N as the square of the addition in quadrature of the relative errors on D_0 and D_t.

Dose reduction ΔD for ROSSINI2 materials has been calculated using the following formula:

$$\Delta D = 1 - D_N \tag{4.2}$$

Also dose reduction per target aerial density has been defined, dividing the previous quantity by the target aerial density:

$$\delta D = \frac{\Delta D}{t} \tag{4.3}$$

where t is the target thickness expressed in g/cm^2

GCRs results

Figures 4.12, 4.13 and 4.14 report the normalized dose in the water detector with different target thicknesses when primary particles generated through the GCR spectrum (with ions ranging from Z=1 to Z=26) for selected subsets of materials:

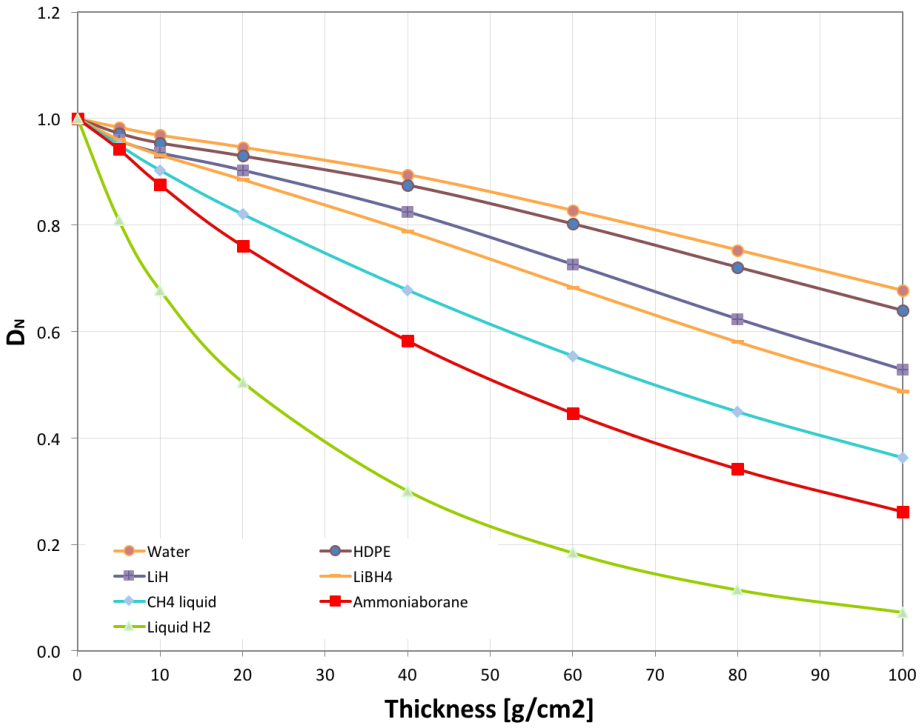

Fig. 4.12 Normalized dose in water detector varying the target thicknesses when primary particles are generated through the GCR spectrum [with ions ranging from Z=1 to Z=26]. Results were obtained with PHITS simulations and simulations errors are less that 1%.

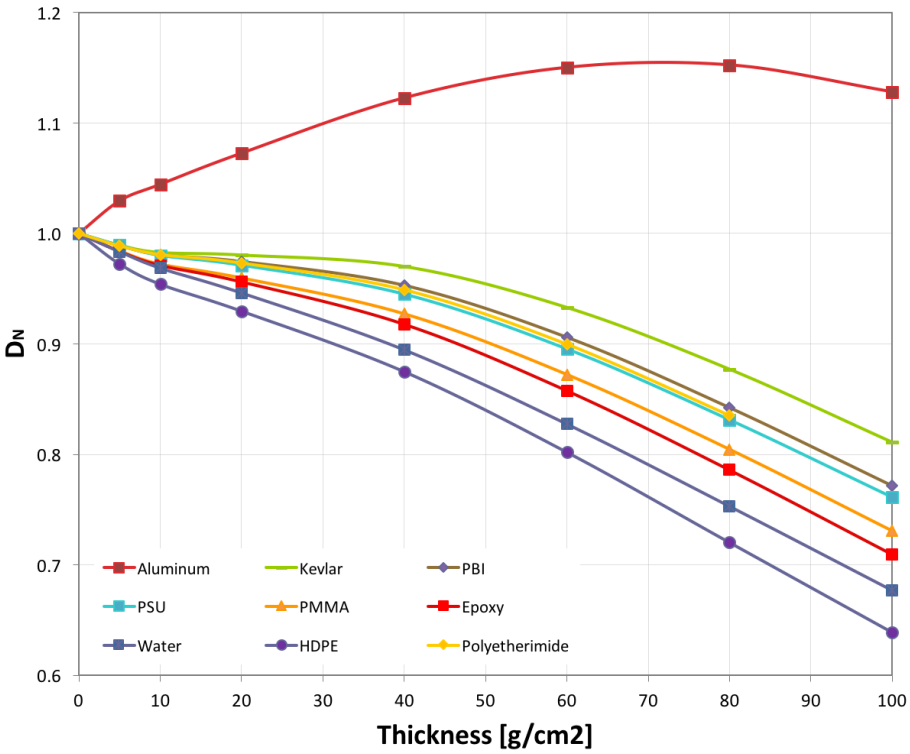

Fig. 4.13 Normalized dose in water detector varying the target thicknesses when primary particles are generated through the GCR spectrum [with ions ranging from Z=1 to Z=26]. Results were obtained with PHITS simulations with errors less than 1%.

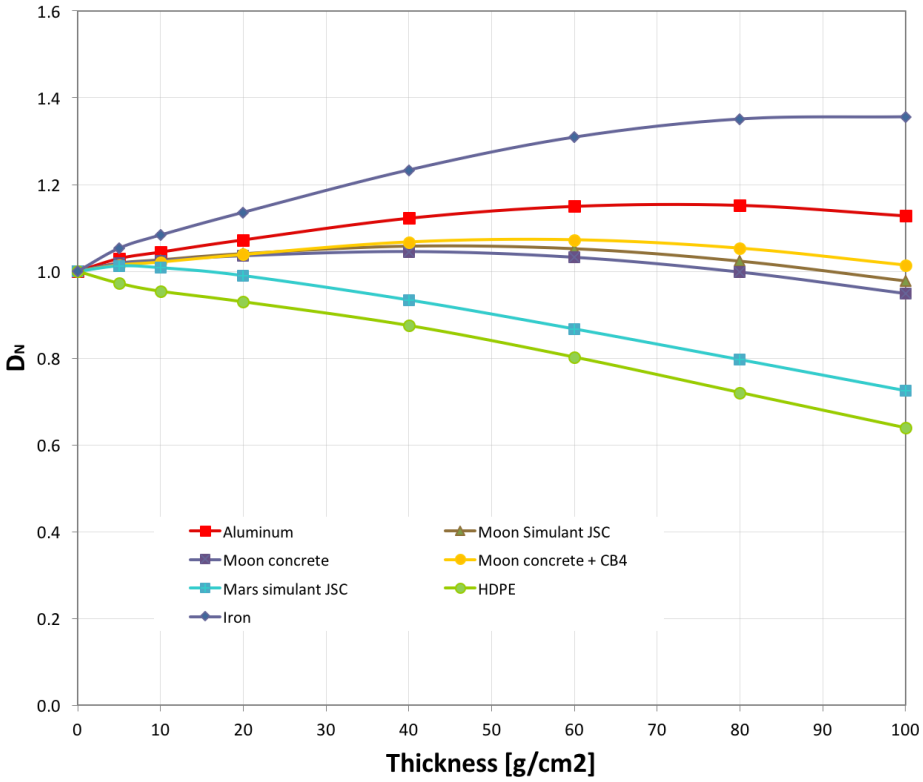

Fig. 4.14 Normalized dose in water detector varying the target thicknesses when primary particles are generated through the GCR spectrum [with ions ranging from Z=1 to Z=26]. Results were obtained with PHITS simulations with errors less than 1%.

materials with high hydrogen content, mainly polymeric materials and in situ re-utilization (ISRU) materials.

A focus on the first interaction points for selected materials is presented in Figure 4.15, where dose reduction results for three different thicknesses of shielding materials, 5, 10 and 20 g/cm^2 are reported for a subset of targets.

Control materials have been introduced in the simulations, in some figures results are reported for iron. It is possible to see that when trying to shield GCR ions with these high Z number materials, the dose delivered to a detector placed behind them is even increasing.

As expected, from these simulations it resulted that even employing very large thicknesses of materials, it is not possible to totally shield GCRs.

Hydrides, i.e. materials with high hydrogen content, result to be the best at shielding GCRs.

A shield made of LiH, one of the best material to shield radiation, would lead to a reduction of about 30% of the unshielded dose, using 60 g/cm^2 of material. However, such a thick shielding would be a not feasible option for a space mission. It is clearly shown how the atomic weight affects the dose reduction to a great extent, leading to an increase in the after target dose when hydrides such as TiH or ZrH are employed. Ammonia Borane shows the best performances in terms of GCRs dose reduction, closely followed by LiH and $LiBH_4$. Among these materials, LiH is considered the best shielding material, due to its greater compatibility with the spacecraft environment with respect to the others.

HDPE resulted the best polymeric material from a radiation protection point of view. Moreover, it is important to consider the possible multifunctionality of the materials. For instance, epoxy can be employed in the production of CFRP, therefore its use in space becomes very attractive.

Finally, dose reduction per aeric density values are given for a subset of materials in Figure 4.16. As expected, dose reduction from GCR radiation tends to constant values after an initial transient, depending on the material type. This is due to the production of a huge number of secondary particles, which give their contribute to the total dose. In particular, a great quantity of neutrons is generated with very long ranges.

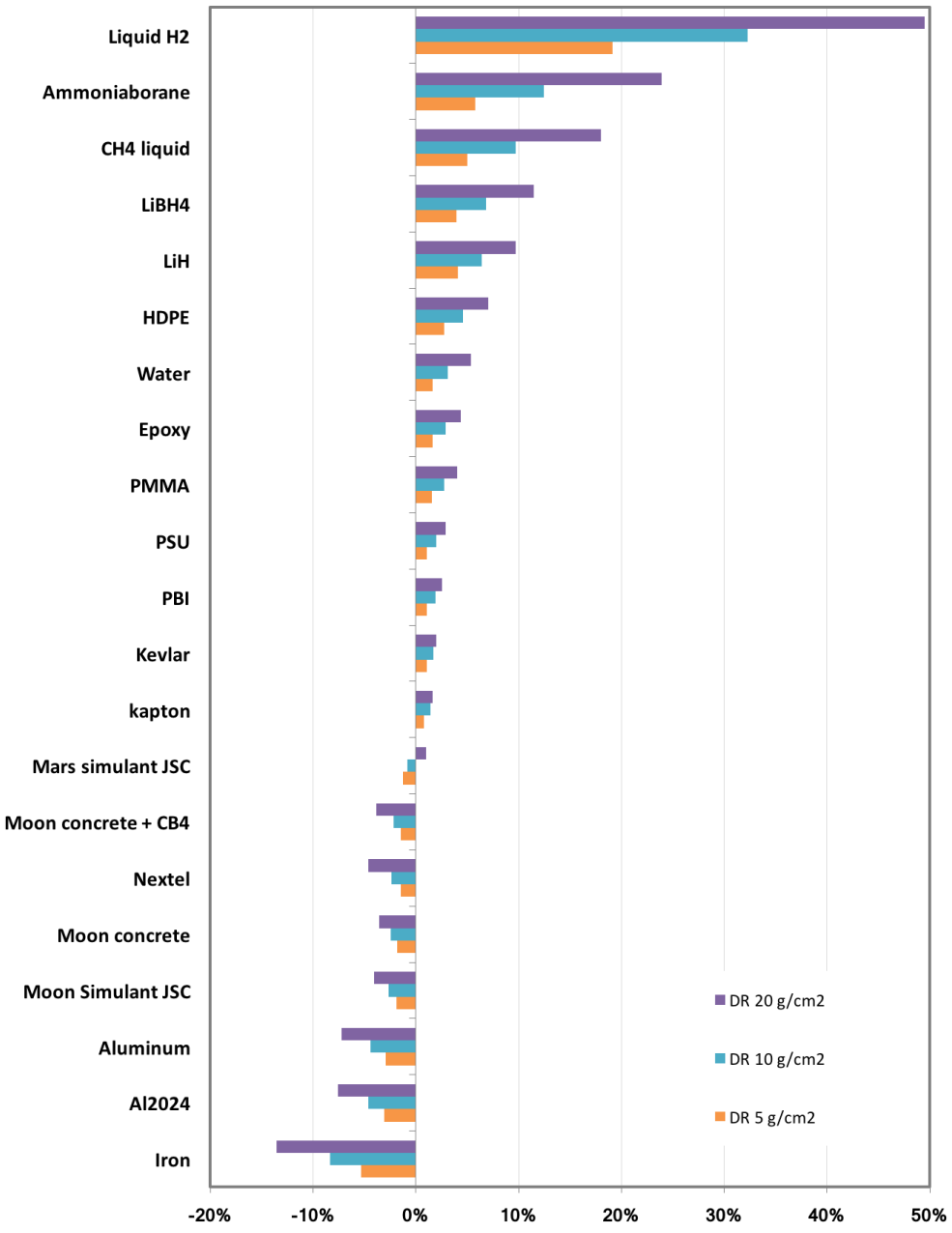

Fig. 4.15 δD in different targets when primary particles are generated through the GCR spectrum [with ions ranging from Z=1 to Z=26] for 3 different thicknesses, 5, 10 and 20 g/cm^2. Results were obtained with PHITS simulations with errors less than 1%.

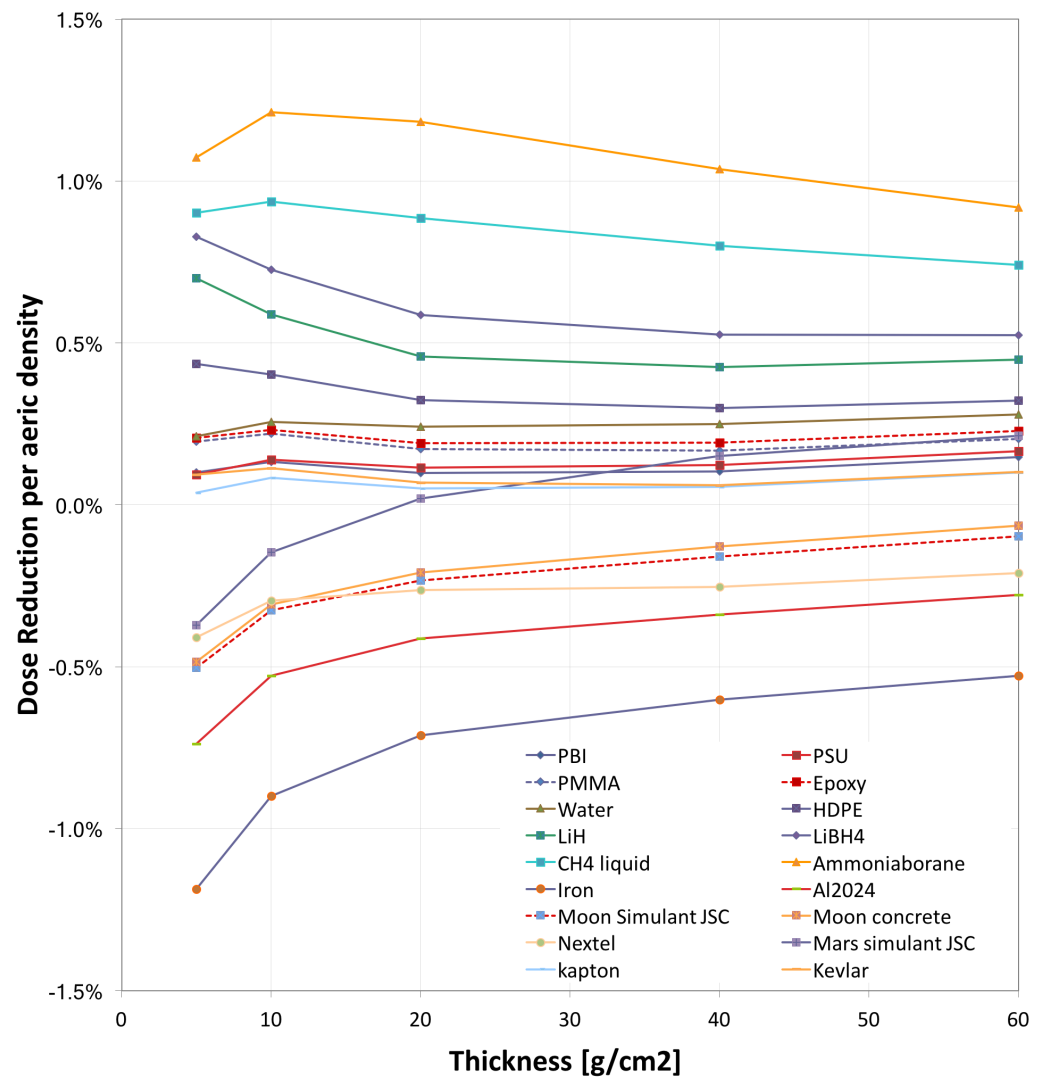

Fig. 4.16 GCR dose reduction versus target depth for a subset of materials. Results obtained with PHITS simulations with errors less than 1%.

A study has been carried out with GCRs on a subset of 3 materials to investigate the influence of the detector dimensions on the dose reduction. Even if the relative material performances are not varying we can see in Figure 4.17 how dose reduction is decreasing faster with a smaller detector (radius 10 cm instead of 20). Since a pencil beam GCR source was used for the 1D simulations, this effect is mainly due to the fact that GCRs have the ability to cause ionization even far away from their primary path, and dose is still deposited by secondary particles (e.g. δ-ray electrons) centimeters away from the primary beam.

Further studies should be carried out to investigate the results dependency on the detector size and to harmonize the detector selection in the framework of future works.

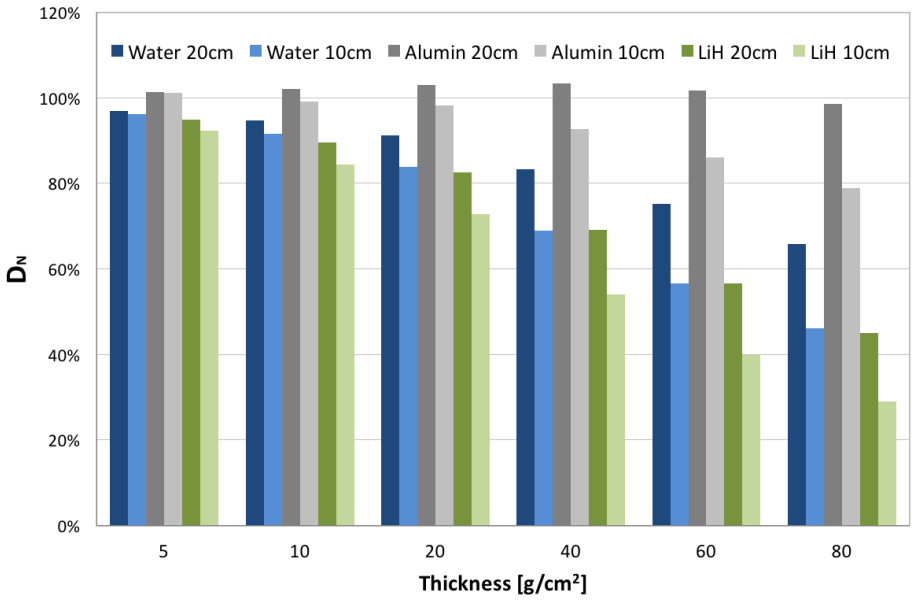

Fig. 4.17 GCR normalized dose for a subset of 3 materials as a function of their thickness, calculated for two detector radius, 20 and 10 cm. Results obtained for PHITS simulations with errors less than 1%.

SPEs results

In Figure 4.18 dose reduction results for four different thicknesses, 1, 2, 5 and 10 g/cm^2, are reported for different materials when considering solar protons generated through the ESP spectrum.

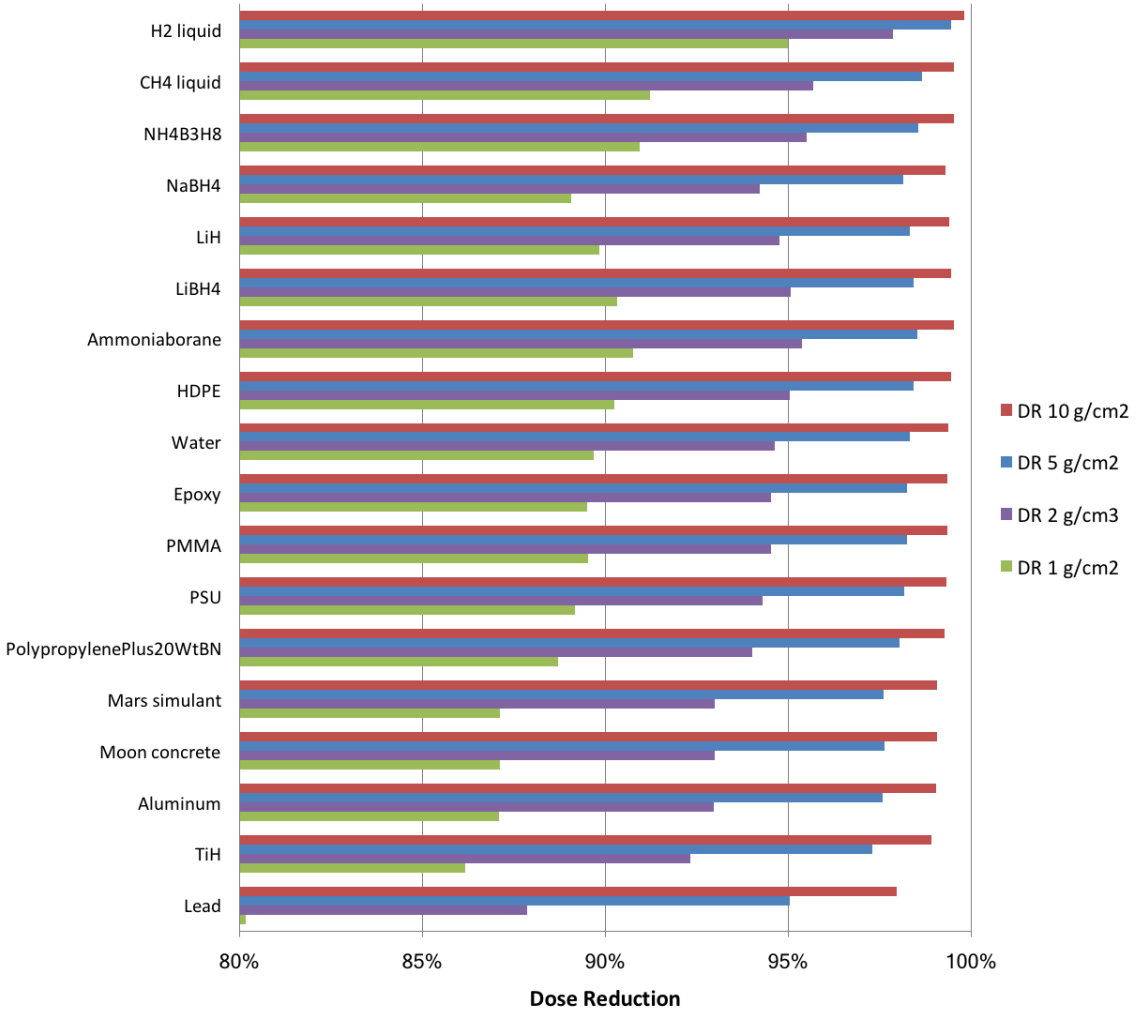

Fig. 4.18 Dose reduction in different targets shielding particles generated through the ESP spectrum (considering only solar protons) for 4 different thicknesses, 1, 2, 5, 10 g/cm^2. Results obtained with PHITS simulations with errors less than 1%.

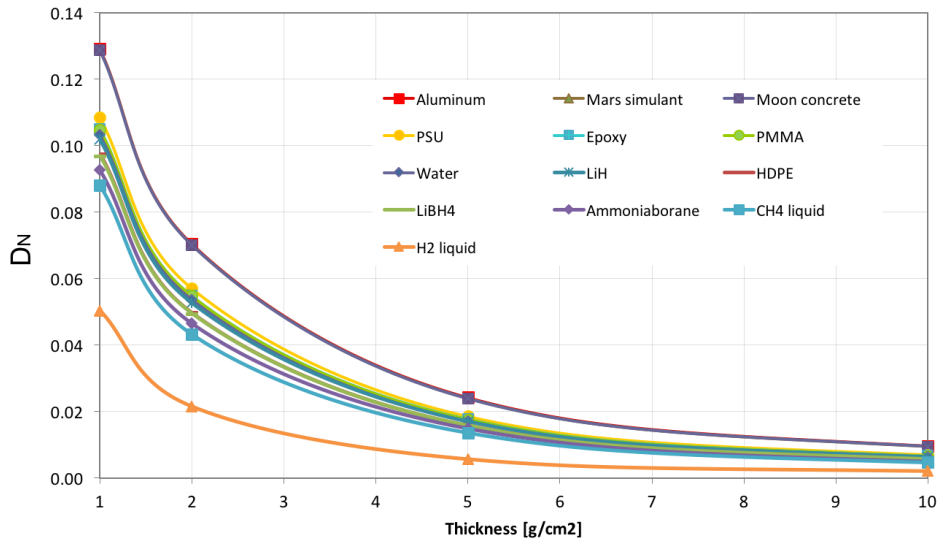

Fig. 4.19 Normalized dose in water detector obtained for selected targets with thickness up to 10 g/cm^2 when particles are generated through the ESP spectrum (considering only solar protons). Results obtained with PHITS simulations with errors less than 1%.

In Figure 4.19 the the normalized dose vs. depth curves referring to the same spectrum has been plotted for a subset of materials. All curves meet at 1.0 for $t = 0$, however only points from 1 g/cm^2 are shown, due to the high dose reduction achieved after only 1 g/cm^2 of shielding material.

Simulations have been run up to a shielding thickness of 10 g/cm^2, values for which almost all the solar protons have been shielded. This does not mean that an astronaut would be safe if such an event would happen, because the high energy part of the spectrum, still passing through tens of centimeter of water equivalent, can have the potential to be a threat to the crew's health, being its fluence massive. However, for the scope of this work, whose goal is to characterize shielding properties of materials, after some cm these differences are less noticeable. Therefore, dose reduction is given with respect to the unshielded dose and, for now, nothing is said about the total dose delivered to an astronaut during a solar particle event.

When SPEs are concerned, little differences are seen among different materials. As for GCRs, also for SPEs the averaged atomic weight of the considered targets is inversely proportional to their shielding capability. Considering liquid hydrogen and methane as unrealistic choices, the next interesting materials which could be used to shield a solar particle event are hydrides, followed by HDPE and water.

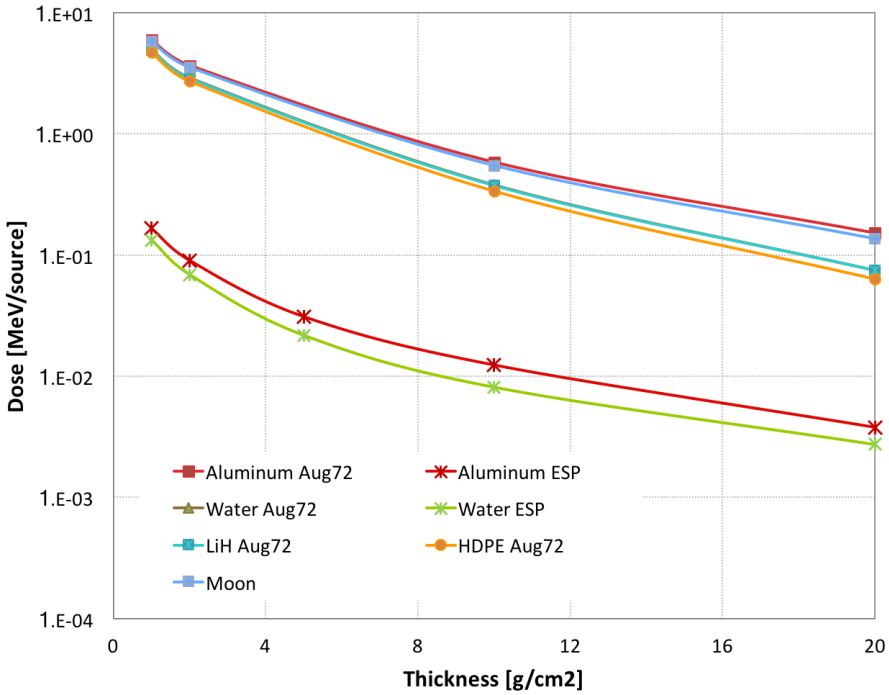

Fig. 4.20 SPE absorbed energy in water detector per single primary event for different materials: ESP model vs August '72 model for Aluminum and water, plus LiH, moon concrete and HDPE (August '72). Results obtained with PHITS simulations with errors less than 1%.

Figure 4.20 shows the calculated dose per primary event in the water detector for two different SPE spectra: ESP and August '72 SPE. It is possible to notice how, for lower shielded spacecraft or extra vehicular activities, an event similar to the August '72 one can potentially deliver higher doses to the crew than the one resulting from the ESP model.

Comparisons with Geant4

Comparison have been made between PHITS and GRAS/Geant4 simulations for GCR and SPE spectra with a subset of target materials and results are reported in Figures 4.21 and 4.22.

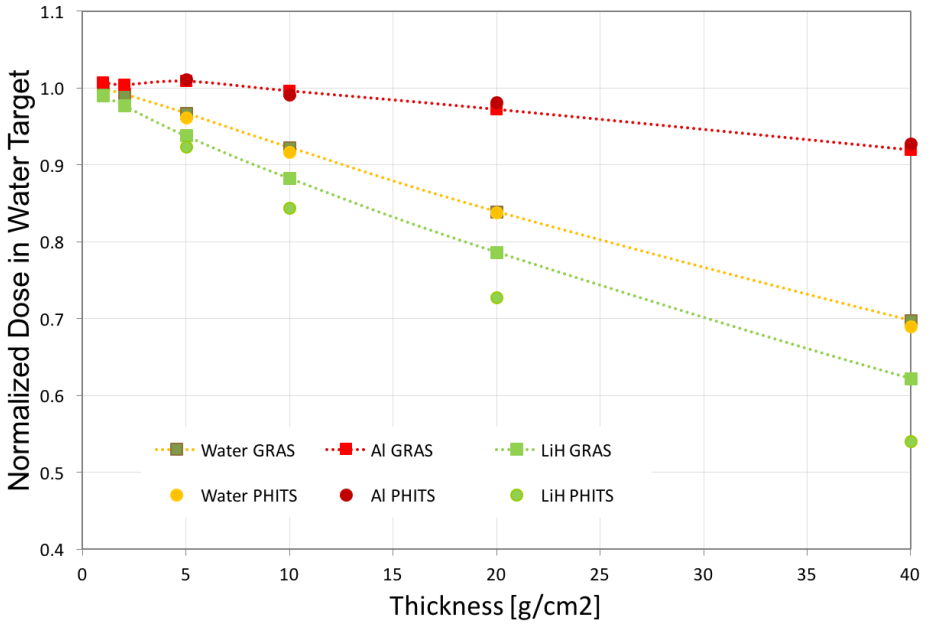

Fig. 4.21 Simulation of a GCR pencil beam on different shielding target material. Dose is calculated into a 10 cm radius, 2 cm thickness water detector with both PHITS and GRAS/Geant4 Monte Carlo codes. Results have errors less than 1% and therefore not shown in the graph.

The codes are in agreement within the simulation error but for GCRs interaction with LiH[2]. In this case, dose reduction results to be higher for PHITS than for Geant4.

[2]The comparison simulations have been done at the end of the simulations campaign when additional information were available on updated nuclear cross section models, implemented in PHITS, describing interaction with LiH. For this reason these Geant4 comparison simulations have been carried out with PHITS using the nuclear Kurotama cross-section formula, while the majority of

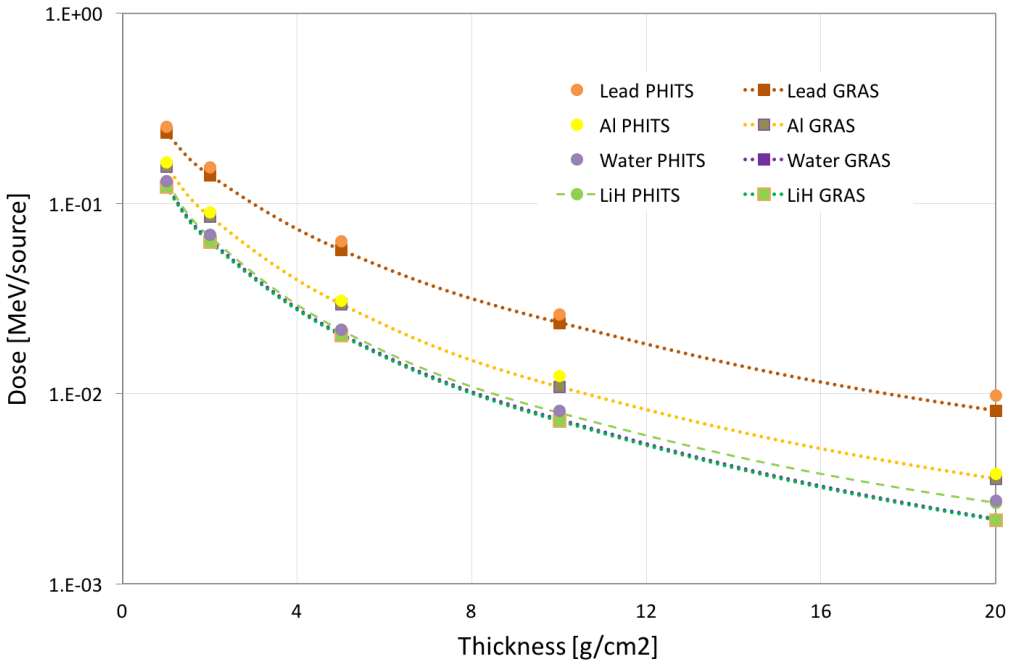

Fig. 4.22 Simulation of a SPE pencil beam on different shielding target material. Dose is calculated into a 10 cm radius, 2 cm thickness water detector with both PHITS and GRAS/Geant4 Monte Carlo codes. Results have errors less than 1% and therefore not shown in the graph.

This is due to the different nuclear cross-section models implemented in the two codes.

4.5 MDPS simulations

A typical spacecraft structure slab has been simulated to consider the different contribution to dose reduction of selected materials, when placed inside a habitat. In particular, considering the Columbus module of the ISS as reference, a primary structure principally made by the Micrometeoroids and Debris Protection System (MDPS) has been modeled. The following layers of materials have been considered: 0.25 cm of Aluminum, 0.55 cm of Nextel, 0.8 cm of Kevlar, 0.2 cm of Aluminum and 0.2 cm of HDPE. Shielding materials of varying thickness have then been inserted after the MDPS, i.e. after the first few centimeters of layered materials and before air (the green region numbered "1" in Figure 4.23). Dose and dose equivalent (ICRP60) have been calculated inside a 1 cm thick water detector, with a radius of 20 cm. Figure 4.23 shows the simulation layered setup as reproduced in PHITS simulations in the no target case.

A 1D pencil beam has been used, reproducing one of the worst case scenario SPE, August'72.

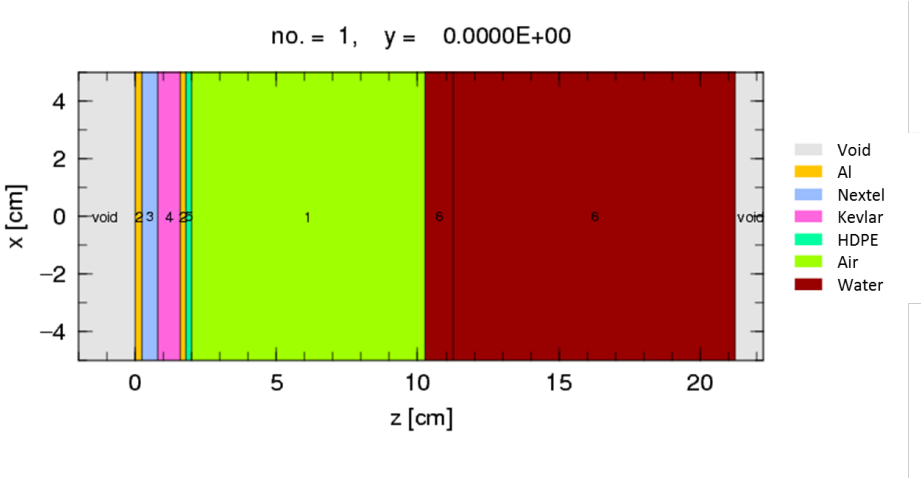

Fig. 4.23 Columbus MDPS as reproduced in the PHITS simulations.

the other simulations reported in this chapter are made with the default nuclear model implemented in PHITS. Refer to paragraph 5.6 for further information.

Results are finally reported for a layer of varying thickness of Aluminum, water and Kevlar in Figure 4.25.

After 20 g/cm^2 of additional shielding, the majority of the incoming radiation has been counteracted and no peculiar differences are present among materials when trying to shield solar protons. Dose reduction has been calculated as in the previous paragraphs. The same reduction trend is observed for ICRP60 dose equivalent (not reported here).

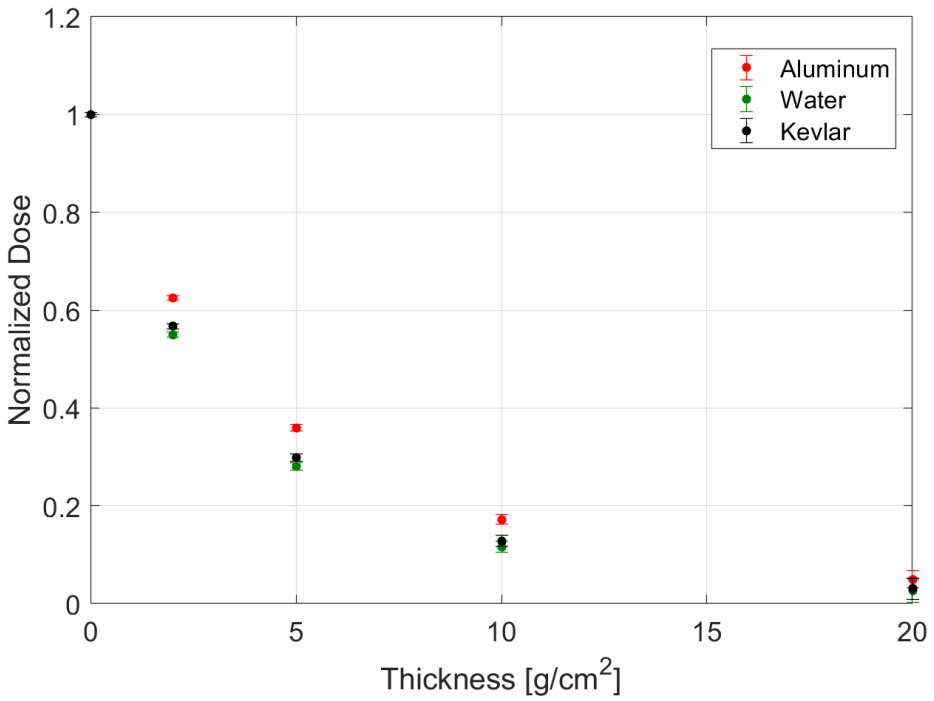

Fig. 4.24 Normalized dose (D_N) for a selected subset of shielding materials obtained with PHITS simulations.

4.6 Moon soil and shielding material simulations

Simulations to study the usefulness of adding extra shielding materials after a layer of moon soil have been carried out. These simulations have been used as starting point for the 3D moon habitat design, described in Chapter 6.

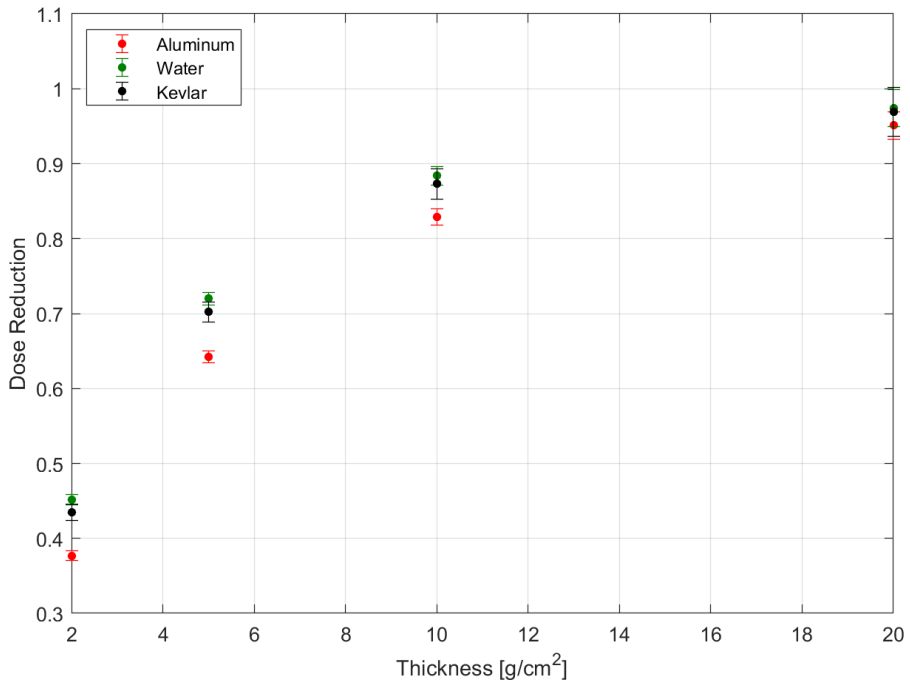

Fig. 4.25 Dose reduction (ΔD) for a selected subset of shielding materials obtained with PHITS simulations.

The set-up geometry is very similar to the one used for the trade-off simulations. An additional layer, made either of 45 or 90 g/cm^2 of moon soil, has been included between the GCRs source and the shielding material, as reported in Figure 4.26.

The composition assumed for the Lunar soil used in the Monte Carlo simulation is reported in Chapter 6 and its density is taken as 1.8 g/cm^3.

The GCRs source has been modeled as a circular beam of radius 40 cm to reproduce a more realistic exposure situation.

Six different shielding configurations have been simulated:

- Moon soil (25 cm - 45 g/cm^2) + Water
- Moon soil (25 cm - 45 g/cm^2) + LiH
- Moon soil (25 cm - 45 g/cm^2) + Moon soil
- Moon soil (50 cm - 90 g/cm^2) + Water
- Moon soil (50 cm - 90 g/cm^2) + LiH
- Moon soil (50 cm - 90 g/cm^2) + Moon soil

For each configuration, the additional shielding material layer thickness has been varied in a range from 10 to 50 g/cm^2.

The goal of this simulation is to understand the benefits, if any, of using additional shielding material after a layer of moon soil, in the hypothesis of a moon habitat shielded using in-situ materials. As a consequence, normalized dose has been calculated with respect to the dose in the configuration with only 90 g/cm^2 of moon soil D_{MS}, in the following way:

$$D_N = \frac{D_{MS+Sh}}{D_{MS}} \tag{4.4}$$

where D_{MS+Sh} refers to the dose in the detector after the Lunar soil and the shielding material.

Simulations have been done with PHITS, using the default nuclear models of the code.

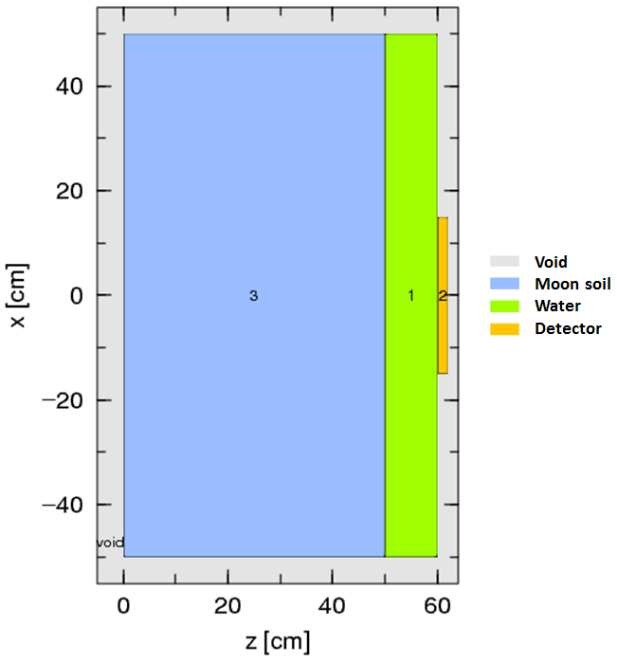

Fig. 4.26 Moon 1D simulations: set-up as obtained from PHITS simulation for the case of 90 g/cm^2 of Moon soil followed by 10 g/cm^2 of water.

Figures 4.27 and 4.28 report the results for the dose reduction obtained in the water detector (expressed in %) after varying thicknesses (in g/cm^2) of shielding materials.

Additional layers of Lunar soil lead to a dose increase up to about 45+50 g/cm^2, value after which the dose starts again to decrease.

When using water or lithium hydride, on the other hand, the dose is additionally decreasing with respect to the "only moon soil" situation, thanks to the fact that these materials have higher fragmentation cross sections and at the same time produce less neutrons than lunar soil.

Figure 4.29 and Figure 4.30 focus on the neutron and proton flux, respectively, behind different multilayered configurations. With respect to the scenario where only moon soil is considered, for LiH and water shielding configurations a drastic reduction of the number of neutrons reaching the water detector in the energy range important for biological effects was observed (0.01 MeV – 10 MeV). On the other hand, when adding additional Lunar soil, no improvement is observed.

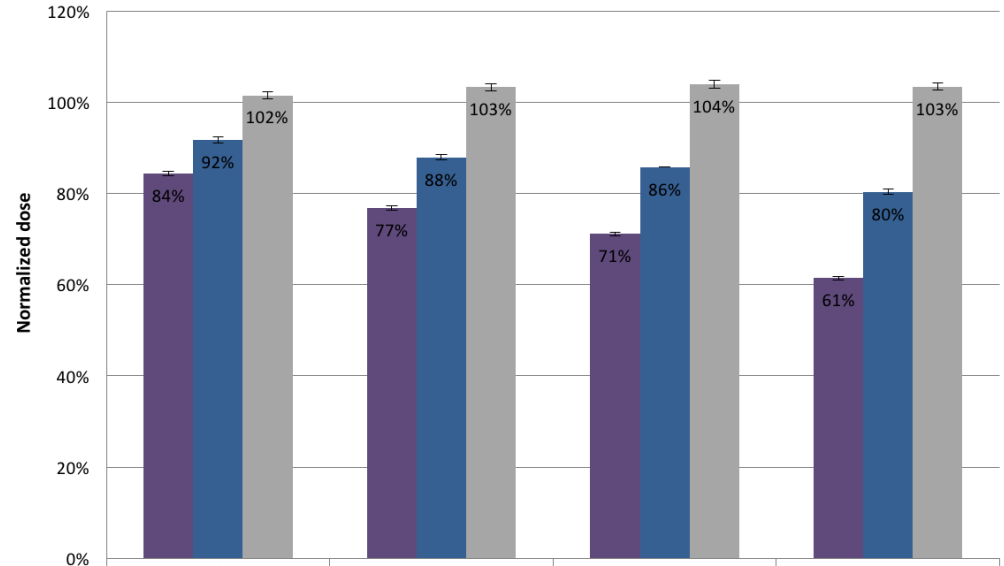

	10 g/cm2	20 g/cm2	30 g/cm2	50 g/cm2
LiH	84%	77%	71%	61%
Water	92%	88%	86%	80%
Moon Soil	102%	103%	104%	103%

Fig. 4.27 Normalized dose (Eq. 4.4) for a GCRs source in a water detector after 45 g/cm^2 of moon soil plus different thicknesses (g/cm^2) of different shielding materials, normalized to dose in the same detector after only 45 g/cm^2 of Moon Soil - PHITS simulations.

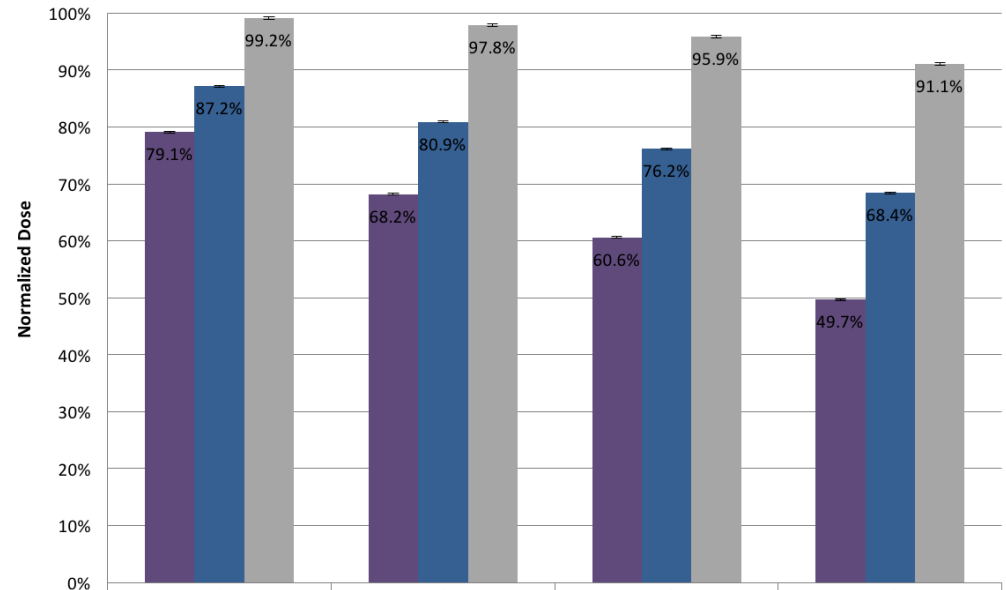

	10 g/cm2	20 g/cm2	30 g/cm2	50 g/cm2
LiH	79.1%	68.2%	60.6%	49.7%
Water	87.2%	80.9%	76.2%	68.4%
Moon Soil	99.2%	97.8%	95.9%	91.1%

Fig. 4.28 Normalized dose (Eq. 4.4) for a GCRs source in a water detector after 90 g/cm^2 of moon soil plus different thicknesses (g/cm^2) of different shielding materials, normalized to dose in the same detector after only 90 g/cm^2 of Moon Soil - PHITS simulations.

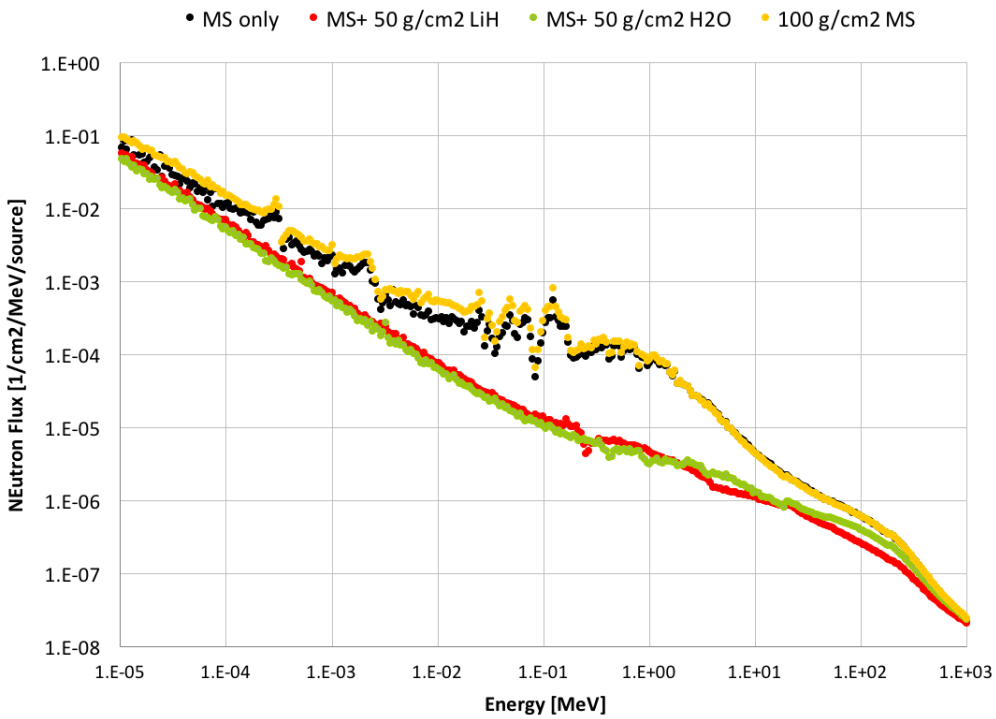

Fig. 4.29 Neutron fluence, normalized per the number of events and square cm, behind different moon soil configurations. Each configuration has 90 g/cm^2 of Moon Soil and 50 g/cm^2 of the shielding material - PHITS simulations.

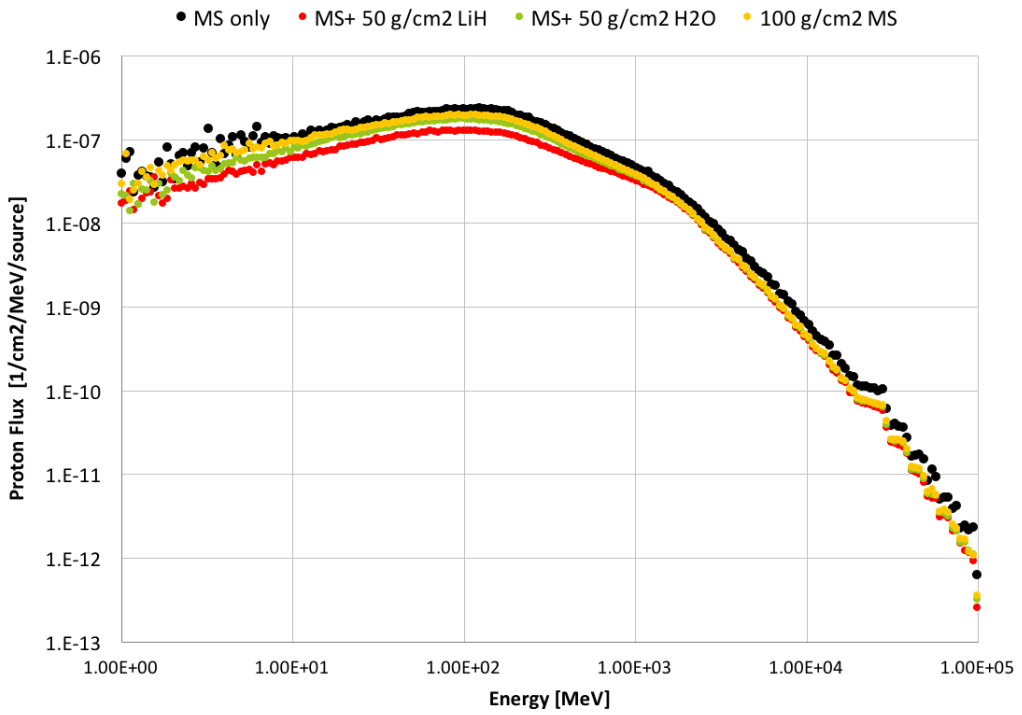

Fig. 4.30 Proton fluence, normalized per the number of events and square cm, behind different moon soil configurations. Each configuration has 90 g/cm^2 of Moon Soil and 50 g/cm^2 of the shielding material - PHITS simulations.

4.7 Conclusion on 1D simulations

Properly selecting radiation shielding materials and trying to optimize their arrangement outside and inside spacecraft, planetary habitat, suits and rovers are the only countermeasures available up to now for both GCRs and SPEs.

Simulations of radiation interactions with matter of different possible shielding materials and configurations have been performed to support the material selection process and also to produce guidelines for design.

Hydrides, and in particular LiH, represent the best option for shielding habitats from the point of view of the radiation shielding properties. This class of material is indeed the only simulated one able to guarantee an increased dose reduction compared to all the others.

Also, materials containing carbon, such as polymers and epoxies, are recommended to be studied as primary structure materials instead of Aluminum; in fact, their lighter nuclei have fewer neutrons to release and some nuclei can break into three helium nuclei without releasing any neutrons at all.

As regards ISRU materials, from simulations Moon and Mars simulants result to be better shielding materials than Aluminum.

On the basis of these results, the materials showing the most promising shielding properties were selected for the radiation tests described in Chapter 5 (the complete list is given in Chapter 3).

Chapter 5

Radiation test simulations

In the framework of ROSSINI2 experiment, several radiation tests have been carried out on single materials and multilayers configurations. At the same time, the radiation tests have been reproduced by means of both Geant4/GRAS[1] and PHITS simulations.

The comparison of the experimental results and the simulations outputs gives a validations of both the Monte Carlo codes in 2D configurations and under beams species and energies comparable with GCRs. PHITS version 2.80 and Geant4 version 4.10.01 have been used. Each simulation campaign has been preceded by parameters and physics lists optimization.

As regards Geant4, the QBBC-EMY Geant4 physics list has been selected. This physics list has been created for high energy hadronic physics and, in particular, for space applications, radiation biology and radiation protection.

As regard PHITS, straggling has been used with the energy straggling option number 1 for charged particle and nucleus, with Coulomb diffusion by Lynch's formula based on the Moliere theory (Eq.(4) in [74]) and event generation mode version 2. Cut-off energies have been changed to 1E-10 MeV and 1E-3 for neutrons and photons, respectively. All the other parameters have not been modified from PHITS default, exception made for nuclear models, which have been changed when light nucleus-nucleus reactions were involved, as described in the following sections.

The following experiments have been simulated:

[1]Most of Geant4 simulations reported in this chapter were done by Dr. Luca Bocchini, Thales Alenia Space, in the framework of ROSSINI2, and are here reported for the validation of the code

- Dose reduction experiments, carried out at Heidelberg Ion-Beam Therapy Center (HIT) and Brookhaven National Laboratory (BNL), with different particle sources between December 2015 and July 2016.
- Primary beam attenuation, done at Gesellschaft für Schwerionenforschung (GSI), Darmstadt, in July 2016.
- Microdosimetry and Neutron measurements, carried out at Trento Institute for Fundamentals Physics Applications (TIFPA).
- Double differential neutrons production cross section experiments, done at BNL in June 2016.

Experimental errors were sometimes not available and, therefore, not reported in some graphs.

5.1 ROSSINI study simulations

After the trade-off simulations reported in the previous chapter, PHITS and Geant4 simulations have been carried out to reproduce the experimental data taken during the ROSSINI study, ended in 2012.

The set-up used to carry out the ROSSINI (2012) simulations is the "BNL dose reduction" set-up, described in paragraph 5.2.2, but using a lower primary iron beam energy of 963 MeV/nuc. Full Bragg curves were measured for HDPE, pure Aluminum, Moon concrete and JSC Mars and Moon regoliths, irradiated with a ^{56}Fe beam at 963 MeV/nuc.

PHITS simulations show good agreement with test results for Aluminum and HDPE. As regards tests on Moon and Mars regolith, discrepancies are found after some grams per square centimeters of the materials. These disagreements are probably due to inaccuracies in modeling the properties of the materials, such as dust density and porosity.

Geant4 shows some unsolved issue when reproducing high-energy iron beam interacting with HDPE, as reported in the previous chapter. In Figure 5.1 the fragmentation region is characterized by an underestimation of the dose, while the

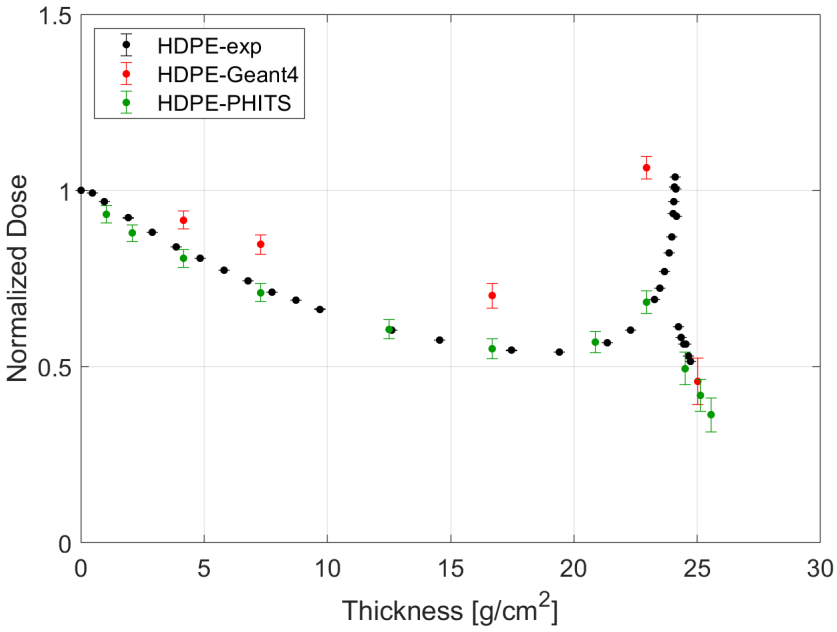

Fig. 5.1 Bragg curve of 963 MeV/nuc ^{56}Fe ions in HDPE as measured at BNL-NSRL and comparison with PHITS and Geant4 simulations results.

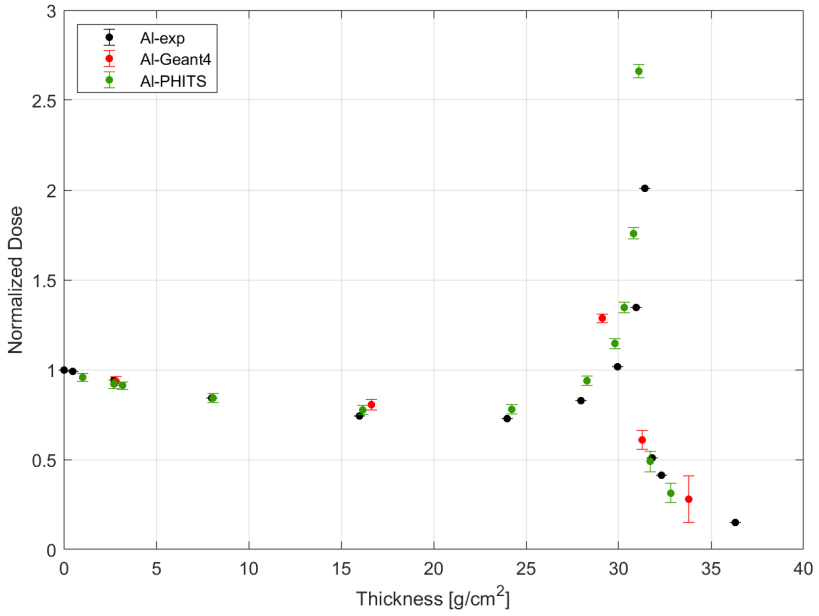

Fig. 5.2 Bragg curve of 963 MeV/nuc ^{56}Fe ions in Aluminum as measured at BNL-NSRL and comparison with PHITS and Geant4 simulations results.

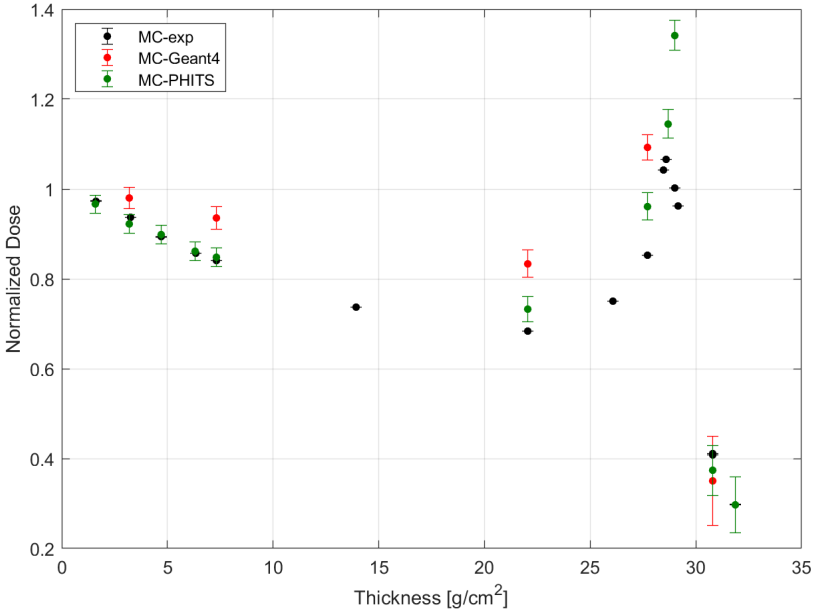

Fig. 5.3 Bragg curve of 963 MeV/nuc ^{56}Fe ions in Moon concrete simulant as measured at BNL-NSRL and comparison with PHITS and Geant4 simulations results.

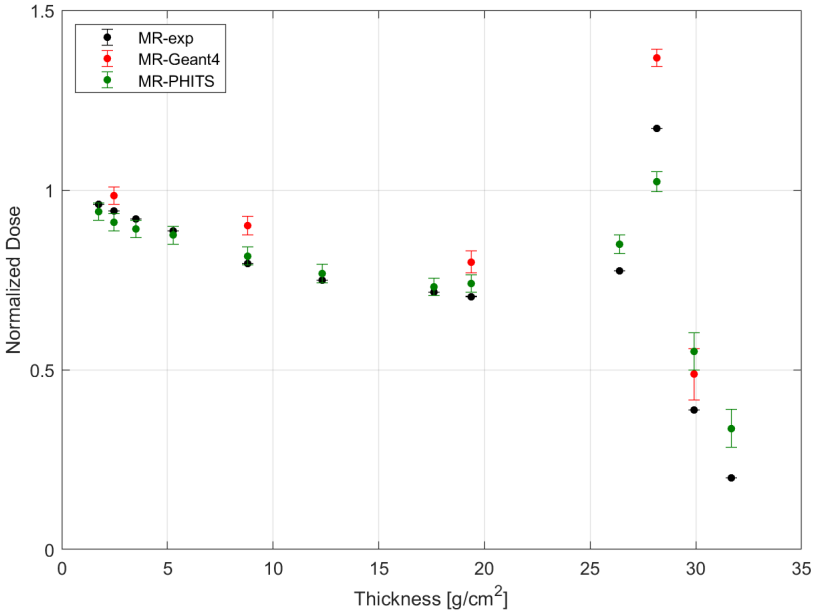

Fig. 5.4 Bragg curve of 963 MeV/nuc ^{56}Fe ions in Moon regolith simulant as measured at BNL-NSRL and comparison with PHITS and Geant4 simulations results.

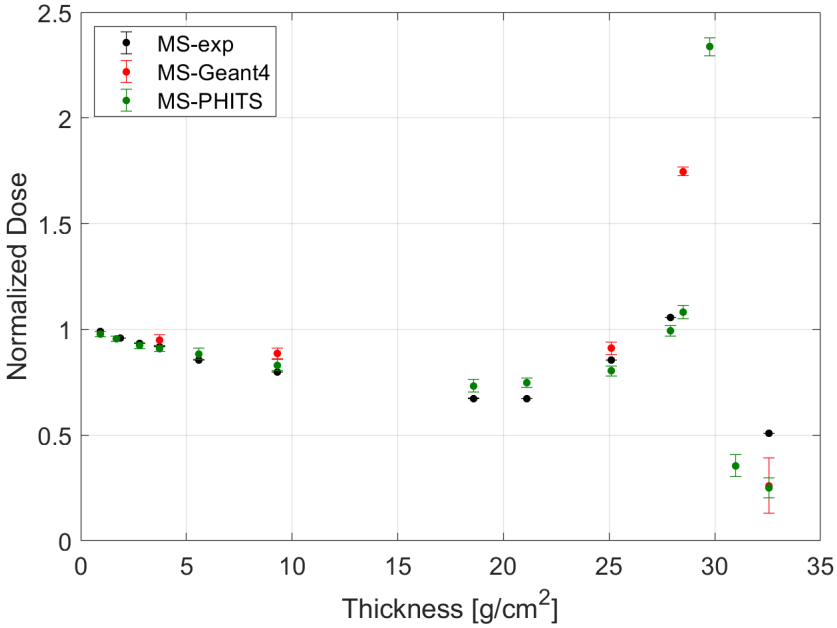

Fig. 5.5 Bragg curve of 963 MeV/nuc ^{56}Fe ions in Mars regolith simulant as measured at BNL-NSRL and comparison with PHITS and Geant4 simulations results.

dose behind the Bragg Peak seems to be better reproduced. The origin of these discrepancies is still under investigation.

5.2 Dose reduction radiation tests and simulations

5.2.1 Dose reduction experiments at HIT

Dose reduction experiments have been carried out at the HIT during two different beam shifts: the first one in December 2015 and the second one in March 2016.

HIT is a clinical facility where carbon and proton beams are available to treat patients. The synchrotron accelerator can deliver protons up to 230 MeV, Helium up to 230 MeV/nuc, Carbon up to 430 MeV/nuc and Oxygen up to 430 MeV/nuc.

430.1 MeV/nuc Carbon ions pencil beam has been used in ROSSINI2 to test the dose reduction effectiveness of different single and multilayers material configurations.

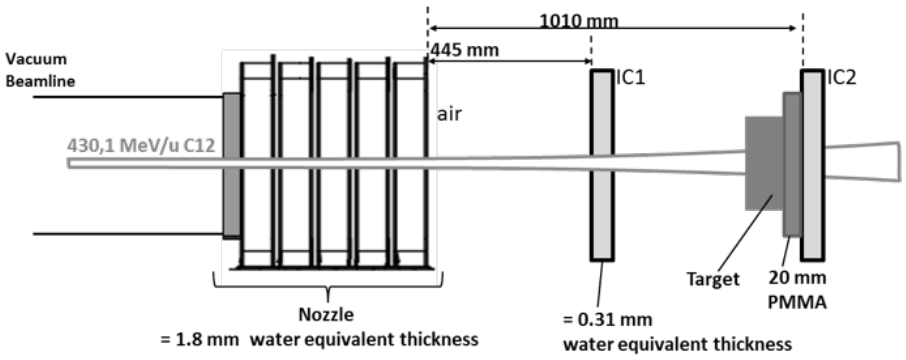

Fig. 5.6 Schematic drawing of the experimental setup used for the ROSSINI2 dose attenuation measurements at HIT, used for PHITS and Geant4 simulations (GSI courtesy - not in scale).

The schematic drawing of the experimental setup can be found in Figure 5.6. Two large parallel plate Ionization Chamber (IC) with a lateral size of 20 cm and an active gas gap of 10 mm, IC1 and IC2, were used before and after the targets, respectively. Both IC were filled with air.

In the test configuration a 2 cm thick Poly(methyl methacrylate) (PMMA) slab was placed just upstream of IC2 to compensate the electrons build-up effect: in this way constant conditions in the IC2 concerning electron and fragment build-up were established. The target was then positioned in front of the PMMA layer, in contact with it. The no-target measurement included the PMMA layer.

In the simulations, all the in-beam components were reproduced with a varying degree of simplification. The ionization chambers have been modeled as boxes with the same dimensions as in reality, with air inside, between Mylar layers. The air volumes have been divided into active and non-active volumes, considering that only the gas between the electrodes (electrodes were not modeled) is contributing to the dose measurements. The total gas volume thickness of each IC is 4 cm and the Mylar layer thickness is 0.0025 cm. The nozzle was modeled as a box of water 0.18 cm thick. PMMA was reproduced as in the reality, as a 20x20 cm box thick 2 cm. Finally, all the volumes in the simulations were surrounded by air in standard conditions and the beam room structures were neglected.

Detailed geometrical models have been used also for the targets. In Figure 5.7 and Figure 5.8 sketches of the model with single and multiple LiH targets are shown, respectively. In our simulation of LiH samples also the PE plastic surrounding the

samples has been modeled (with two PE layers of 0.018 g/cm^2 each), to consider its contribution to the dose reduction.

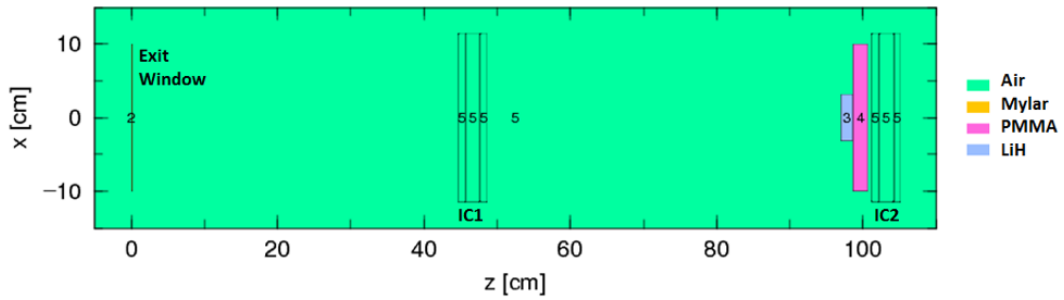

Fig. 5.7 Dose reduction experiments at HIT - Simulation set-up with a single LiH sample as modeled in PHITS. It is possible to see the exit window, the ICs and PMMA slab too. Air is surrounding the geometrical bodies.

In the PHITS simulations the source is modeled as a mono-energetic (430.1 MeV/nuc) axial source of ^{12}C ions with a radius of 1 cm. Radiation doses were registered in both ionization chambers active gas volumes.

An initial simulation has been made with PHITS and Geant4 reproducing experimental data of a PMMA Bragg peak curve, measured in the past at HIT, to benchmark the codes using experimental data obtained with the same beam energy and setup of the ROSSINI2 dose reduction tests.

Results of the comparison between experimental data and the simulations for the PMMA Bragg peak are reported in Figure 5.9 for the 430.1 MeV/nuc Carbon ions. The simulations relative error is less than 1%. The agreement between the simulations and the experimental data is quite good, in particular for aeric densities up to Bragg peak. The normalized dose values obtained by simulations slightly deviate from the experimental values after the Bragg peak, on the tail caused by nuclear fragmentation.

In the measurement and in the simulations similarly, the ratio of the signal (absorbed energy) of the two ionisation chambers has been calculated as:

$$r = \frac{D_{IC2}}{D_{IC1}} \tag{5.1}$$

In the measurement and in the simulations as well, the ratio of the signal (absorbed energy) of the two ionisation chambers with and without the target has been used to

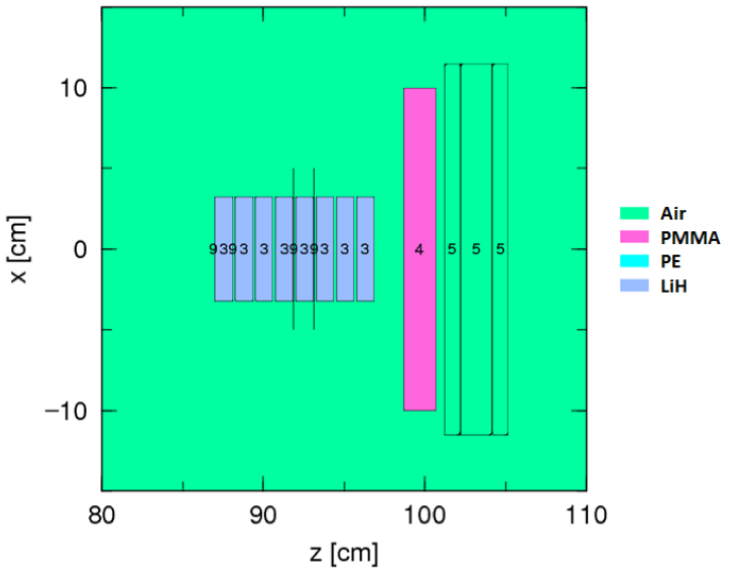

Fig. 5.8 Dose reduction experiments at HIT - Simulation set-up with multiple LiH samples: focusing on a single LiH sample as modeled in PHITS, it is possible to see only two of the plastic layers surrounding the LiH samples, because of low refinement of the selected graphical resolution.

define a reduction factor, R:

$$R = \frac{r_{targ}}{r_{no\ targ}} \tag{5.2}$$

defined as the signal ratio with the target divided by the signal ratio without the target. Finally, the relative dose attenuation produced by the target is given by:

$$\delta D = 1 - R \tag{5.3}$$

To be able to compare shielding effectiveness of materials of different thicknesses, a dose reduction per Aeric Density (A_D) [g/cm^2] has been finally defined for each measurement point as:

$$\delta D_n = \frac{\delta D}{A_D} \tag{5.4}$$

This last quantity will vary with the thickness of the material, therefore, when more than one measurement point is available per material, an average dose reduction has sometimes been introduced.

For each simulation, moreover, information on the particle fluences at different volume interfaces, energy deposits and interactions were saved and are available

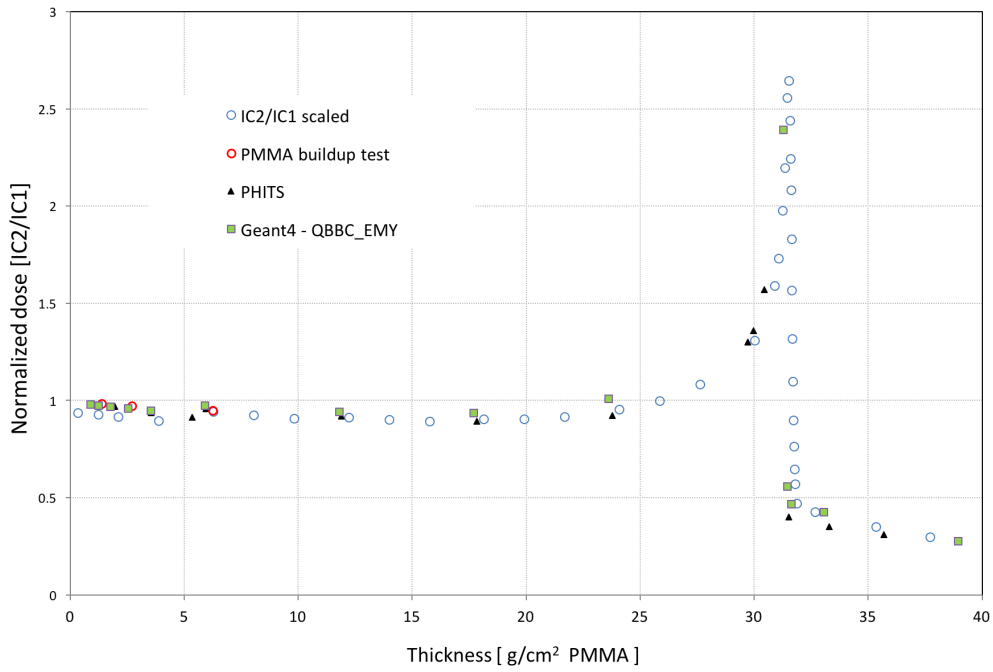

Fig. 5.9 Dose reduction experiments at HIT - Bragg peak in PMMA irradiated with ^{12}C ions at 430 MeV/nuc - Experimental data courtesy of HIT and simulations results obtained with PHITS and Geant4.

for future works. Particles fluxes [1/(cm^2*source)] inside the simulated volumes, separated for each of the main particle species, are hereafter shown in Figure 5.10, as obtained in a PHITS simulation of a Carbon beam interacting with a target (number 3 in the picture).

It is possible to see that the primary beam is slightly spreading as crossing the material present on its way. Secondary alpha particles and protons are generally generated with a forward peak, as a results of nuclear interactions.

Experimental measurements, in terms of reduction factors and their relative simulations results are reported, together with information on the errors, in Figure 5.11.

Relative dose attenuation produced by the target (experimental data) is given in Figure 5.12 and it gives practical values for the evaluation of the materials.

The dose reduction values at the HIT experiment show very large relative differences for the different materials (much stronger than for GeV/nuc beams, as can be seen in the following paragraphs), because the increasing in dE/dx reduces the effectiveness of the materials, therefore increasing the relative differences.

Dose attenuation with an aluminium target is close to zero for small thickness and anyway very low for thick slabs. This is due to the fact that for 430.1 MeV/nuc Carbon ions, the aluminum attenuation is nearly compensated by the increase of dE/dx.

LiH turns out to be the best shielding material among the selected ones, and the only one providing a good dose reduction, when compared to all the others. Polymers and water present similar dose reduction, while no difference is noticeable between epoxies with and without nanotubes (NT), as expected, considering the low mass percentage of NT used. ANMAC materials also have similar dose reductions whether made with magnetized or non-magnetized nano-particles, apparently meaning that the magnetization of the nano-particles inserted in the ANMAC HDPE is not able to modify the interactions of high energy beams with materials.

Generally, agreement is good for both Monte Carlo codes. However, dose attenuation of LiH predicted by the default models implemented in PHITS shows a strong overestimation of the LiH ability to reduce the dose, due to the nuclear cross section model used by the code. Some analyses have been done to investigate the disagreement and different nuclear cross section models have been employed

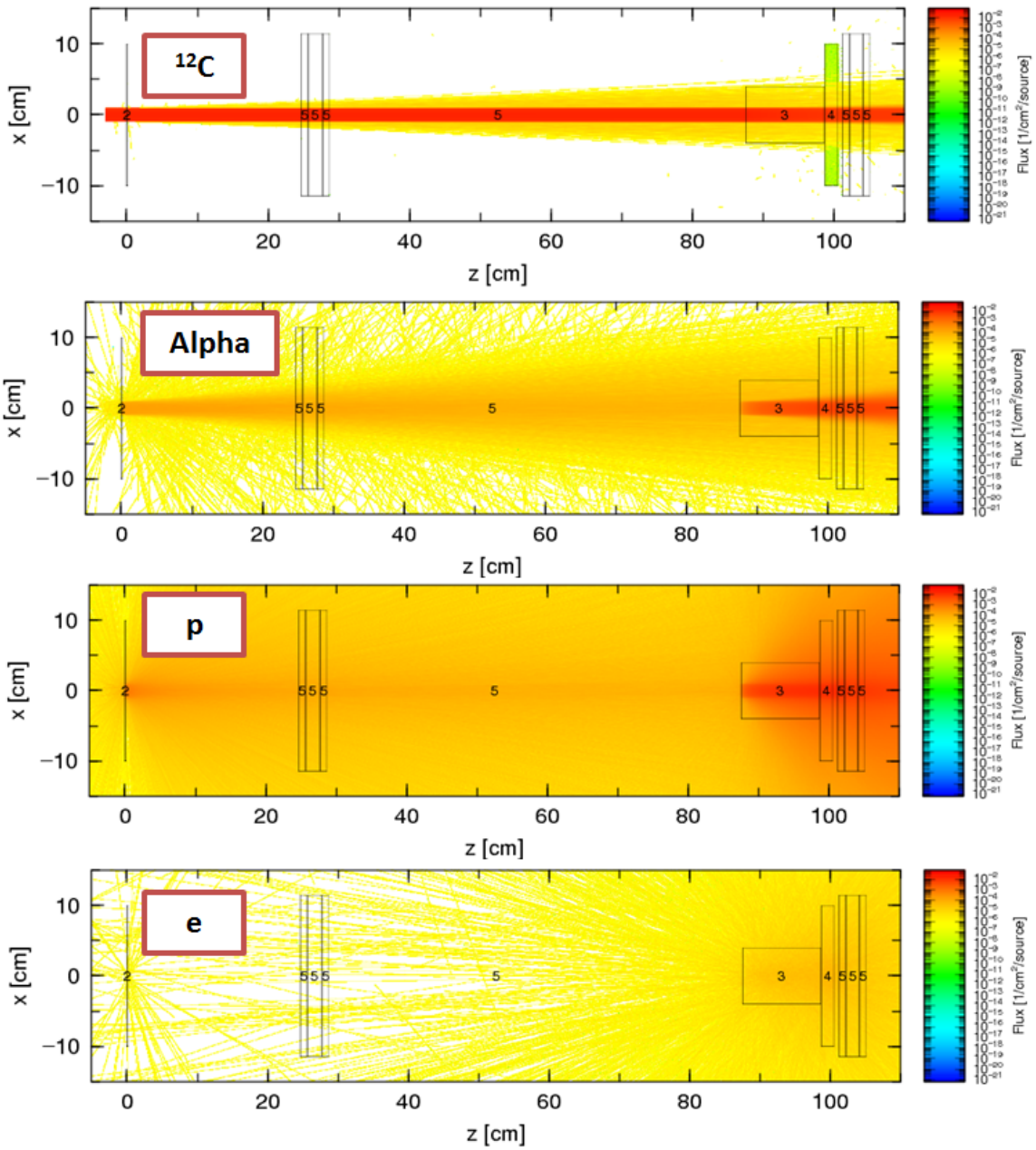

Fig. 5.10 Particles normalized fluxes [1/(cm^2*source)] inside the simulated volume, separated for each of the main particle species, generated by a ^{12}C beam on a target - Dose reduction experiments at HIT - PHITS simulation.

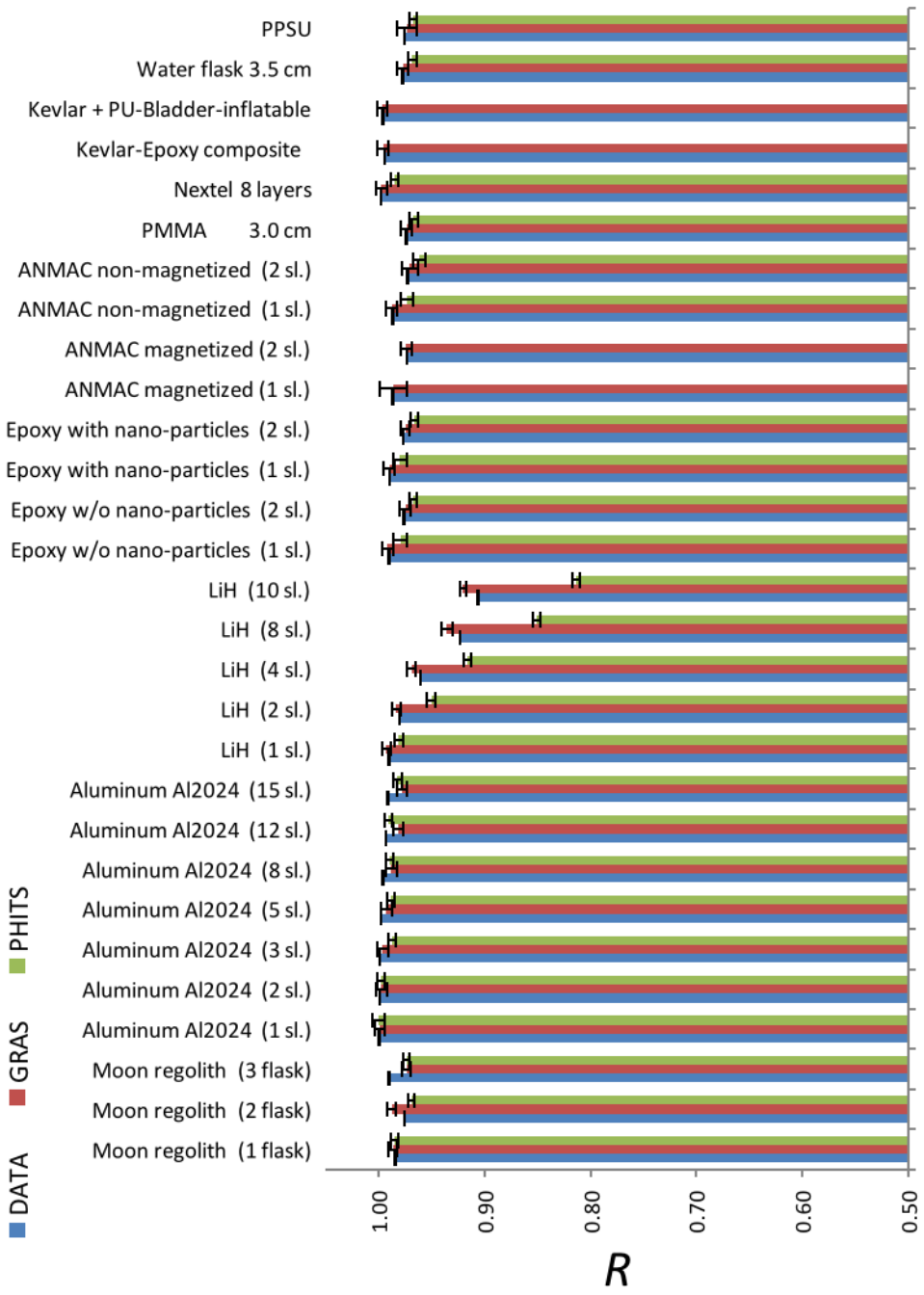

Fig. 5.11 Dose reduction experiments at HIT - Reduction factors for the tested targets: experimental results, PHITS and Geant4/GRAS simulations outputs.

in additional simulations. A dedicated paragraph is written on the subject (refer to paragraph 5.6).

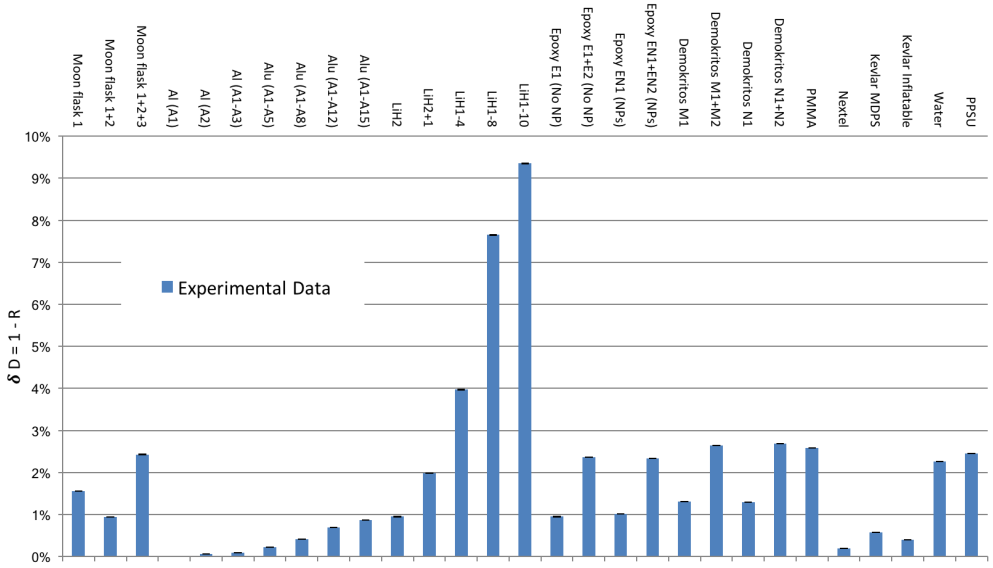

Fig. 5.12 Dose reduction experiments at HIT - Percent dose attenuation, experimental data.

5.2.2 Dose reduction experiments at BNL-NSRL

The NSRL is an accelerator-based center able to provide charged particles for space radiation research, located in Upton, NY. The facility is funded by NASA and managed in collaboration with BNL. Nowadays ion species from protons to gold are available, at energies ranging from 50 MeV/nuc to 2500 MeV for protons and 1500 MeV/nuc for ^{56}Fe. It is also possible to achieve lower energies using passive absorbers. The beam line is able to produce a large square beam spot with a uniform radiation field over a 20x20 cm^2 square, useful when radio-biology experiments are performed.

The shielding effectiveness of some of the ROSSINI2 materials has been assessed by measuring their performance in reducing the dose when exposed to a 20x20 cm^2 1000 MeV/nuc Helium beam and/or 972 MeV/nuc Iron beam.

Figure 5.13 reports a schematic draw of the dose reduction set-up used at NSRL for ROSSINI2.

Referring to Figure 5.13, the dose behind the target was measured with an ionization chamber (EGG counter) produced by Far West Technology (model IC-17A), placed as close as possible (less than 1 cm distance) to the target. Another ion chamber, QC3, placed upstream the target material, monitored the incoming

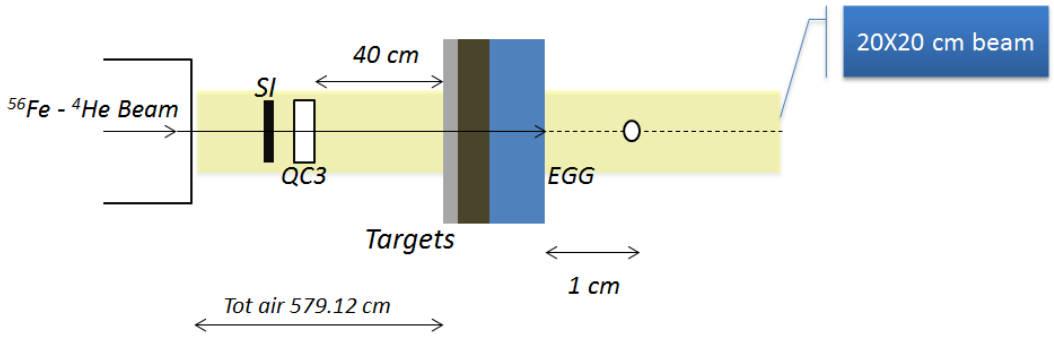

Fig. 5.13 Dose reduction experiments at BNL NSRL - Experimental set-up for ROSSINI2 study (not in scale).

beam, providing the normalization factor from which the dose reduction could be calculated. S1 is instead a scintillator, also used to monitor the beam.

The analysis of the measured dose values is performed in the same way as in Paragraph 5.2.1. As for the measurements carried out at HIT, dose attenuation due to the experimental setup itself was assessed by a no-target measurement and the reduction factor R was calculated with respect to this no-target measurement (that, in this case, corresponds to the ratio between the measured dose in EGG and the one in QC3, without the target).

Simulations using PHITS and GRAS/Geant4 of the dose reduction experiment performed at NSRL have been made. A 20x20 cm^2 mono-energetic (1 GeV/nuc ^{4}He and 972 MeV/nuc ^{56}Fe) beam has been modeled perpendicularly reaching the targets and the dose behind the shielding has been calculated inside the sensitive volume of the EGG chamber. Air has been included everywhere in the beam room.

The aluminum vacuum window was modeled as a slab of thickness 0.103 mm, scintillator S1 as 2 mm of polyviniltuolene, the QC3 ion chamber as a slab of 0.068 mm of water equivalent (40x40 cm^2 size). Finally, the EGG was reproduced as a sphere made of A-150 tissue-equivalent plastic, with diameter of 1.25 cm and wall thickness of 0.127 cm.

Figure 5.14 reports a sketch of the final PHITS dose reduction geometrical model.

One has to note at this point, that this set-up is slightly different from the one at HIT. At NSRL a large beam is used and dose is calculated inside a small detector, while the opposite happens at HIT, where a pencil beam is employed and wide ionization chambers were used as detectors. The reason of this differences is mainly

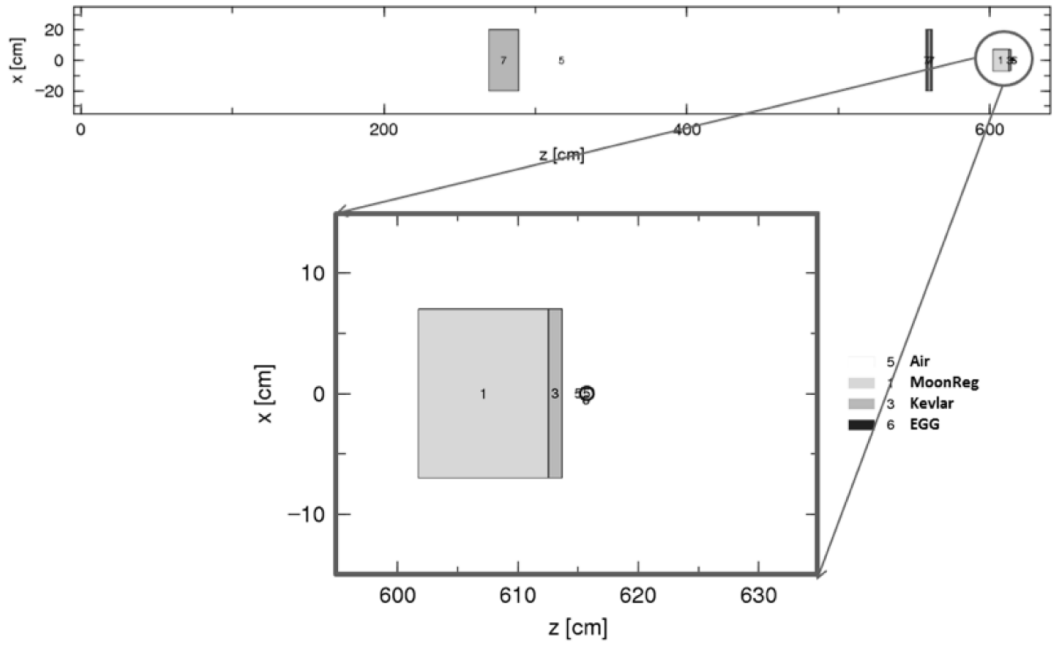

Fig. 5.14 Dose reduction experiments at BNL NSRL - Dose reduction set-up as reproduced in PHITS; in the zoomed part it is possible to see the multilayer target (1+3) and the EGG chamber section.

due to the fact that HIT is a treatment facility, while NSRL was expressly created by NASA to reproduce a space radiation exposure. Furthermore, the beam energies are also different in terms of consequences on dose reduction. For 430 MeV/nuc carbon ions, it is possible to notice from Figure 5.9 that fragmentation is slightly balanced by dE/dx, leading to a lower dose reduction compared to the situation at NSRL, where higher energy beam are employed and fragmentation of the primary beam dominates over the increase of the stopping power.

Different single layers and multilayers configurations have been studied at NSRL. Properties of the investigated multilayers are reported in Table 5.1. Multilayer A is representative of a rigid primary structure made of carbon fibers to hold the pressurized volumes and combinations of aluminum, Nextel and Kevlar to protect them from meteoroids and thermal excursions. It has the following configuration: 0.57 g cm^{-2} Al 2024, 0.7 g cm^{-2} Kevlar resin, 0.4 g cm^{-2} Nextel and 0.3 g cm^{-2} carbon fibers. Multilayer B, on the other hand, is a reproduction of an inflatable portion of a future habitat, where Nextel and Kevlar protect the inflatable Bladder made of PFTF and PU. Multilayer B has the following configuration: 1.2 g cm^{-2} Nextel and 0.028 g cm^{-2} Inflatable Kevlar + inflatable Bladder.

Multilayer configuration	g cm^{-2}	Test Numbering
Multilayer A	1.97	28
Multilayer A and LiH	8.10	24
Multilayer A and water	6.97	25
Multilayer B and LiH	7.37	30
Multilayer B and water	6.23	29
Moon regolith and Multilayer B	22.28	34
Moon regolith, Multilayer B and LiH	28.42	36
Moon regolith, Multilayer B and water	27.28	35

Table 5.1 Multilayer configurations studied at NSRL and relative thicknesses in g cm^{-2}. Also, alternative numbering used during the test and sometimes reported in this work are given.

Figures 5.15 and 5.16 report the relative dose attenuation (in percentage) measured at NRSL for Helium and Iron beams, for single materials and multilayers, respectively. Dose attenuation are given in percentages and are calculated as in Equation 5.3.

E and EN refers to epoxies with and without nanotubes inside them, respectively. M and N to magnetized and non-magnetized ANMAC samples.

Figures 5.17 and 5.18 show the reduction R (Equation 5.2) of the experimental measurements compared with PHITS and Geant4 simulations results, for Helium and Iron beams, respectively.

As regards the simulations, also in this case it is possible to state that the agreement with experimental data is in general good for both Geant4 and PHITS. PHITS, however, when simulations are run with default nuclear cross section models, presents again an overestimation of the shielding effects for LiH, as seen in the previous paragraphs.

Finally, Figures 5.19 and 5.20 report the normalized dose reduction per aeric thickness (δD_n Equation 5.4) as function of depth for several target types irradiated with 972 MeV/nuc ^{56}Fe and 1 GeV/nuc ^{4}He ions, respectively.

The following considerations can be drawn from the results obtained with the 972 MeV/u ^{56}Fe beam. The most effective shielding material per g cm^{-2} is again Lithium Hydride, performing even better than HDPE: its average normalized dose reduction per aeric density is about 6% versus about 4 % g^{-1}cm^2 of HDPE (Figure 5.19). Results obtained with Moon regolith indicate that this ISRU simulant is

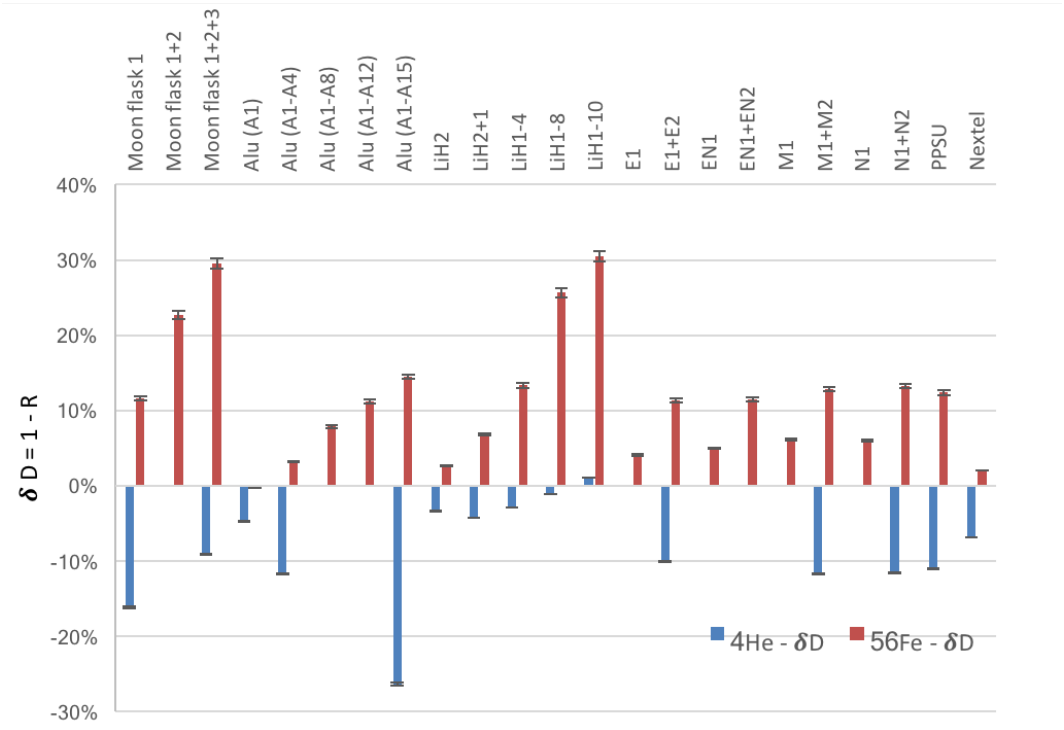

Fig. 5.15 Dose reduction experiments at BNL NSRL - Percent dose attenuation for single materials (experimental data).

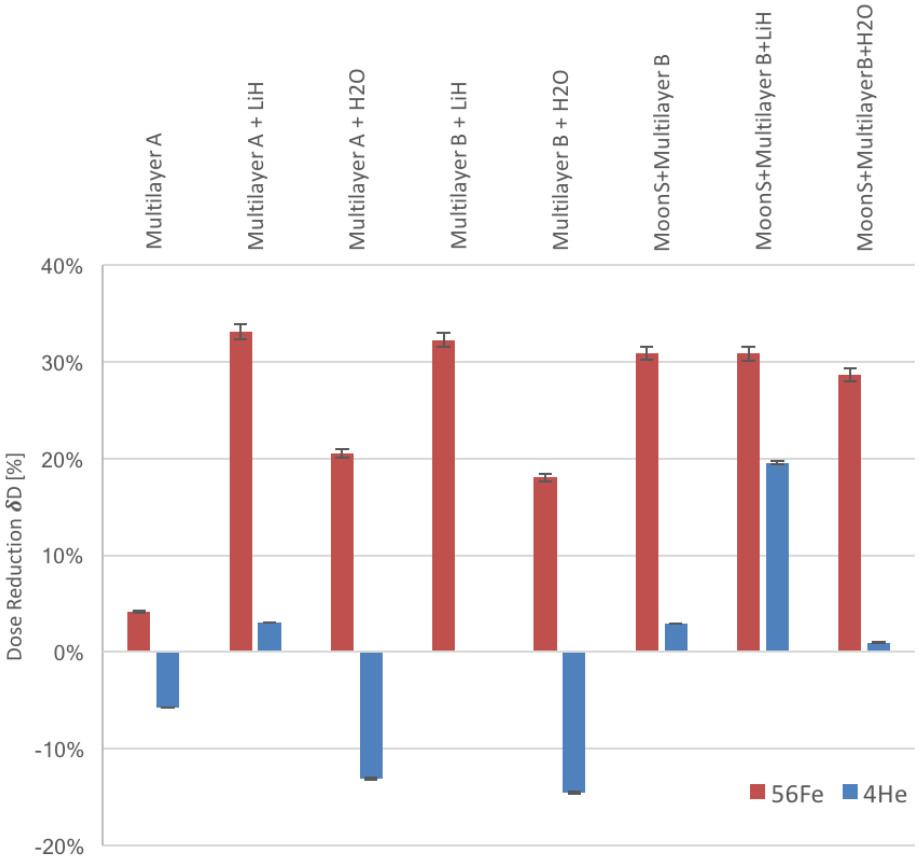

Fig. 5.16 Dose reduction experiments at BNL NSRL - Percent relative dose attenuation for multilayer configurations, experimental data.

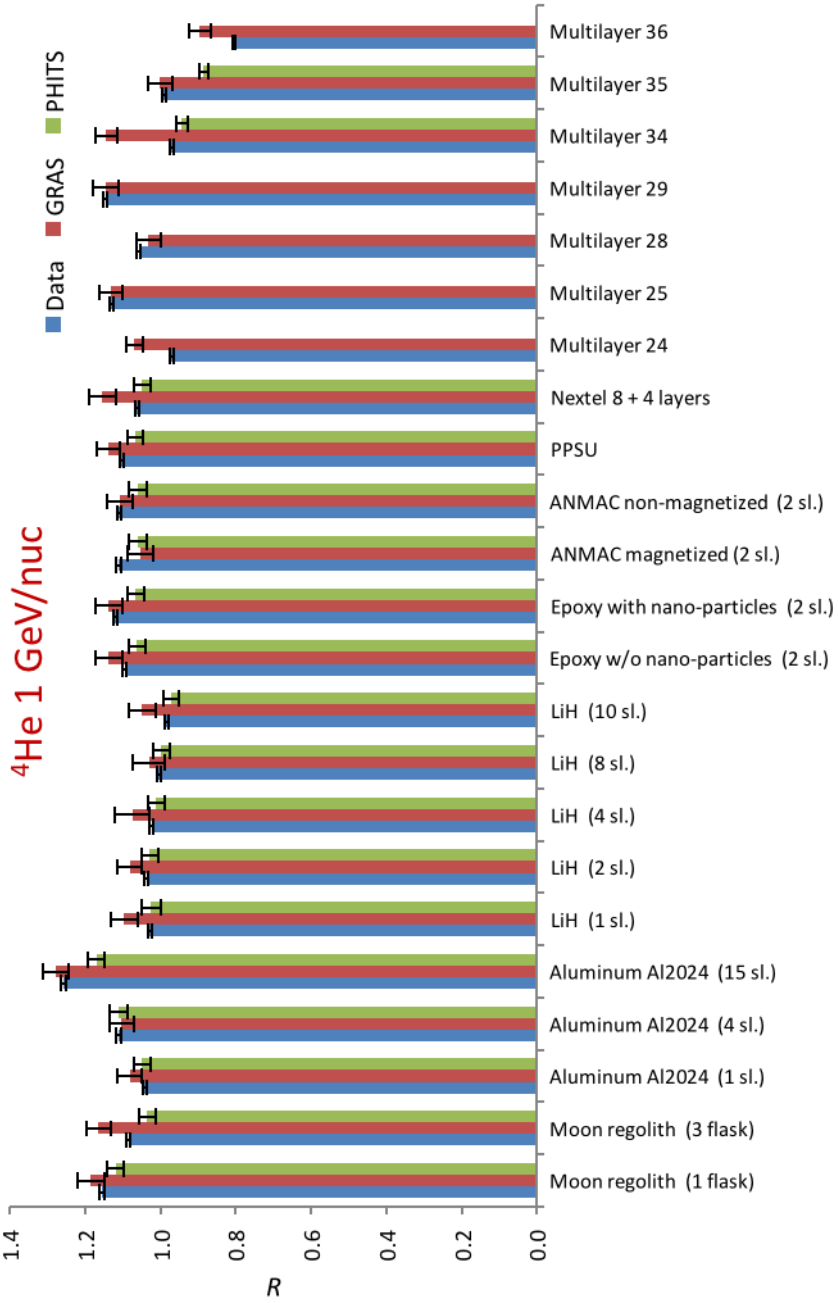

Fig. 5.17 Dose reduction experiments at BNL NSRL - Reduction factor obtained with several targets under 1 GeV/nuc helium beam (experimental results, PHITS and Geant4/GRAS simulations outputs).

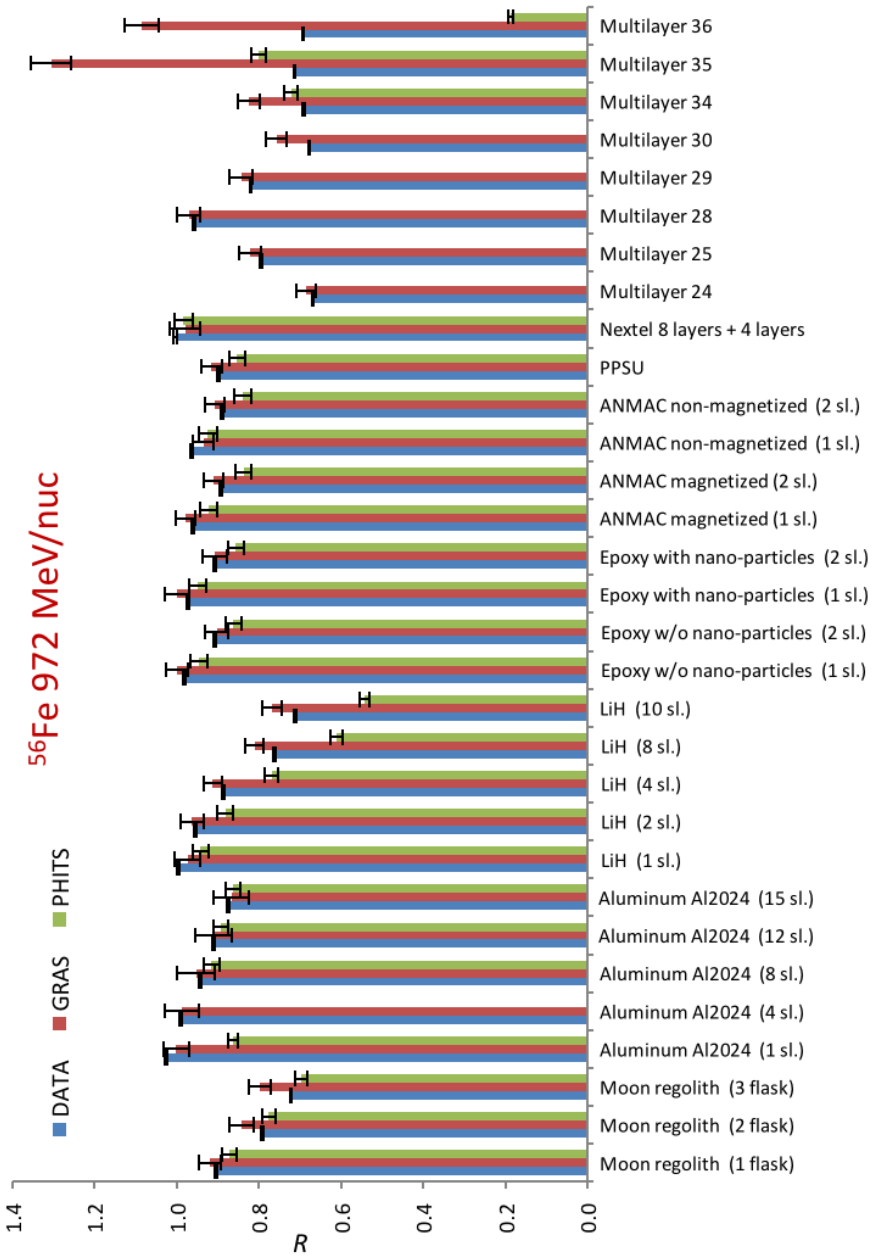

Fig. 5.18 Dose reduction experiments at BNL NSRL - Reduction factor obtained with several targets under 972 MeV/nuc iron beam (experimental results, PHITS and Geant4/GRAS simulations outputs).

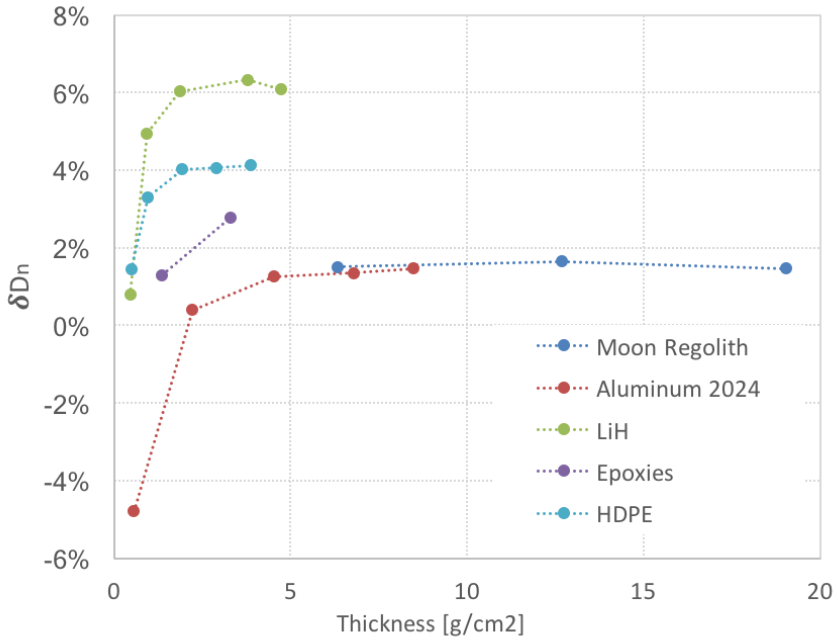

Fig. 5.19 Dose reduction experiments at BNL NSRL - Normalized dose reduction as a function of depth for several target types irradiated with 972 MeV/nuc ^{56}Fe ions.

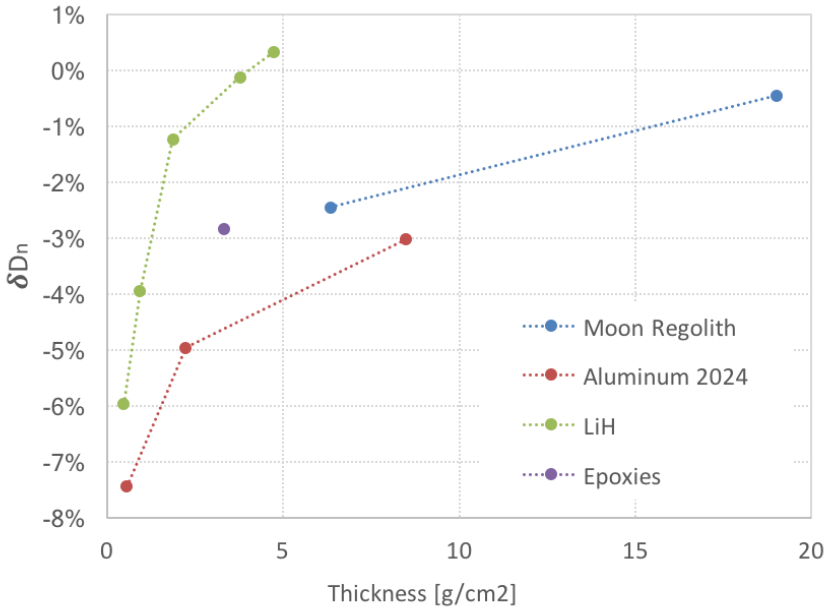

Fig. 5.20 Dose reduction experiments at BNL NSRL - Normalized dose reduction as a function of depth for several target types irradiated with 1 GeV/nuc ^{4}He ions.

characterized by a similar dose reduction effectiveness of aluminum, around 2% $g^{-1}cm^2$.

Furthermore, aluminium 2024 appears to be a worse shielding material than the standard aluminium according to the results of the previous ROSSINI study, reported in the ROSSINI final report, available online on the ESA website (reference: SGI-TASI-PRO-0226).

The presence of nanotubes in the epoxy samples does not appear to enhance their shielding capability, as for the HIT measurements results.

The multilayer representative of a rigid habitat (multilayer A) provides approximately a 4% dose reduction (Figure 5.16) when exposed to a high energy iron beam. This value is increased up to 35% by adding 6 g cm^{-2} LiH behind it, but only up to 25% with a 5 g cm^{-2} water target. The same trend is observed for multilayer B.

When 12 g cm^{-2} of Moon regolith is placed in front of the multilayer B, it dominates the dose attenuation and a further addition of LiH or water does not result in any significant change.

We can notice that the multilayer configurations of Moon regolith followed by either LiH and water have aeric thicknesses close to the position of the Bragg peak for irradiation with 963 MeV/nuc ^{56}Fe in Moon regolith, as shown in Figure 5.4. This is probably the reason why the simulations, characterized by uncertainties in set-up reproduction, are not in agreement with the experimental data in Figure 5.18: around the Bragg Peak location, dE/dx is highly varying with thickness.

The plot of the normalized dose reduction versus target depth (Figure 5.19) shows a similar trend for all materials. For small thicknesses, δD_n increases rapidly until it reaches a peak (whose position and width heavily depends on the material) and then it starts decreasing. The cause of such small values observed for very thin shields (below 1 g cm^{-2}) is probably due to the production of delta rays and secondary target fragments, but its nature should be investigated and clarified with the help of the Monte Carlo simulations.

Instead, as regards the Helium beam irradiation tests, Figure 5.20 reports the normalized dose reduction as function of depth for several target types irradiated with 1 GeV/nuc ^{4}He ions. None of the irradiated targets was thick enough to attenuate the beam. Unlike for ^{56}Fe ions, the materials tested against high energy alpha particles show different shielding behaviors. LiH starts showing some shielding effectiveness

already at 6 g cm^{-2} while the dose behind Aluminum 2024 is still increasing rather than decreasing up to 10 g cm^{-2} depth. Moon regolith also appears to be a poor shielding materials against ^{4}He ions, causing a negative δD_n even after 20 g cm^{-2} of thickness.

In summary, the experimental campaign performed at NSRL suggests that a candidate shielding material suitable for GCRs should be tested with at least two beams with different characteristics as those selected in this study. The results reported above indicate that some materials with good shielding effectiveness against 972 MeV/nuc ^{56}Fe ions perform very poorly when irradiated with high energetic alphas.

Among the material types included in this investigation, Lithium Hydride represents the best option for in-flight habitats, when only radiation shielding properties are considered.

5.3 Primary beam attenuation measurements and simulations at GSI

The measurement campaign for the total charge-changing cross sections in the framework of ROSSINI 2 took place in the experimental room “Cave A” at the GSI Helmholtzzentrum GmbH in Darmstadt.

GSI performs basic and applied research in physics and other science disciplines, such as plasma physics, atomic and nuclear physics, biophysics and medical research. All particle species from protons to uranium can be accelerated at GSI up to at least 1 GeV/nuc of energy.

The objective of this campaign was to measure the loss of primary carbon (total charge changing cross section, looking only at the loss of Z=6 particles). To do so, the primary beam attenuation was measured using a 600 MeV/nuc ^{12}C beam with a Full Width at Half Maximum (FWHM) of about 5 mm on the target. Three kinds of targets were irradiated with different thicknesses: LiH, Moon concrete and Polyethylene.

The beam, once passed through the vacuum exit window made of 0.01 cm of Al, was monitored by a BC400-like plastic scintillator, named START detector.

A 23 cm long hexagonal ΔE/E telescope with an inscribed radius of 3 cm (BaF_2) was combined with a hexagonal 5 mm BC400-like plastic scintillator inscribed in a cylinder of radius 5 cm (VETO) to measure the particles surviving after the target. All the passing particles were recorded, and during the analysis particles with Z=6 were selected.

The target was placed very close to the VETO detector, about 0.5 cm.

A sketch of the set-up can be found in Figure 5.21.

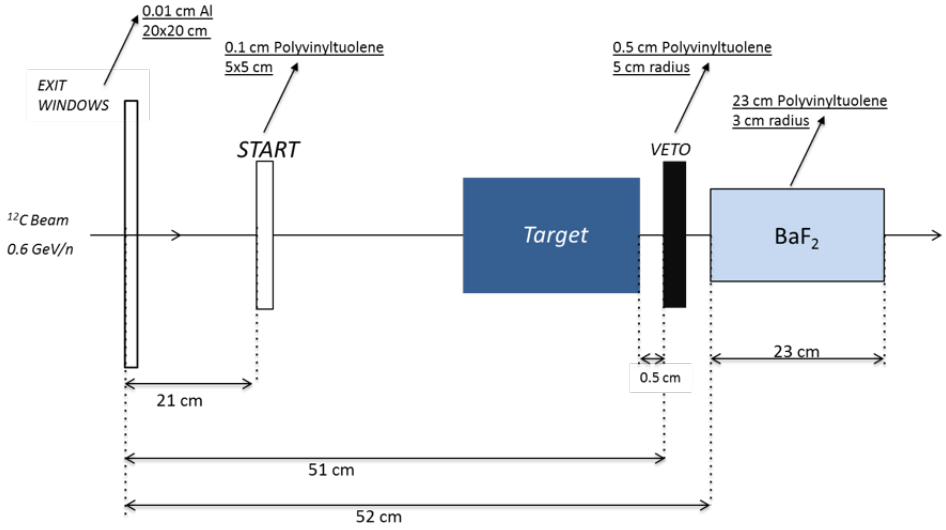

Fig. 5.21 Primary beam attenuation experiments at GSI - Experimental set-up (not in scale).

All the off-line analyses were carried out by the GSI team using the ROOT data analysis framework. Valid primary events recorded in the START detector were selected and the corresponding surviving primary carbon ions were handmade graphically chosen in the 2D-ΔE/E scatter plot.

As regards the PHITS simulations, the beam has been simulated as a mono-energetic (600 MeV/nuc) Gaussian distribution arriving perpendicular to the target and with a FWHM of 0.5 cm. Figure 5.22 reports the PHITS set up for LiH simulations. Also in this case, LiH samples have been modeled separately in the simulations.

In each simulation, air has been used to fill the empty volumes. START and VETO detectors have been built in the model as made of the same materials as in the reality (using for the VETO a cylindrical shape instead of a hexagonal one). On the other hand, the BaF_2 detector has been modeled as an air cylinder of radius of 3

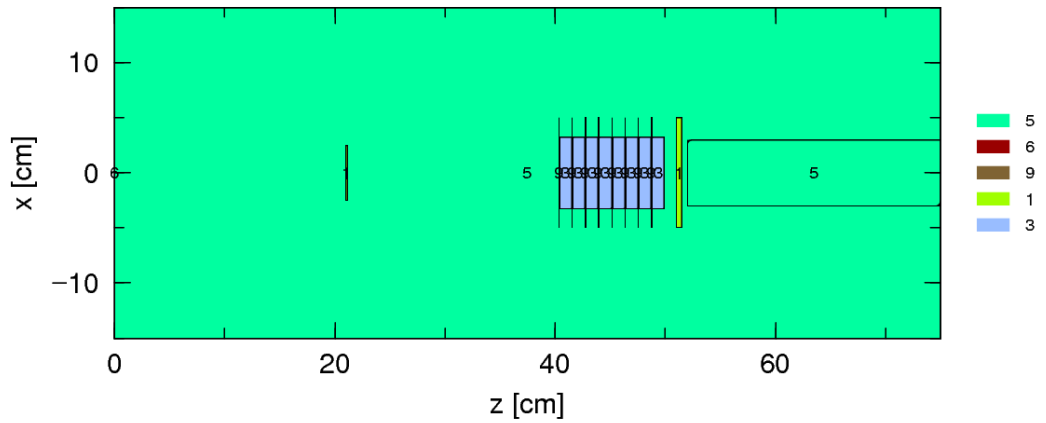

Fig. 5.22 Primary beam attenuation experiments at GSI - PHITS set up for simulations of primary beam attenuation by means of a LiH target. 1 refer to plastics, 3 to LiH, 5 to air 6 to the exit window material, 9 to PE surrounding LiH.

cm, to save computational time, considering the just the particle fluence entering this detector was important for our comparison simulations, and not the interactions with the detector itself. Figure 5.23 shows particles crossing the target (3), recorded in the VETO (1) and then crossing the BaF_2 detector (5) without interacting with it, as simulated with PHITS.

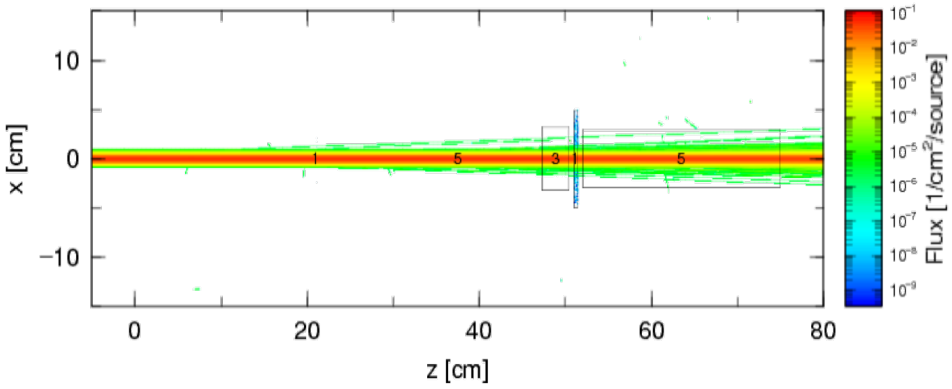

Fig. 5.23 Primary beam attenuation experiments at GSI - example of PHITS simulation of primary beam attenuation measurement. Particle crossing the target (3) are recorded in the VETO (1) and then in the BaF_2 detector (5). It is possible to see the beam spreading as it crosses materials.

Fluence (expressed as number of ions per cm^2) of Carbon ions (including all the isotopes) crossing the surface of each detector has been recorded. Initially, for each considered target the number of primary ions and generated fragments with Z=6

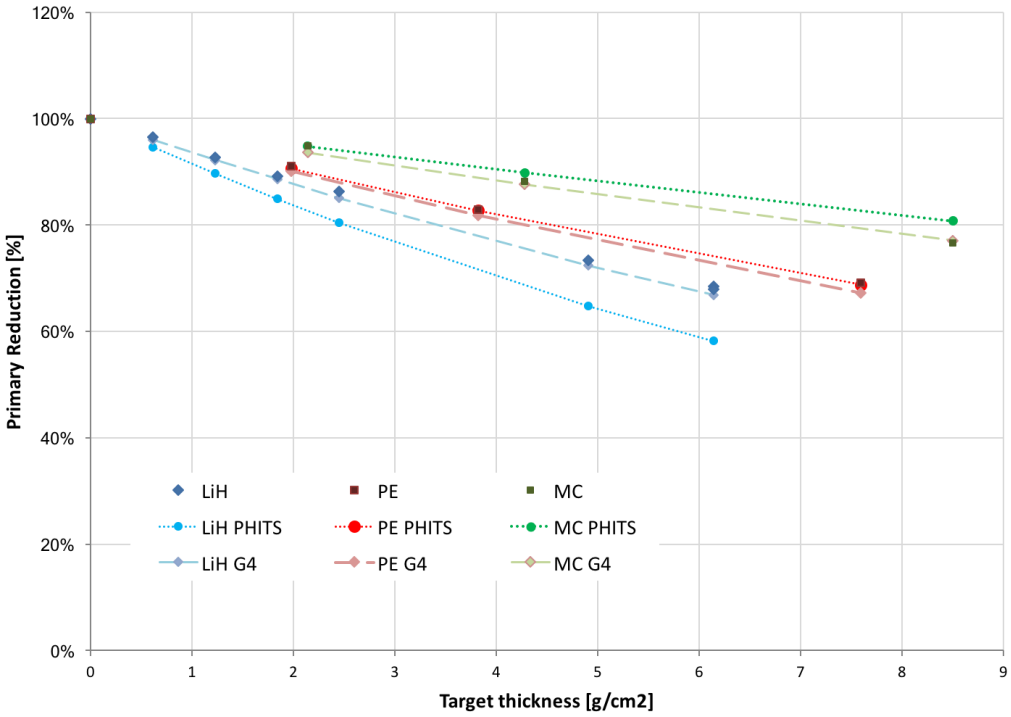

Fig. 5.24 Primary beam attenuation experiments at GSI - primary beam attenuation test results versus PHITS and Geant4 simulations. The survival fraction of primary ion carbons (considering all isotopes) is given versus target depths, where MC stands for moon concrete and PE for HDPE. Default nuclear cross section models have been used for PHITS simulations. Experimental and simulations errors are less than 1% and not shown in the graph.

reaching the BaF_2 detector has been divided by the number of the particles crossing the START scintillator, then this ratio has been normalized with respect to the BaF_2 / START ratio obtained without an interposed target.

Simulations of the survival fraction of carbon ions at 600 MeV/nuc (primary and secondary ions with Z=6) penetrating different materials have been carried out with Geant4 and PHITS and simulations results, compared with measurements, are reported in Figure 5.24.

LiH is performing very good, showing a lower survival fraction than all the other materials, HDPE included. This is due to the higher hydrogen content of LiH, which leads to a higher fragmentation cross section.

As regards simulations, agreement is very good for HDPE for both Monte Carlo codes, demonstrating the goodness of our simulation set-up. As regards moon concrete, agreement is sufficient, and is worsening with increasing thickness. This can partially be attributed to the fact that moon concrete samples are made sintering dust and both density and elemental composition could slightly vary among samples. Finally, LiH capability to fragmentize the primary beam is well described by Geant4 (using QBBC-EMY physics list), while is overestimated by PHITS (run with default nuclear models).

This inaccuracy of PHITS when LiH is concerned is observed all over LiH simulations against experimental data, leading to the conclusion that also 1D simulations with PHITS on GCR dose reduction per aeric density have been overestimated. For this reason, these simulations have partially been re-run and results shown in the previous chapter include the newer results for hydrides. An investigation of alternative nuclear models to describe the problem is discussed in a dedicated paragraph (paragraph 5.6).

5.4 Neutron production measurements at TIFPA

The Trento Proton Therapy Center has been designed to support pencil beam scanning techniques producing proton beams able to treat deep-seated tumors. Protons beams are produced with an ion source and accelerated with a cyclotron in an energy range between 70 and 230 MeV. The beam serves two isocentric gantries and one experimental room (TIFPA cave).

The ROSSINI2 experiments were performed at the 30 degree line that can deliver proton pencil beam energy in the whole energy range mentioned above, with a FWHM from 7 to 16 mm, for the highest and lowest energy, respectively. The measurements' goal was to compare the neutron production yields of different materials, in terms of ambient dose.

Three different thicknesses of the following materials were used: LiH, HDPE, Moon concrete and Aluminum 2024.

Three passive neutron dosimeters, consisting of a TLD cartridge (two TLD600H chips sensitive to photons and thermal neutrons and two TLD700H chips only sensitive to photons), were inserted in spheres made of HDPE and Lead. These

spheres were located at 90, 65 and 15 degrees with respect to the beam line, as shown in Figure 5.25. Details about these detectors and their response function can be found in [75]. All TLDs were calibrated before the experiment with a ^{137}Cs source. The conversion factor from absorbed dose to neutron ambient dose equivalent was then obtained by measurements with a ^{241}AmBe neutron source.

The incoming beam was monitored by a 20 x 20 cm^2 air-filled parallel plate ionization chamber placed outside the exit windows and a water dump was inserted at the end of the beam line to dump the beam, to reduce the extra neutron dose to the TLD dosimeters and to avoid activation of the walls. A no target measurement (and simulation) was made, obtaining the neutron dose originating from the water beam dump. This dose was then appropriately subtracted from the target-in measurements and simulations.

Results, in terms of ambient doses, were scaled to the amount of incoming primary protons (10^{12}).

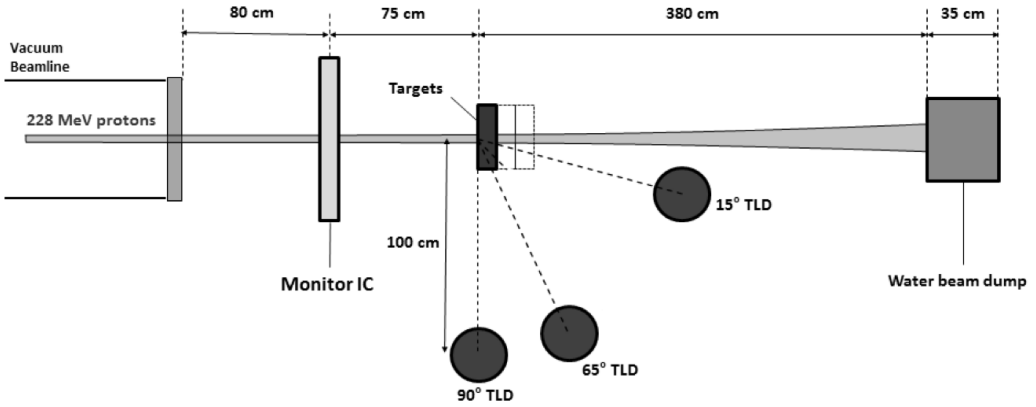

Fig. 5.25 Neutron production measurements at TIPFA - schematic drawing of the experimental setup used for neutron ambient dose measurements (not in scale) - courtesy of GSI team.

When reproducing this measurement with simulations, the whole cave has been modeled in a simplified way, to consider the neutrons produced within the water beam dump and their moderation inside the cave. One meter concrete wall has been considered, together with one meter thick ceiling and floors. Part of the beam room can be seen in Figure 5.26 (floor and ceiling not shown in the picture), reporting the PHITS calculated ambient dose due to protons in the beam room. In Figure 5.27, the neutron contribution to ambient dose, higher than the protons outside the

beam trajectory, is shown too. These plots were obtained using the ambient dose conversion factors already implemented in PHITS and automatically generated by PHITS itself as simulation input, as detailed below.

The Monitor IC and the exit window have been modeled as the one used in experiment at HIT (refer to paragraph 5.2.1). Air has been inserted everywhere in the beam room. The HDPE target, has been modeled as in reality, i.e. changing the overlap of two HDPE wedges to obtain different thicknesses. LiH samples have been modeled individually, too, also considering the thin PE layers surrounding them.

The spheres surrounding the detectors have been modeled as air filled spheres (10 cm of radius), and the real materials have not been considered, being the goal of the simulations to calculate the spectrum of neutron fluence entering each sphere.

The proton beam of energy 228 MeV was modeled in a first instance as a pencil beam of radius 0.6 cm, with direction perpendicular to the target.

During this simulation campaign several additional simulations, changing the detectors and beam parameters, were made to study how the simulated neutron ambient dose was possibly varying. Results during this robustness analysis did not significantly change.

In the simulations, once the neutron spectrum over each detector was obtained normalized per single generated (simulation) proton, a response function (from [75]) providing fluence to dose conversion factors ($pSv * cm^2$) was applied to obtain the neutron ambient dose[2].

Because PHITS is not generally providing data on particles but only integrated results, a modification was implemented in our PHITS macro, and information (such as position, velocity, energy, etc..) on particles crossing the detectors were dumped into a text file, then read by ROOT and translated into a histogram. Afterwards, particles were grouped into energy bins as those of the response function, and the coefficients were applied to convert from fluence to ambient dose. Finally, each energy beam contribution was summed up to obtain an integral result. An example of the data saved for each simulation is given in Figure 5.28, reporting the position (x,z) of the neutrons crossing the detector sphere versus their energy. It is possible to

[2]In [75] measured dose values are compared with dose values derived from calculated neutron spectra folded with dose conversion coefficients

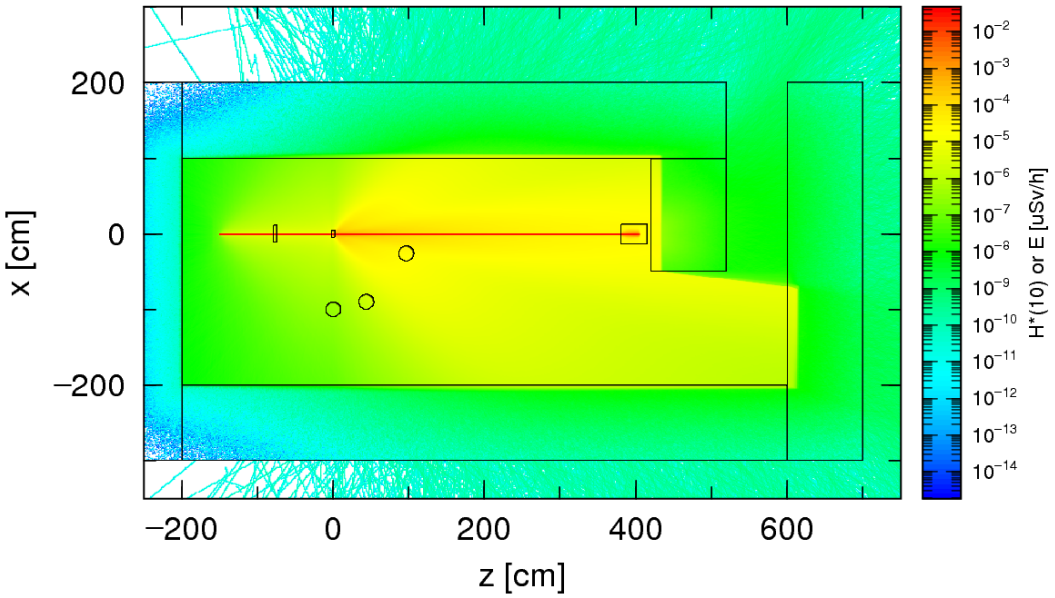

Fig. 5.26 Neutron production measurements at TIPFA - proton contribution to the ambient dose, not normalized, as simulated in PHITS (no target) using the ambient dose conversion factors already implemented in PHITS. Ambient dose expressed in uSv/h - Trento Proton Facility beam room.

see how higher energy neutrons arrived from the direction of the target, while on the other side only low energy background neutrons reach the detecting sphere.

In Figure 5.29 results from PHITS simulations and experimental data are compared.

We can see how the neutron ambient dose is increasing with the target thickness and with decreasing angle, as expected.

Considering the PE target peculiar shape, some self shielding effects could happen and this could be one of the reasons why PE results as the material producing less neutron ambient dose (by a factor of about 2 with respect to LiH, at higher thicknesses). However, this should be reproduced by the code and therefore the measurement of the highest thickness point could just be an outlier.

Aluminum seems to generate lower neutron ambient dose that LiH in the forward directions, while at 65 and 90 degrees the results are similar.

Considering that the TLD are calibrated with radioactive source introducing uncertainties of about 20-30%, good agreement is found when comparing simulations and experimental data for the larger angles (65 and 90 degrees), however PHITS

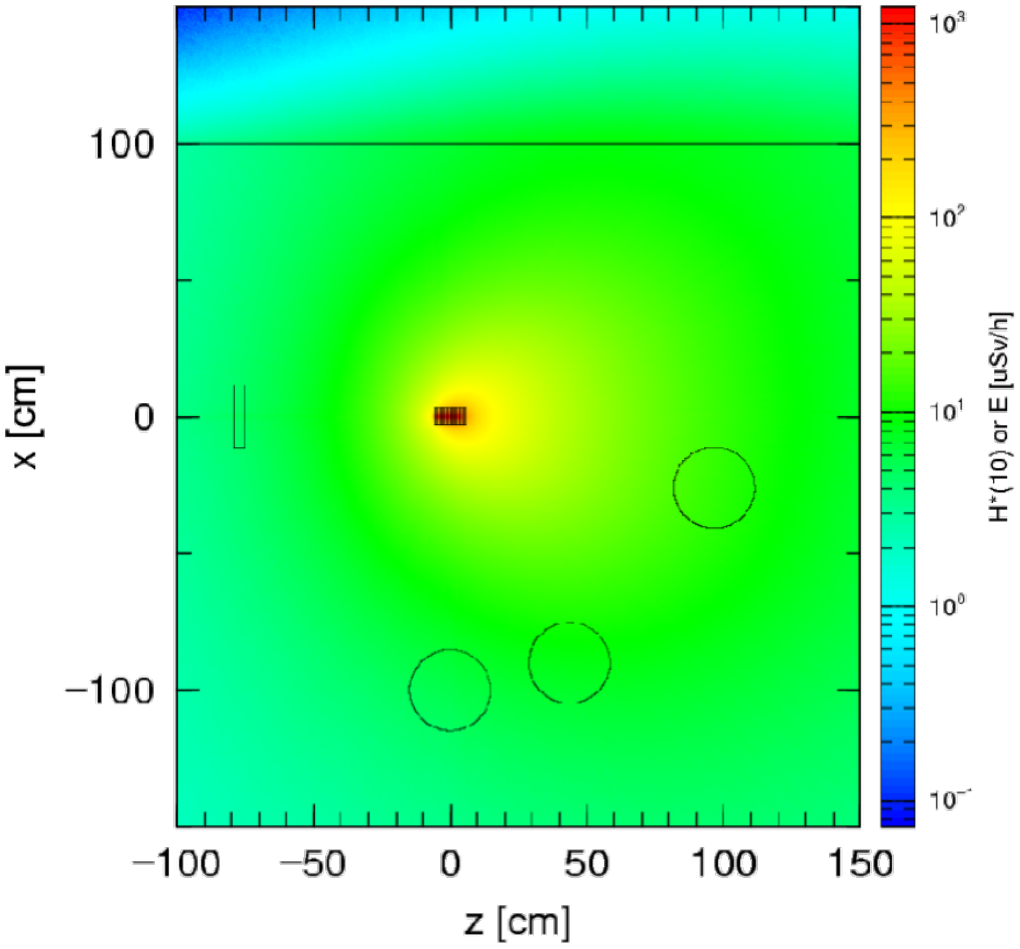

Fig. 5.27 Neutron production measurements at TIPFA - neutron contribution to the ambient dose, not normalized, as simulated in PHITS (with 10 slabs of LiH) using the ambient dose conversion factors already implemented in PHITS. Ambient dose expressed in uSv/h - Trento Proton Facility beam room.

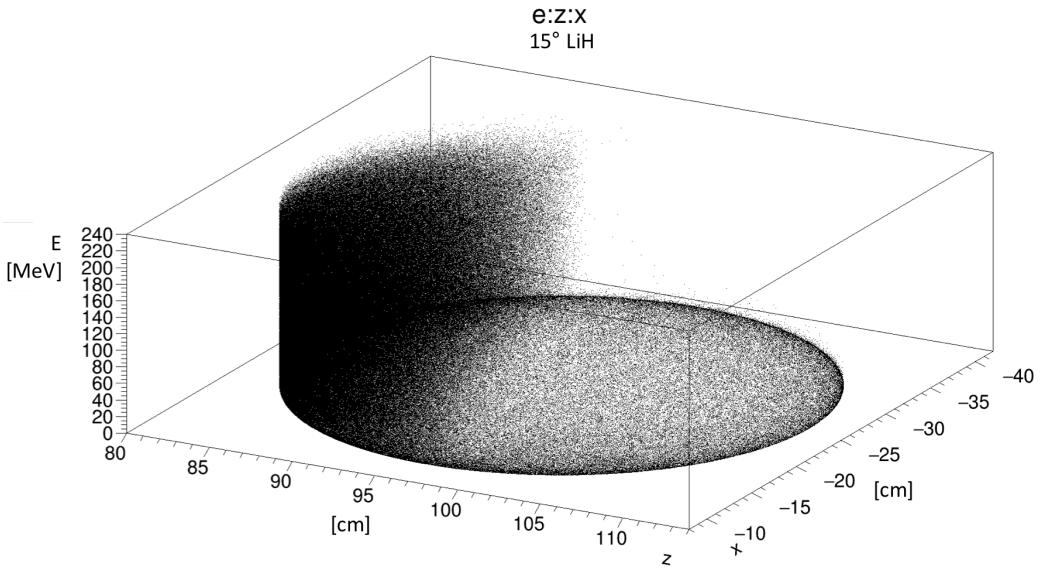

Fig. 5.28 Neutron production measurements at TIPFA - The energy (E) of neutrons crossing the 15° detector sphere in position x,z is shown. Faster neutrons arrive from where the target is placed (denser region), while on the other side only background, back-scattered neutrons are reaching the sphere - Plot created with ROOT.

underestimates the neutron doses of the 15 degrees detector of about 2.5 times. The origin of the discrepancies needs further investigation in terms of additional measurements with targets with possibly uniform dimensions, but possible causes could be the nuclear cross section models implemented in PHITS.

However, some simulations have been made with different nuclear models and results did not seem to improve.

5.5 Microdosimetry test at TIFPA

In the framework of ROSSINI2 project, microdosimetric distributions have been simulated with PHITS Monte Carlo code and compared with results of the test carried out at Trento TIFPA facilities in December 2016. The Tissue Equivalent Proportional Chamber (TEPC) detector used in the experiment is the Model LET-1/2, Far West Technology. It is a spherical Tissue Equivalent (TE) proportional counter suitable for measuring the LET spectra of absorbed dose in the detector. TE proportional counting gas is stored at a low pressure to enable the spherical detector volume to simulate a small tissue volume of 2 microns in diameter. In this way, one can

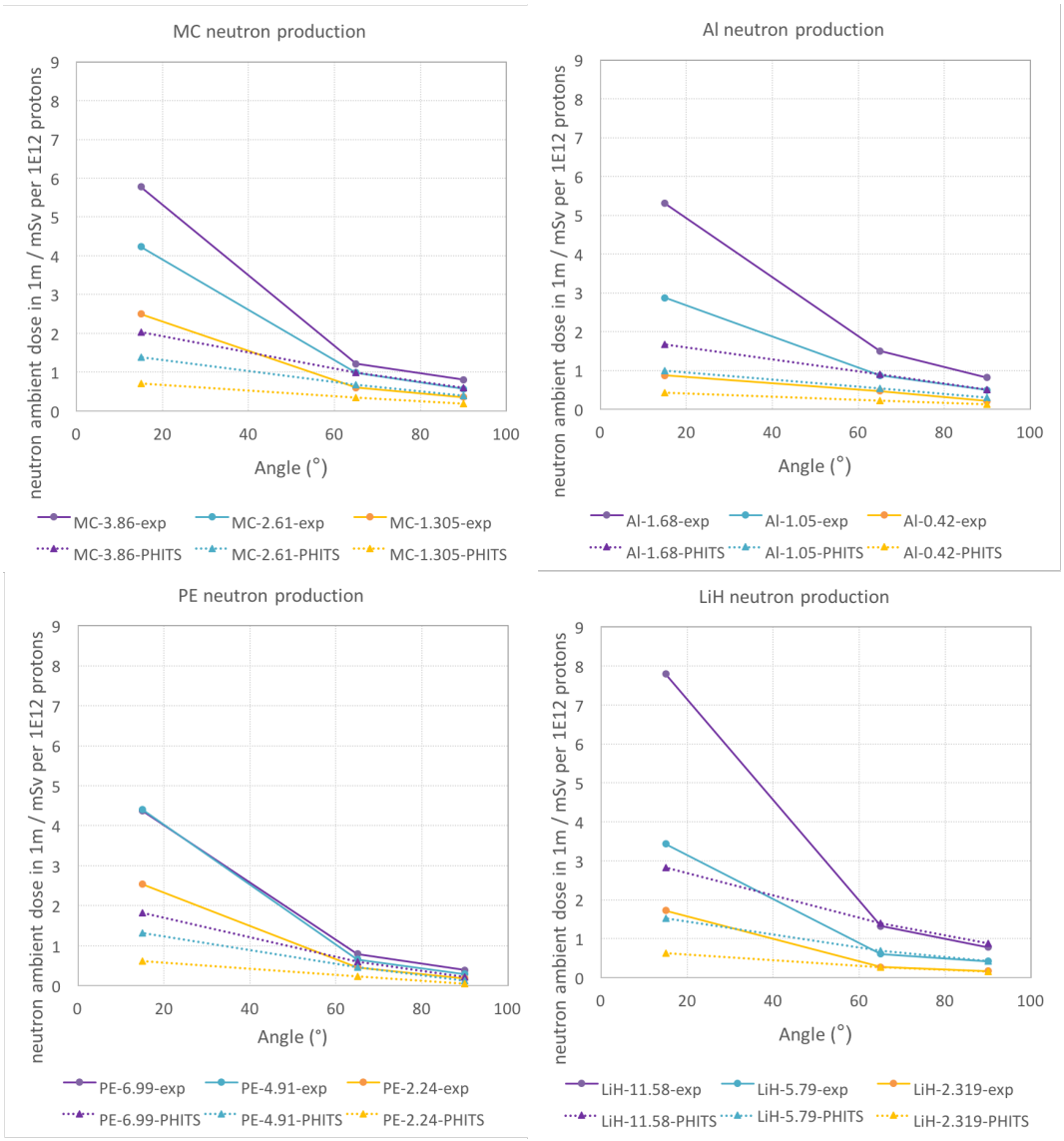

Fig. 5.29 Neutron production measurements at TIPFA - PHITS simulations of ambient dose compared to experimental data. Simulation errors are lower than 1% and not shown in the graph. Errors on experimental data are estimated to be less than 15%.

correlate the deposited energy to the sensitive gas with the one deposited to a cell nucleus. Moreover, it is possible to correlate the resulting microdosimetric quantities to the radiation quality factors.

The geometrical details of the set-up can be found in Figure 5.30. The parameter d1, the distance between the beam monitor and the beginning of the target, has been varied depending on the targets.

Before further describing the simulations, a brief definition of microdosimetric quantities is given, being them not generally used in space radiation context.

The probability distribution, y, for lineal energy is

$$y = \frac{\varepsilon}{\bar{l}} \tag{5.5}$$

where ε is the deposited energy in the sensitive volume used as a detector and $\bar{l}$ is the mean chord length of the sensitive volume.

y varies from one event to another, therefore the frequency mean energy $\bar{y}_f$ is introduced as:

$$\bar{y}_f = \int_0^{-\inf} y f(y) dy \tag{5.6}$$

$\bar{y}_f$ is the first moment of the probability density function $f(y)$ and can be used as an approximation for the linear energy transfer.

In the PHITS Monte Carlo simulations the detector has been modeled as a spherical ionizing chamber filled with a tissue equivalent gas, surrounded by a spherical wall made of tissue-equivalent plastic. The detecting sphere has been placed in a cylindrical vacuum chamber isolated from outside by a thin aluminum shell (Figure 5.31).

The actual materials and dimensions of both targets and beam line have been implemented in the simulations as accurately as possible. Propane (55%) was assumed as TE gas, with addition of CO_2 (39.6%) and N_2 (5.4%); NIST material Shonka A-150 plastic was assumed as the spherical shell containing the TE gas. No TEPC wires were however considered in the simulations. The detector wall thickness was 0.127 cm, the inner diameter 2.54 cm and the density of the Shonka A-150

plastic 1.12 g/cm^3. The external can containing the sphere was modeled as a 0.0178 cm thick aluminium layer.

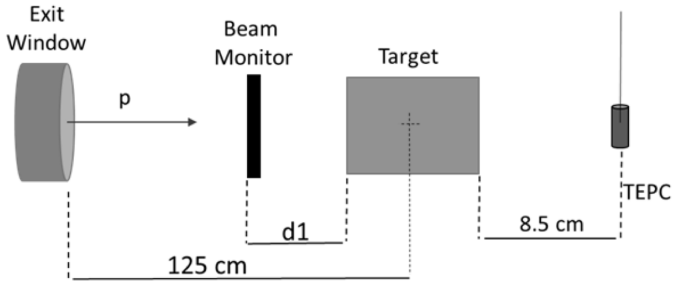

Fig. 5.30 Microdosimetry test at TIFPA - Set-up used for the measurements (not in scale).

Simulations cut-off energies have been changed from default values to 1E-10 and 1E-3 MeV for neutrons and photons, respectively. All the others parameters have not been modified from PHITS default. The updated version of the Event Generation Mode (egm v2), available at the time of the microdosimetry simulations, has been used.

The proton beam has been modeled as a circular beam perpendicular to the target surfaces, characterized by a mono-energetic Gaussian distribution with varying FWHM, depending on the beam energy. The following beam parameters have been assumed in the simulations (values expressed in millimeters):

- 148 MeV: X-FWHM = 4.52*2.355, Y-FWHM = 4.51*2.355
- 100 MeV: X-FWHM = 5.81*2.355, Y-FWHM = 5.86*2.355
- 70 MeV: X-FWHM = 6.87*2.355, Y-FWHM = 6.91*2.355

All the elements found in the beam line (nozzle and beam monitor) have been modeled using their water equivalent thicknesses, while the exit window has been reproduced as a thin slab of Titanium (70 micron).

Figure 5.31 shows an example of the flux (normalized per generated event) resulting from 148 MeV protons impacting in 9 cm of PBI target. In particular, in the upper frame the flux from all particles is shown, while on the lower frame only proton flux is reported.

The following materials have been tested: LiH, Moon regolith and PBI.

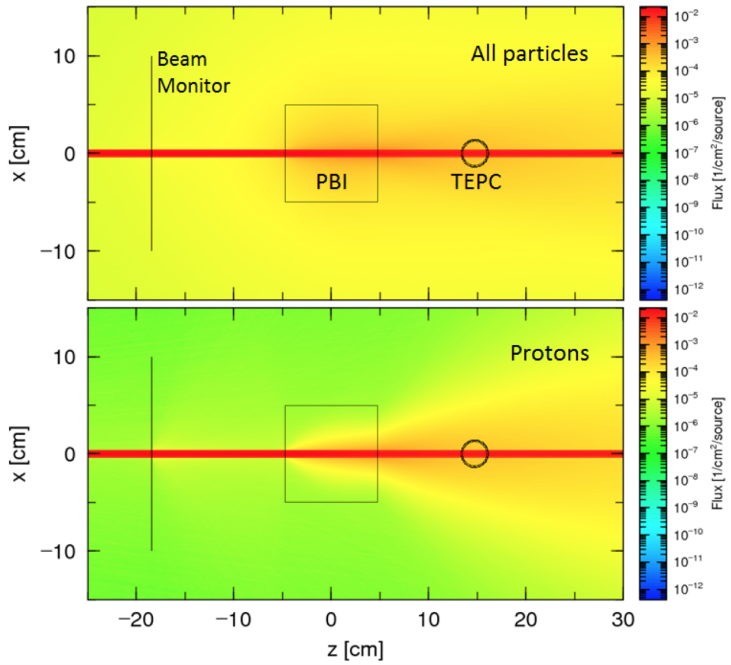

Fig. 5.31 Microdosimetry test at TIFPA - PHITS set-up for simulations with PBI target. The upper frame shows the flux of all the particle species in the simulated volume, while in the lower frame the only proton flux is reported.

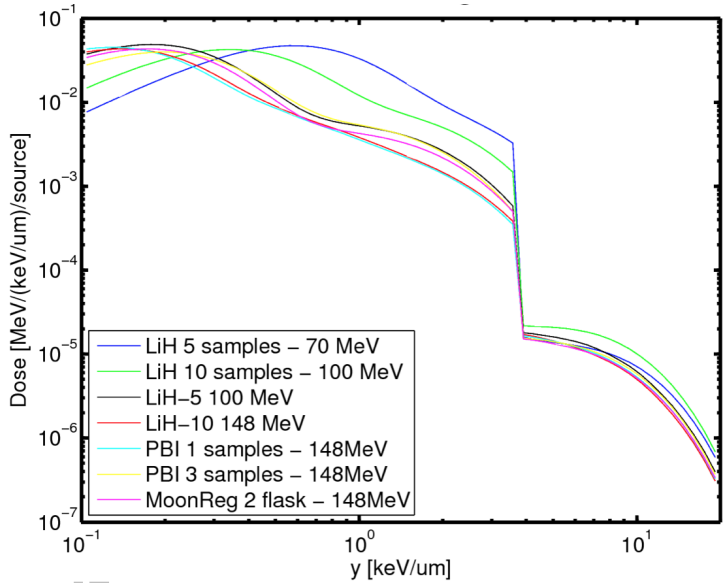

Fig. 5.32 Microdosimetry test at TIFPA - Linear energy distribution calculated with PHITS for different targets and proton energies.

Figure 5.32 reports the resulting lineal energy distributions in the TEPC detector after the selected materials, also here referred as "microdosimetric dose" or only "dose", expressed in MeV/(keV/μm)/source and in MeV/ln(keV/μm)/source, obtained from PHITS simulations. A tail at higher y can be noticed, probably produced by fragments of the interaction.

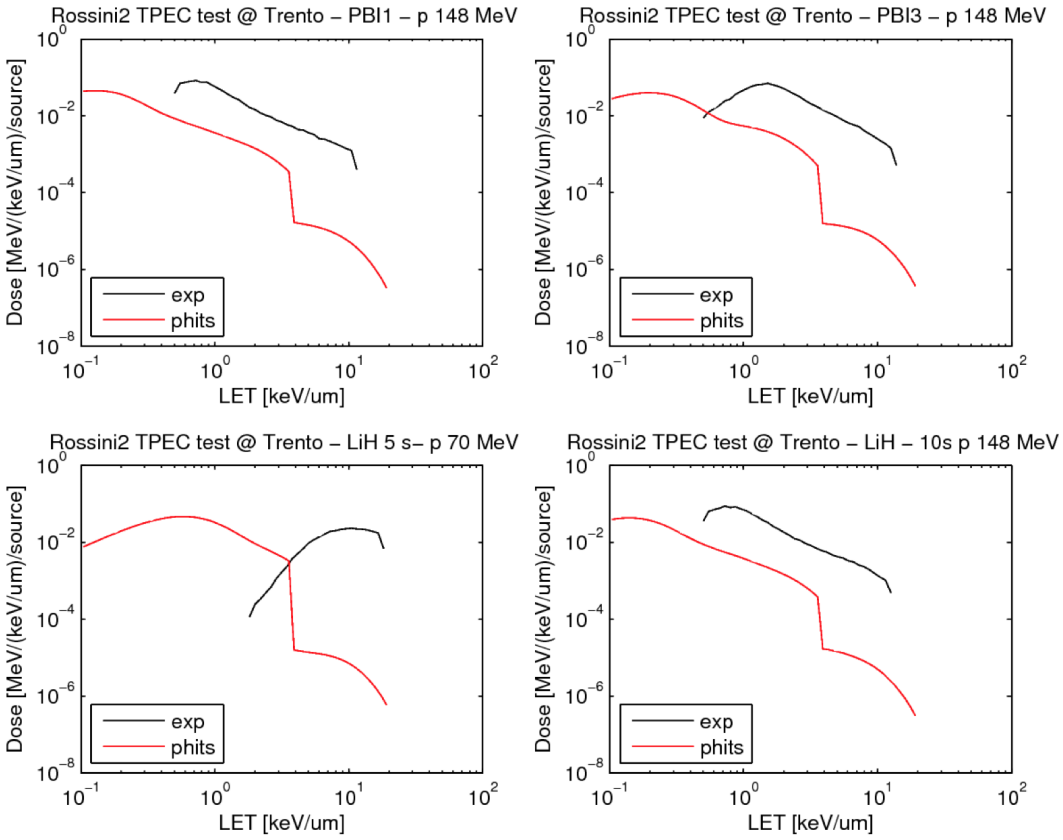

Fig. 5.33 Microdosimetry test at TIFPA - Linear energy distributions calculated with PHITS for a subset of microdosimetry measurements (red lines) and compared against experimental data (black lines). The upper figures report data for 1 (left) and 3 (right) PBI slabs, tested with a proton beam at 148 MeV. The figures at the bottom show the results for 5 (left) and 10 (right) slabs of LiH, tested with protons at 70 and 148 MeV, respectively.

Figure 5.33 reports comparisons with experimental data for a subset of measurements.

The experimental data seem to be shifted to higher y with respect to the results of PHITS simulations. This disagreement could be ascribed to two main reasons. Either a miscalculation of the in-beam calibration procedure, which is a trivial step of the data analysis and more accurate checks or eventually a new calibration test

need to be performed or there is an underestimation of the yields of the secondary fragments produced (especially protons and neutrons) due to the physical models uncertainties implemented in the codes.

5.6 PHITS simulations of LiH - nuclear cross section study

A parameter optimization campaign dedicated to light projectile and target nuclei interactions was carried out at the end of the study, evaluating different nuclear cross section models implemented in PHITS, in an attempt to solve simulations-tests discrepancies found for LiH.

In particular, PHITS v2.80 uses as default the NASA model for nuclear cross section, and we decided to compare it with the implementation of Shen and Kurotama nucleon-nucleus and nucleus-nucleus cross-section formulas.

Details on the KUROTAMA model, the one better reproducing LiH, can be found in [76]. This model is based on the Black Sphere cross section formula [77] and it presents an overall better agreement with a part of the experimental data than earlier models.

Figure 5.34 shows the simulation results concerning the dose reduction tests at HIT, where LiH samples were irradiated with a ^{12}C beam at 430.1 MeV/nuc of energy and simulations are carried out using different nuclear models. We can see that Kurotama model is better reproducing light ions beams interactions with low atomic number materials, such as LiH, while the default PHITS model (the model developed by NASA) overestimated LiH performances, as also seen in all the simulations presented in the previous sections of this chapter. The agreement with data of these alternative nuclear models is very good for the first experimental points, while with increasing thicknesses also Shen and Kurotama models predict a higher dose reduction than the measured one.

Figure 5.35 shows the simulation results reproducing the GSI primary beam attenuation test at GSI (^{12}C beam at 600 MeV/nuc of energy). Also in this case the agreement is very good for the first experimental points, while some differences can be noted in the number of primary beam entering the BaF_2 detector, leading to the

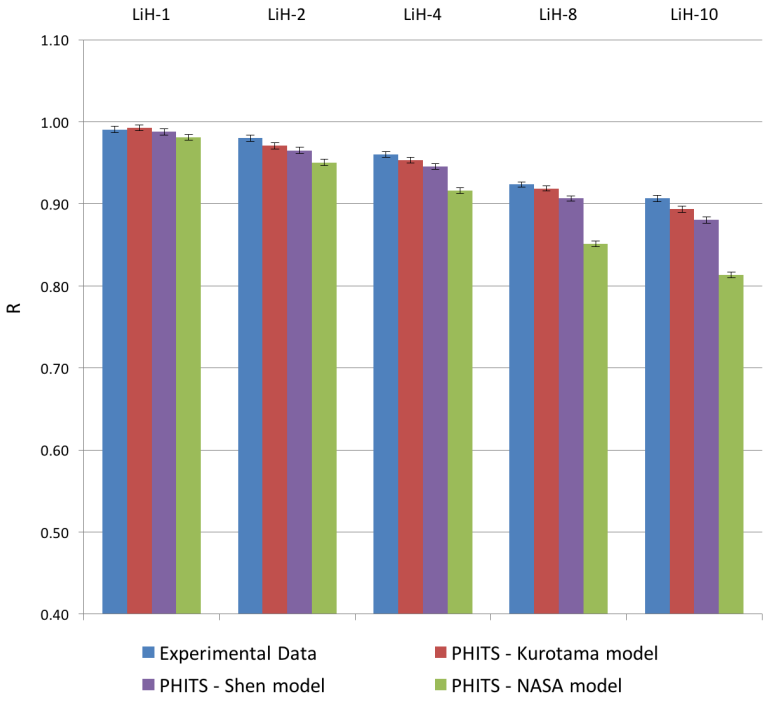

Fig. 5.34 Dose reduction experiments at HIT - Comparison of the reduction factors obtained irradiating a LiH target with 430.1 MeV/nuc carbon ions, simulated varying the PHITS nuclear cross-section model .

conclusion that all models available in PHITS are at least slightly overestimating LiH capability to fragmentate the incoming beam when thick enough LiH samples are considered.

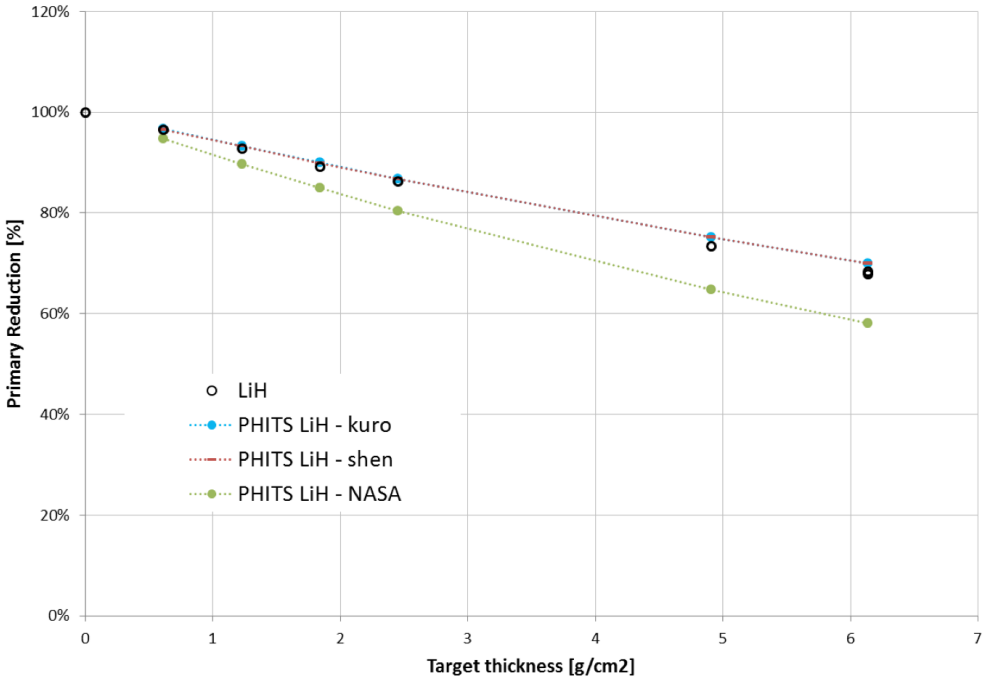

Fig. 5.35 Dose reduction experiments at GSI - Comparison between the experimental reduction factor measured irradiating a LiH target with 600 MeV/nuc carbon ions and the one calculated with PHITS using different nuclear cross-section models, where "kuro" and "shen" stands for Kurotama and Shen models, respectively.

As regards instead neutron production from 228 MeV protons, several simulations have been carried out with two total reaction cross section models of PHITS (Tripathi and Kurotama) and similar results in terms of ambient dose were obtained.

In conclusion, when simulating light GCR interactions with light hydrides, the use the Kurotama model is recommended to obtain the total reaction cross section, which is essential to determine the mean free path of a transported particle.

5.7 Fragmentation measurements at NSRL

Data analysis and simulations are still on-going to reproduce the double differential neutron production cross section test, performed at NSRL (BNL) in June 2016.

Different depths of LiH have been chosen (1.06 and 6.14 g cm^{-2}) and were exposed to a 972 MeV/nuc ^{56}Fe beam to investigate the production of secondary light particles (Hydrogen isotopes and neutrons) from nuclear fragmentation of the primary radiation. The measurements were acquired also with a 5.24 g cm^{-2} polyethylene target, chosen as reference material.

Ten samples of LiH were also irradiated with a 1000 MeV/nuc ^{4}He beam to test its behavior when exposed to a light ion.

The number of primary particles impinging on the target was monitored with two plastic scintillators referred to as S1 and S2 (thickness 0.2 cm, 1x1 cm^2 and 2x2 cm^2 active area, type BC400). Fragments exiting the targets were detected by two telescopes, placed at 10 and 45 degrees with respect to the primary beam direction and at a distance of 3.5 m from the target center. Each telescope was composed by a plastic scintillator referred to as N1V1 or N3V3 (thickness 0.635 cm, 12.7x12.7 cm^2 active area, type BC400) followed by a liquid scintillator referred to N1 or N3 (12.7 cm active diameter, 12.7 cm length, type EJ301). Figures 5.36 and 5.37 report sketches of the experimental set-up, before and after the target, respectively. They also report information on each material and thickness assumed in the PHITS simulations.

An event seen by the telescope was recorded only if correlated to a primary particle arriving on the target. Energy loss and Time Of Flight (TOF) were acquired for all detectors.

The data analysis for these measurements is very complex and is still under evaluation. In the meanwhile, preliminary simulations have been carried out, calculating the secondary particles flux at 10 and 45 degrees.

An example of proton production from the interaction of of 1 GeV/nuc ^{56}Fe and ^{4}He beams with 10 LiH samples is shown in Figure 5.38, as simulated with PHITS. Simulations data on each particles crossing the detectors have been dumped on text files, then analyzed using the ROOT software. The data reported in the figure are not normalized.

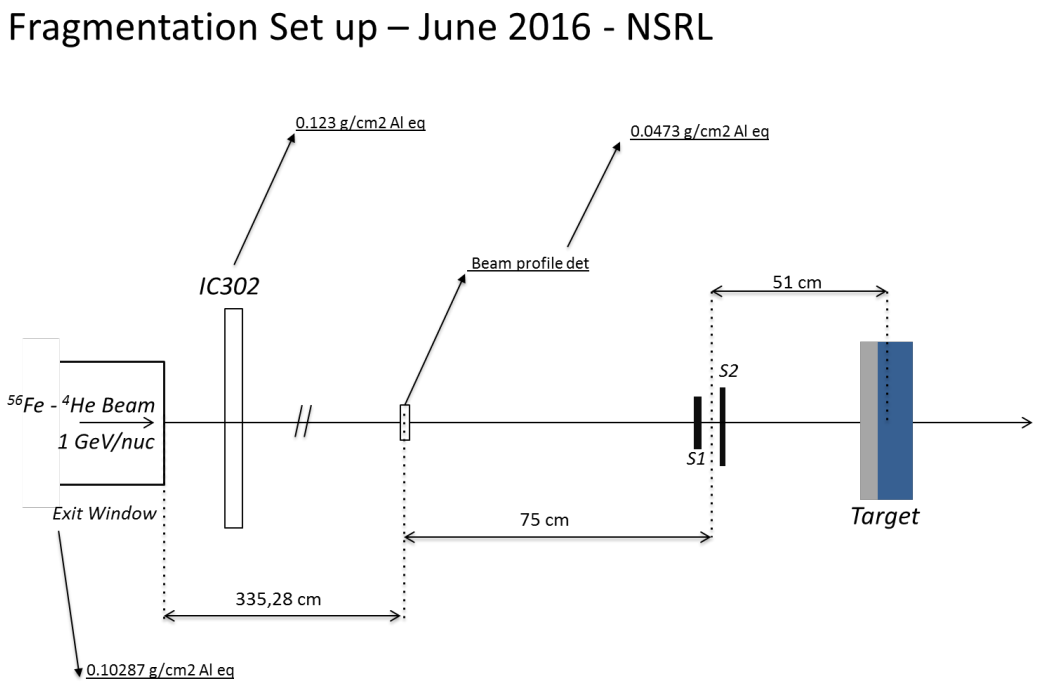

Fig. 5.36 Fragmentation experiment at BNL-NSRL - Set-up before target focus (not in scale).

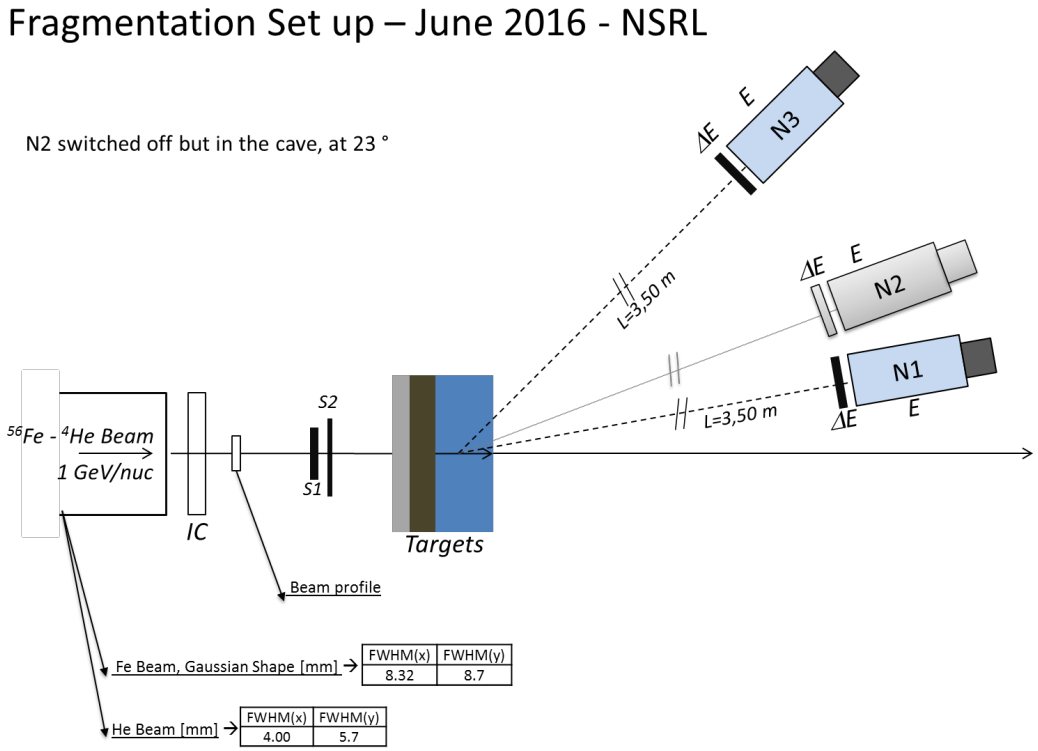

Fig. 5.37 Fragmentation experiment at BNL-NSRL - Set-up after target focus (not in scale).

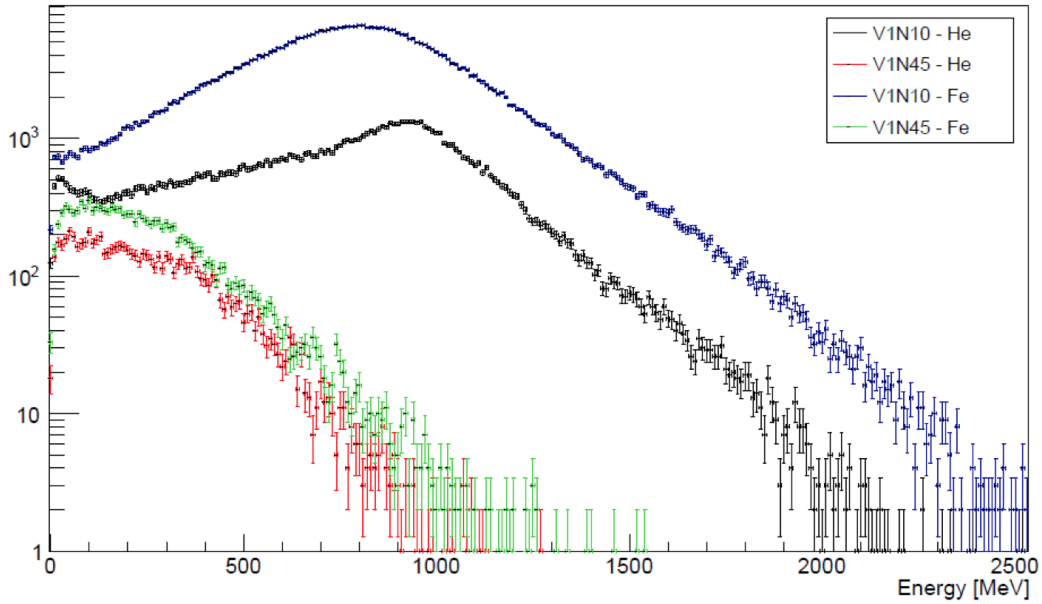

Fig. 5.38 Fragmentation experiment at BNL-NSRL - proton production from 1 GeV/nuc ^{56}Fe and ^{4}He beams crossing a target made of 10 LiH samples, at different angles (10 and 45 degrees) – PHITS simulation, results are not normalized.

5.8 Putting all together

PHITS and GRAS/Geant4 ability to reproduce radiation measurements involving HZE particles has been confirmed in the framework of this study.

GRAS/Geant4 resulted slightly better when light projectiles - light nuclei interactions were involved, while PHITS was able to reproduce high energy iron beam behavior in a more realistic way. Considering that both codes were generally in agreement with measurements and their performances similar, they both qualify to be used for 3D Monte Carlo simulations of realistic exposure situations.

Therefore, at the beginning of this work, both codes were used in an attempt to calculate doses and doses equivalent for a crew involved in a Moon mission. However, soon it was realized that GRAS/Geant4 was more suited than PHITS when trying to reproduce complex geometries. In particular, it was possible to create geometrical models through dedicated modeling software (such as FASTRAD or FREECAD) and then to convert them in a format compatible with GRAS/Geant4. The same was not possible for PHITS, leading to gigantic modeling time.

For this reason, 3D simulations presented in the following chapter (Chapter 6) have been performed only with GRAS/Geant4.

Chapter 6

Simulation of a Moon habitat

A Moon base is one of the most promising space project of our time. It is considered an enabling step for deep space long duration missions and needs the development of many key technologies. Among those, radiation protection is one of the main challenges, considering that the Moon has neither atmosphere nor a magnetic field, therefore astronauts and electronics will be exposed to the complete deep space radiation environment (details can be found in Section 1.7.3).

Short term missions on the Moon will need to foresee areas where the crew will be protected from SPEs, while GCR and the secondary neutron albedo will be a hazard for long term missions.

Geant4 simulations of different Moon exposure scenarios have been carried out with the goal of calculating crew radiation exposure during a Moon surface mission. A modular habitat model has been created and iterations have been made to simulate different degrees of shielding. A deep space exposure simulation has been made too, to perform comparisons with existing literature and with Moon surface results.

The habitat has been realistically created, with materials and thicknesses selected referring to the experiments and simulations described in Chapter 5 and to other space projects. This work reports results for a standard aluminum-based habitat, without iterating different shielding materials configurations, however on-going simulations will include iterations using Lithium Hydride and possibly others materials as shielding layers, to evaluate their effectiveness in reducing the dose in a realistic scenario.

Simulations have been run on Thales Alenia Space Italia 8x Dell PowerEdge M620 blade servers already described in Chapter 4.

6.1 Geant4 model description

6.1.1 Moon soil composition and density

When calculating the exposure in the Moon scenario case, Moon soil needs to be modeled. The Moon surface is primarily composed by several oxides. In the simulation only the Lunar soil was modeled, meant as the first layer of fine powdery soil, characterized by scattered rocks, also called Moon regolith [78]. The Lunar soil composition used is reported in Figure 6.1: Oxygen (42%), Silicon (21%), Iron (13%), Calcium (8%), Aluminium (7%), and Magnesium (6%), with a bulk density of 3.4 g/cm^3.

Two different materials with the same elemental composition and different density have been created in Geant4, to consider the different densities of compacted and uncompacted soil, the latter referring to the one placed above the habitat in the buried habitat scenario (see Section 6.1.2 for details).

The Moon surface has been modeled as a 10 meters high box of compacted moon regolith, with a square base with sides of 25 meters.

6.1.2 Moon habitat model geometry

A habitat has been designed and simulated for an early long term exploration scenario: small volumes, where astronauts are going to spend from some months to a year while performing activities, such as scientific research and local resources exploitation, to enable the development of yet to come self-sufficient colonies. In this exploration scenario, protection from GCR and SPE, as well as meteoroids must be provided.

The concept has been designed on the hypothesis of reusing the ISS rigid modules geometries, i.e. Aluminum cylindrical habitats, with embedded MDPS, here not separately modeled, but included in the Aluminum structure surrounding the pressurized volumes. Different options have been simulated starting from this basic module;

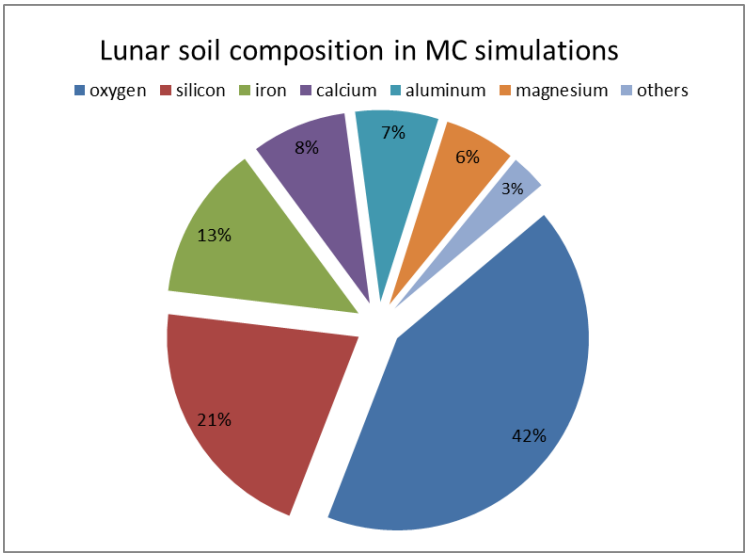

Fig. 6.1 Lunar soil composition used in the Monte Carlo simulations.

in a first version the habitat is placed above the Moon surface, then a protection from radiation and meteoroids is added, in the form of a Moon regolith dome.

Another simulated version includes the heavily shielded case with the habitat inserted in a 5 meters deep cavity in the Moon soil and covered with Moon regolith, to quantify the resulting additional protection against radiation.

Of course, considering the use of Moon soil to provide protection against radiation translates into the need of using heavy equipment to move, handle, manipulate and transform Moon regolith.

Habitat requirements

Considering a long duration mission, at least about 90 m^3 per crew member is recommended by space agencies, including also stowage and subsystem volumes. A crew composed by 4 astronauts would therefore require about 360 m^3 of habitable volumes. 2.2 m^3 crew sleeping quarters have been foreseen (2.3 x 1.2 x 0.8 m), one for each of the 4 crew members.

A total amount of 2.8 tons of water has been included both as potable, reserve and service water, and placed in our simulation model above the ceiling, to provide further radiation protection. No detailed description of water storage system and internal outfitting is given for the moment.

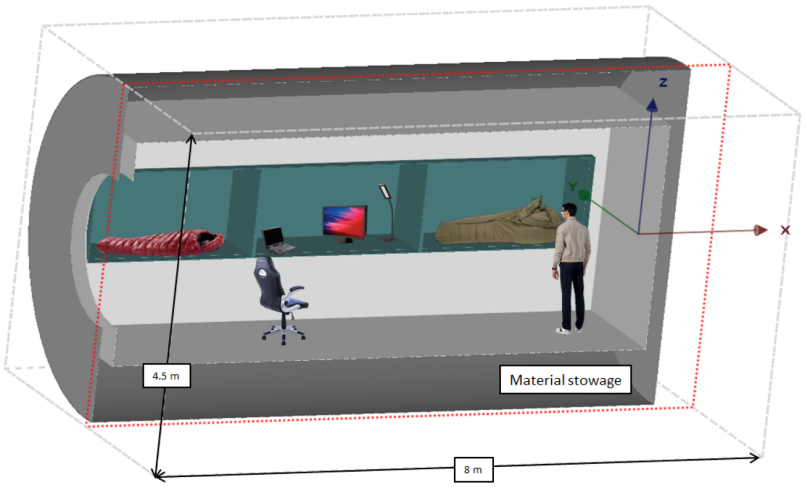

Fig. 6.2 Internal habitat configuration showing 2 crew quarters and material and water storages, below and above the habitable section, respectively.

A 4.5 meters diameter, 7.9 meters long habitat has been selected as the basic unit of the architecture, with an equivalent aluminum wall whose thickness is 20 cm has been modeled as primary structure to consider the large amount of materials and systems which will be located around the habitat. A picture also showing possible internal configuration is given in Figure 6.2. Two habitat units have been modeled, linked by an airlock placed between them, which for the buried habitat scenario vertically extends to allow the astronauts to go outside the habitat passing through it.

The dome scenario is characterized by a 60 centimeter thick Moon soil 3D printed structure placed all around the habitat with a radius of 6.5 meters, as shown in Figure 6.3.

Figures 6.4, 6.5 and 6.6 show some details of the buried habitat scenario. In particular, Figure 6.4, taken from the Radiation Exposure and Mission Strategies for Interplanetary Manned (REMSIM) study [79], shows the sketch which was used as starting point of this activity. Figures 6.5 and 6.6 are screenshots of the Geant4 model of the buried habitat. It is possible to see two colored spheres inside the module, green and purple, made of air and inserted in the model to measure the fluence crossing their surface, as explained in Section 6.1.5, while the water and the food reserves are in blue and red, respectively.

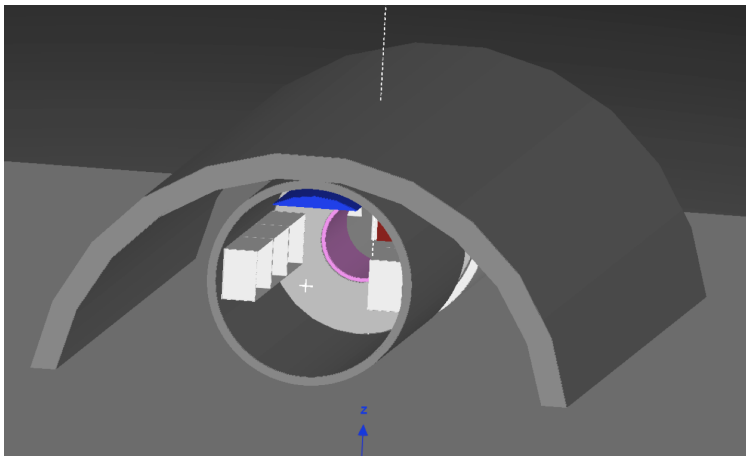

Fig. 6.3 3D printed Moon regolith dome, in a simple configuration, made of 60 cm thick regolith layer, with a radius of 6.5 meters.

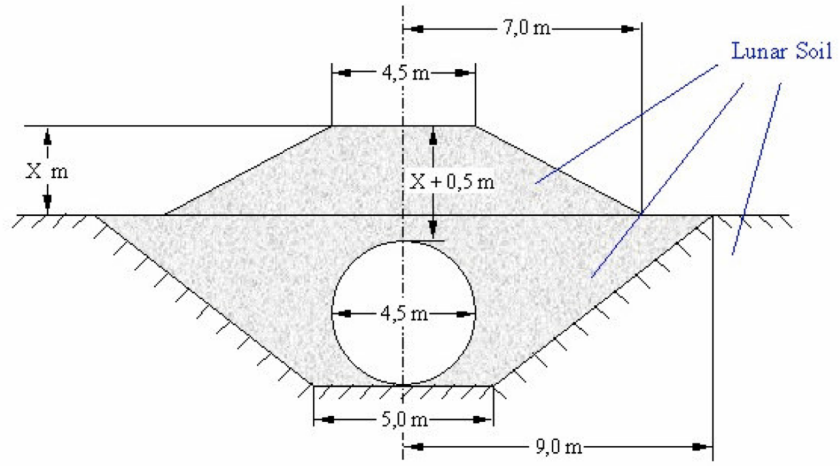

Fig. 6.4 Buried habitat design for Moon scenario, as described in the REMSIM final report.

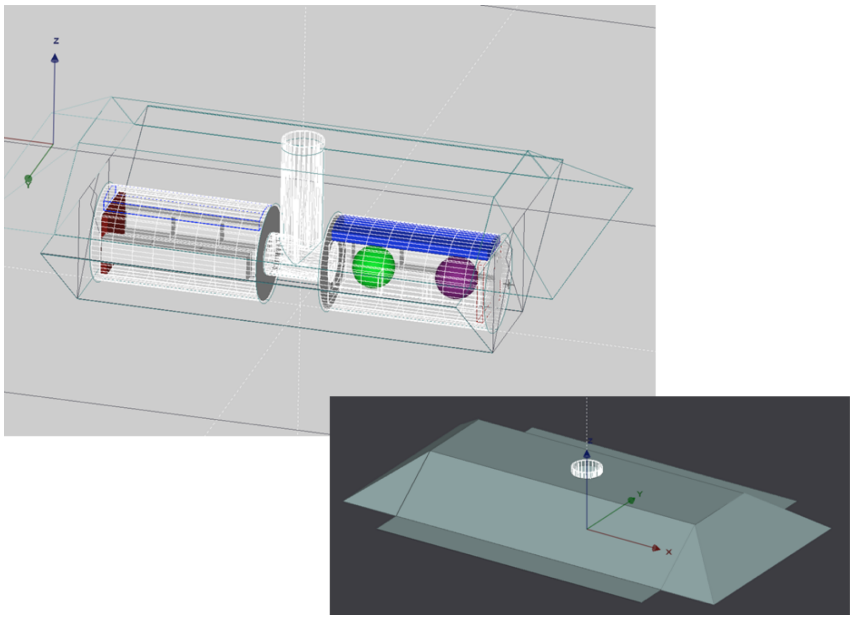

Fig. 6.5 Geant4 simulations model of buried habitat design. Radiation fluence is recorded on the green and purple spherical surfaces.

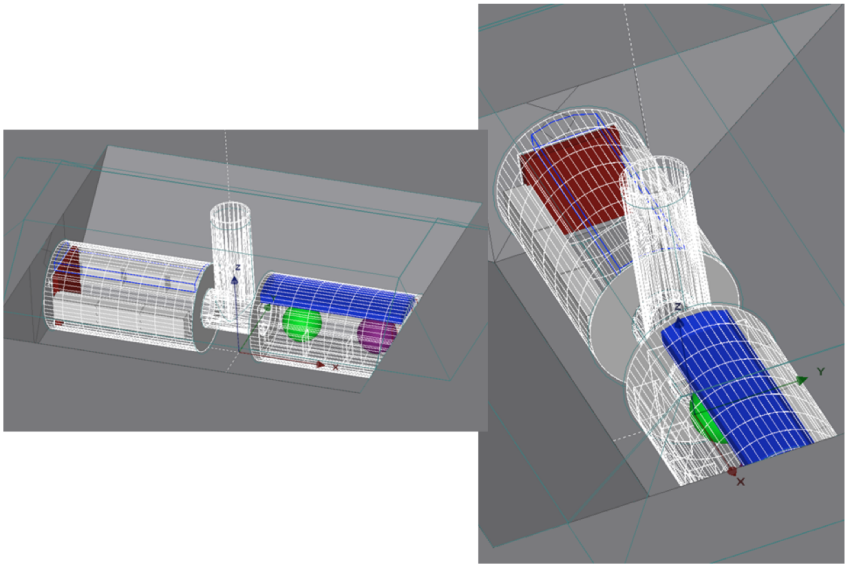

Fig. 6.6 Details of the Geant4 simulation model for the buried moon habitat. Blue: water reserves; red: food reserve.

Habitat simulation models

Different simulation models have been created, based on the above-mentioned habitat:

1. Base **MH** model: the Moon Habitat (MH) is below the moon soil, corresponding to model reported in Figure 6.6.
2. MH – **moon only** model: all the materials constituting the MH have been set to vacuum, to study moon soil and habitat structures impact on dose reduction
3. MH – **surface model**: MH is placed on the moon surface, without additional protection, this model could be representative of the astronaut exposure when working in laboratories for small amount of time, such as greenhouses.
4. MH - **surface – cupola** model: MH is on the moon surface, but this time a moon concrete structure has been created to protect it from the radiation and debris environment. A picture of this model is reported in Figure 6.3.
5. MH – **deep space**: the MH is simulated as if it was in deep space, to study the different induced secondary radiation field and the dose reduction due to the moon presence itself.

6.1.3 Radiation environment

A SPE simulation has been carried out only for the surface exposure scenario (scenario number 3), while GCRs have been simulated for each scenario.

Particles have been sampled isotropically using an inward direction with the built-in cosine law biasing option included in GRAS/Geant4 [66] source parameters. Differential fluxes have been interpolated up to 500 MeV and 10^5 GeV/nucleon for SPEs and GCRs, respectively. All secondary particles were traced except those below their cut-off energies, kept as GRAS/Geant4 default.

Particles have been generated over a half sphere with a radius of 25 meters positioned on the lunar soil for the Moon surface scenarios (scenarios number 1-4), reproduced in Figure 6.7.

For the deep space simulation (scenario number 5), a 13 meters sphere has instead been used, reproduced in Figure 6.8.

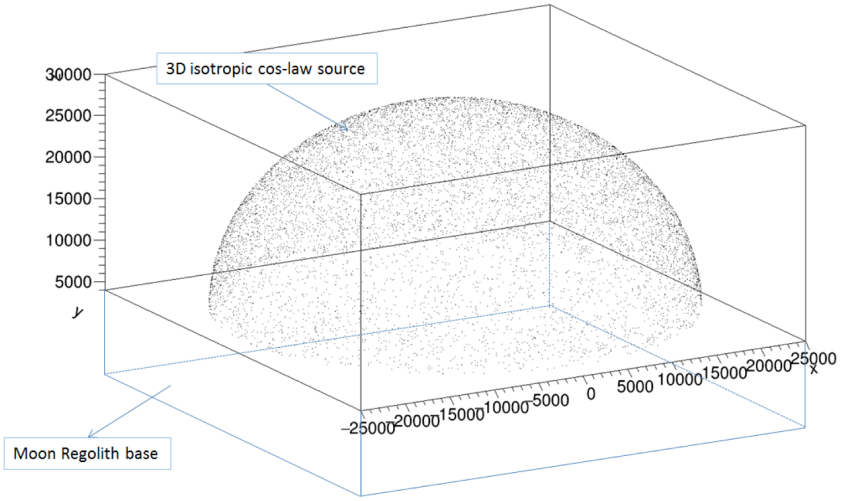

Fig. 6.7 Monte Carlo simulation source geometry, obtained plotting the x,y,z coordinates of the generation point through ROOT data analysis framework [9] - Moon surface scenario (1-4).

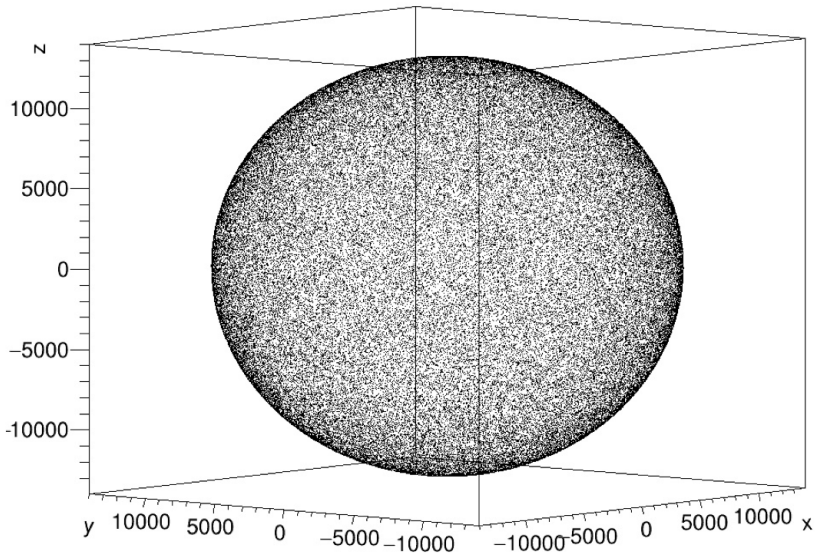

Fig. 6.8 Monte Carlo simulation source geometry, obtained plotting the x,y,z coordinates of the generation point through ROOT data analysis framework [9] – deep space scenario 5.

No natural occurring radioactivity has been considered in this work, due to the fact that the dose due to radionuclides present on the moon would be less than 1% of the dose delivered by cosmic rays [36].

GCR source

The reference mission scenario used here is the same used in Chapter 4, a deep space trip during a solar minimum period, characterized by a higher flux of GCRs than solar maximum.

All the ions with atomic numbers ranging from 1 to 26 have been considered in the calculation using the ISO model 15390 [28] (suggested by ECCS 10-04 standard as reference GCR model) at solar minimum without magnetic cut-off to consider the worst case situation, up to energies of 10^5 GeV/nuc.

Figure 4.8 shows the energy spectra used in the simulations for a subset of considered ions.

SPE source

SPEs are mainly composed by protons, and the work done in the framework of this thesis has considered only the proton component.

The August 1972 event has been chosen as it was one of the worst case event in terms of released dose to the crew for a typical spacecraft shielding (1-10 mm), where particles of energy 10-70 MeV were important. During this event a peak flux near the Earth in excess of 10^6 $protons\ cm^{-2}\ s^{-1}$ above 10 MeV was recorded.

No heavy nuclei have been considered, being their influence negligible compared to GCRs [80].

Secondary radiation

The secondary radiation is the one induced by electromagnetic and nuclear interactions of GCRs and SPEs with the moon soil and habitat structures. Charged particles get absorbed, produce fragments and new species while interacting with the traversed matter. Several kinds of reactions take place and neutrons and photons are the main reaction products, able to give rise to additional secondary particles.

6.1.4 Physics list selection

Neutron production comparisons have been made, simulating with different physics lists GCR interactions with Moon Soil. QBBC-EMY has been selected, with high precision electromagnetic physics and alternative cross-section and final-state models (similar to but faster than the neutron high precision physics lists)for neutron capture.

Binary Cascade model, followed by Precompound and de-excitation, is used below 1.5 GeV to calculate the final-state model of proton- and neutron-nucleus inelastic interactions, while the Bertini one is used between 1GeV and 5GeV.

6.1.5 Simulations endpoints and dose calculations

One option to proceed with the simulation is to insert a phantom model inside the habitat, possibly in different positions and orientations, and then to calculate the dose in each organ and tissue. It is straightforward to understand that to reach enough statistics in the smaller organs, huge computational time is needed.

However, considering that inside a spacecraft the astronaut crew is moving around, changing his/her orientation many times during a day (we are not considering a situation in which the astronaut is sleeping in a sleeping quarter), in a first instance an isotropic exposure can be hypothesized.

Therefore, instead of inserting a phantom inside the habitat, an alternative approach was chosen, i.e. fluence to dose conversion factors have been applied. Specifically, air sphere volumes of radius 1 meter have been inserted inside the habitat geometry (Figures 6.5 and 6.6) and particle fluence crossing their surfaces has been dumped to root histograms, expressed as number of particles. Once the simulation is over and the average fluence on the surface of the sphere has been obtained, the analysis process is composed by the following steps. Initially fluence is converted to relative organ doses for each energy interval and each particle, applying the fluence-to-dose conversion coefficients (expressed in $pGy\ cm^2$), as given in ICRP123 Publication [48]. Calculation of the total equivalent dose is then performed, summing over all the energy bins, for each organ and each particle involved for the assessment of organ doses. Finally, calculation of total effective dose is made for sex averaged case (dose averaged over a male and a female phantom) and a normalization follows, function of the desired output.

More in detail, the simulations give the fluence spectra of the particles reaching the considered volumes (the air spheres) as outputs. In particular, the recorded quantity in the root histograms is the number of particles per energy bin

$$N^E \tag{6.1}$$

and this value is then divided by the cross sectional area of the reference sphere, πr^2, with r the sphere radius:

$$\phi^E = \frac{1}{\pi r^2} N^E \tag{6.2}$$

where E refers to each energy bin.

The so obtained fluence, expressed as $particles/MeV/cm^2$, has to be convoluted by the fluence-to-dose conversion factor, available in $pGy * cm^2$ and varying with energy, and then the results of this operation (in pGy/MeV) must be integrated over the energy (to obtain the mean absorbed dose, defined below). If instead the user desires to obtain ICRP or NASA equivalent dose, before integrating over energy, an additional step is necessary, i.e. the multiplication by the corresponding quality factor.

The simulated dose equivalent for a tissue or organ T is obtained using the quality factor Q and the fluence to dose conversion coefficients, as in Equation 6.2 (for Male or Female).

$$H^{sim}_{T,Q} = \sum_R \sum_E h^E_{T,R,Q} \varphi^E = \sum_R \sum_E Q^E_{T,R} d^E_{T,R} \varphi^E \tag{6.3}$$

where $Q^E_{T,R}$ is the NASA/ICRP quality factor of the particle R having energy E in a tissue or organ T, and $d^E_{T,R}$ is the corresponding fluence to dose conversion coefficient expressed in $pGy * cm^2/MeV$. The mean absorbed dose in the tissue/organ T is calculated in the following way:

$$D^{sim}_T = \sum_R \sum_E d^E_{T,R} \varphi^E . \tag{6.4}$$

Finally, whole body dose can be obtained summing all the contributions for each organ and tissue.

6.1.6 Normalization of the results

As already explained, being the GCR spectrum reaching the habitat isotropic in direction, particles have been generated over a sphere (or half a sphere for the surface scenario) with an inward direction and with cosine law. Being our goal to obtain doses and effective dose over a period of time (i.e. a year, a day), we need to multiply the dose obtained with Equation 6.4 by an additional normalization factor, able to transform the "simulated" fluence into the "real" fluence (or flux), ϕ, we could actually measure in space. We therefore have to consider the number of particle, N_{real}, which would cross the source sphere (or half a sphere) of surface S and radius R in the real world.

Being the quantities dumped to histogram from the simulation referred to the number of simulated primaries, we also need to divide the obtained fluence by the number of simulated particles, N_{sim}, to obtain the fluence per primary. We can now link the fluence of particle per simulated primary to the number of primary particles found in space in a real situation over a certain period of time, to obtain the overall fluence in that period of time, and therefore, the dose.

Summarizing all these considerations we obtain the following expression for the normalization factor, f_n, (for a spherical source):

$$f_n = \frac{N_{real}}{N_{sim}} = \frac{S\phi}{N_{sim}} = \frac{\pi R^2 \phi}{N_{sim}} \tag{6.5}$$

where ϕ is here expressed in $cm^{-2}s{-}1$

Finally, the normalized dose equivalent and mean absorbed dose become:

$$H_{T,Q} = f_n H_{T,Q}^{sim} = \frac{\pi R^2 \phi}{N_{sim}} \sum_R \sum_E Q_{T,R}^E d_{T,R}^E \varphi^E \tag{6.6}$$

$$D_T = f_n D_T^{sim} = \frac{\pi R^2 \phi}{N_{sim}} \sum_R \sum_E d_{T,R}^E \varphi^E. \tag{6.7}$$

ICRP 123 factors are given for female and male phantoms, to obtain the sex-averaged effective dose, the mean is calculated between the male and female total body doses.

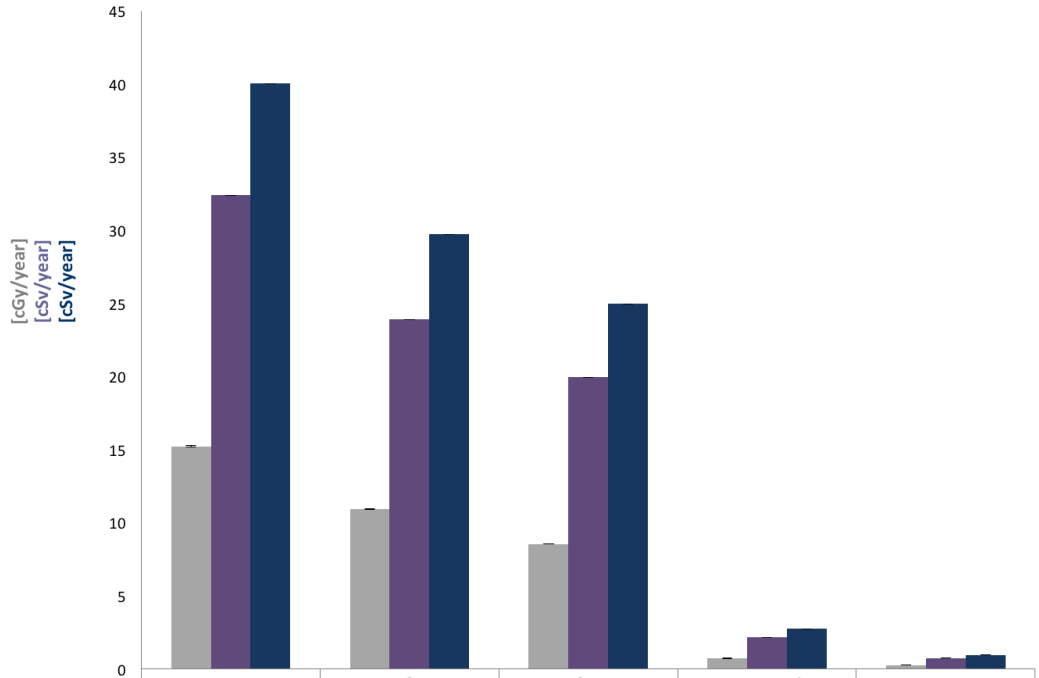

	Deep-space	Surface	Surf-Bags	Moon-only	MH1
Dose [cGy/year]	15,23	10,94	8,55	0,73	0,26
ICRP [cSv/year]	32,41	23,91	19,94	2,16	0,74
NASA [cSv/year]	40,03	29,72	24,96	2,75	0,96

Fig. 6.9 GCR whole spectrum: effective dose and dose equivalent (evaluated using the ICRP and NASA quality factors), where MH1 refers to the base Moon Habitat model, underneath the Moon soil. Simulation error bars are partially hidden.

6.2 Results

Air spheres of 1 meter of radius have been place inside the habitat, as can be seen in Figure 6.5, and particle fluence has been calculated over their surface.

In Figure 6.9 the total effective dose expressed in Gy and in Sv is given as sex averaged and using both NASA and ICRP quality factors, for each exposure scenarios.

GCR exposure results in an effective dose of about 40 cSv per year when a deep space exposure is considered.

In a moon habitat scenario with a 3D printed cupola of moon concrete surrounding the structures, the crew will be protected from radiation for long-duration missions. Instead, in deep space, even with a heavily shielding spacecraft (the habitat taken in consideration in this work is providing from every direction a protection of

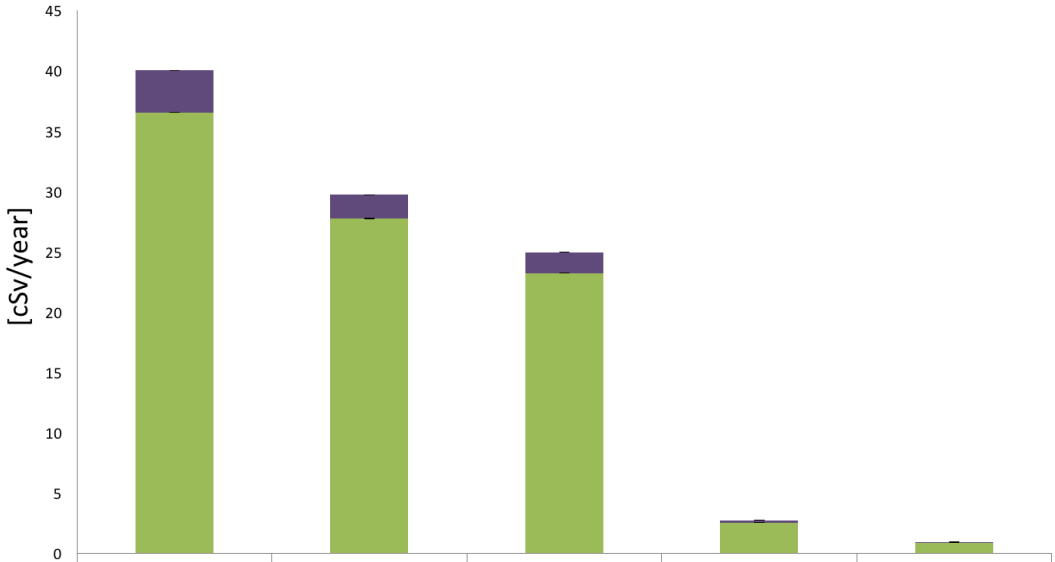

	Deep-space	Surface	Surf-Bags	Moon-only	MH1
HZE	3,489	1,973	1,728	0,212	0,073
H-He	36,54	27,75	23,24	2,54	0,88

Fig. 6.10 Contribution of the primary GCR particles (H, He and HZE) to the total effective dose calculated through NASA quality factors, where MH1 refers to the base Moon Habitat model, underneath the Moon soil. Simulation error bars are partially hidden.

at least 30 g/cm^2 of aluminum equivalent) we can see how the radiation exposure approaches values close to the limits existing in LEO. It is interesting to see that when passing from the "Moon-only" to the "MH1" scenario, therefore when adding the habitat structures and internal systems, dose is slightly decreasing, mostly because of the large amount of water present on the top of the habitat, which is absorbing neutrons produced in the soil.

Contribution of the primary GCR particles to the total effective dose calculated through NASA quality factors is divided between H and He ions and HZE ions in Figure 6.10. It is possible to see how the last contribution decreases when the amount of material around the pressurized volume is increased. HZE have low impact on the effective dose and this is mainly due to the fact that a heavy shielded situation is considered in this work.

Finally, for each scenario, the percentage of dose deposited by different particles is shown in Figures 6.11 and 6.12, distinguishing between dose deposited by protons, alpha, gamma, pions, neutrons and heavy ions.

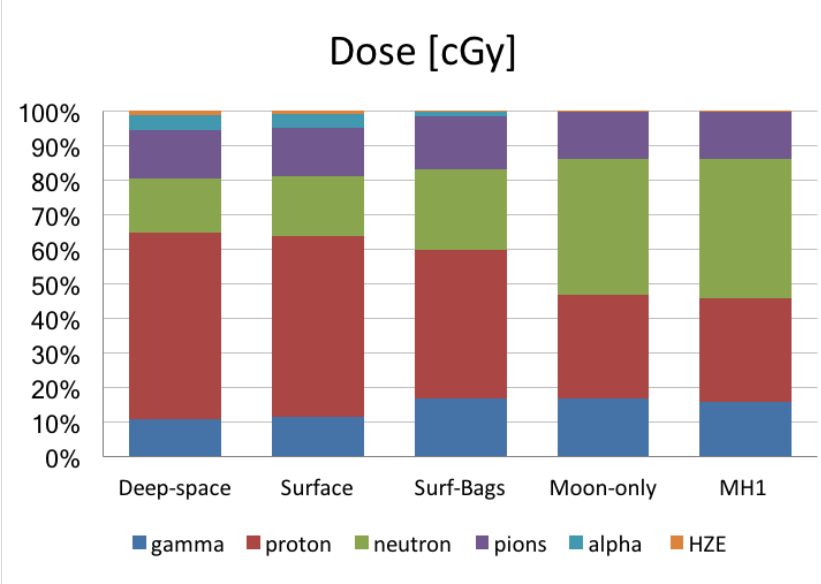

Fig. 6.11 Contribution of the primary GCRs (divided in gamma, protons, neutrons, pions and HZE) to the total effective dose calculated through ICRP 123 fluence to dose conversion factors and expressed in cGy. Simulation errors are not shown as they are less than 1%.

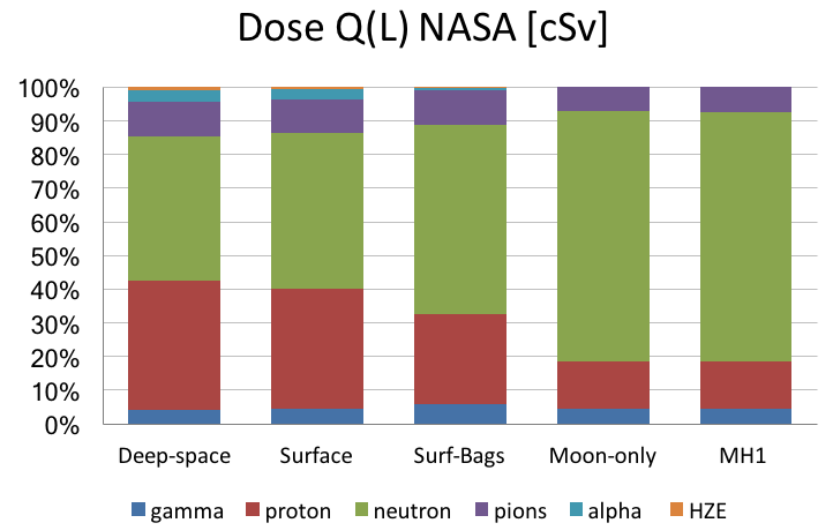

Fig. 6.12 Contribution of the primary GCRs (divided in gamma, protons, neutrons, pions and HZE) to the total effective dose equivalent (in cSv) calculated through ICRP 123 fluence to dose conversion factors and then applying NASA quality factors. Simulation errors are not shown as they are less than 1%.

With increasing thickness the neutron contribution to the equivalent dose increases. Dose deposited directly by heavy ions is significantly decreasing with thickness.

An important consideration to do on the simulation results is that the total effective sex-average dose errors could be slightly underestimated when treated in this way: doses are indeed calculated using the fluence to dose conversion coefficients defined in ICRP 123 publication, which are tabulated without any information on the simulation errors. This could be significant in error analysis. On the other hand, calculating fluence over a spherical volume, instead than in very small phantom tissues and organs, allowed us to achieve reasonable simulations time, making this approach the best for our work. Nevertheless, to deal with the unknown ICRP coefficient errors, our error analysis has been conservatively carried out.

Chapter 7

Conclusions and future works

Radiation risk is one of the main showstopper to deep space exploration: missions that will take place outside Earth's magnetic field and atmosphere protection, will be subjected to an increase risk of radiation-induced detrimental effects for the crew.

Knowledge of the secondary radiation field inside future spacecraft will be therefore essential to determine the astronauts' radiation exposure and to protect them during future long duration deep space missions.

In the framework of this work, some shielding materials have been reviewed, selected and tested. Simulations have been carried out to investigate Monte Carlo codes ability to provide a reliable radiation risk prediction and, finally, crew radiation exposure in a Moon exploration mission has been assessed in different scenarios.

Based on the results of radiation tests and simulations, in the following sections recommendations and learned lessons are provided for future research topics about future radiation test campaigns, innovative materials and structures and Monte Carlo simulations.

7.1 Recommendations for future research work

7.1.1 Material selection

Properly selecting radiation shielding materials and trying to optimize their arrangement outside and inside the spacecraft/habitat is the principal available countermeasures for both GCRs and SPEs.

Considering the work done during the ROSSINI2 study, hydrides seems so far to be the only materials able to drastically reduce the radiation dose inside a habitat. Of course a lot of work needs to be done to design and further characterize them, possibly using as a starting point LiH, as pointed out from the ROSSINI2 study.

In fact, among the material types included in our investigation, from a radiation protection prospective, LiH represents the best option for in-flight habitats when the radiation shielding properties are considered. It is indeed the only studied material able to guarantee an increased dose reduction and beam fragmentation compared to all the others. However, unfortunately LiH is unsafe to be used as it is found in its natural state. It is an easily flammable dust when placed in contact with moistures, moreover it does not possess mechanical properties requested in the space field.

An idea could be to include LiH inside polymers, as filler material, possibly able to strength the polymer matrix and leading to composites with increased hydrogen content. As a result, the new material may have improved mechanical and radiation shielding properties due to the combination of filler and polymer matrix. Of course, in this case, further studies would be needed to investigate the so-obtained material behavior under intense radiation fields, verifying the swelling behavior of LiH and eventual hydrogen dispersion.

Possible partners for this investigation can be found in universities and laboratories working on hydrogen storage materials for automotive transport and stationary applications.

Possibly, the so identified hydrides, eventually coupled with polymeric materials in multilayer configurations, could be included in the future not only as shielding materials when designing deep space habitat and exploration vehicles, but also as flexible layers inside EVA suits, to provide the astronaut with increased protection from SPEs.

A part from hydrides, as a general guideline, materials containing carbon are recommended to be used in the spacecraft design instead of Aluminum. They should be used as primary and secondary structure materials when possible and, also, internal spacecraft outfitting should be made with polymers instead of metals. The lighter nuclei characterizing polymers have in fact fewer neutrons to release and in particular carbon nuclei can break into three helium nuclei without releasing any neutrons at all. This of course has a beneficial effect on the secondary radiation field created inside a habitat. Moreover, it has been proved that Aluminum alloys used in space have even worse shielding properties than pure Aluminum, leading to a more detrimental radiation field.

Dual-use and multi-purpose shielding approaches, i.e. using water, fuel, food and waste stowage for shielding purposes should be investigated in realistic architectures, as it has been preliminary done for the Moon habitat design. Also storm shelter on boards can be optimized following this approach, trying to use materials already-present in the spacecraft to achieve a better radiation protection during emergency situations but also in the everyday life. For instance, crew sleeping quarters should be designed as storm shelters, so that when astronauts are sleeping they are more protected.

The creation of suits which can be temporarily inflated with service water in case of necessity, or to be worn when the astronauts are sleeping, is another possible way to achieve a better astronaut's protection.

ISRU materials, such as Moon regolith and Moon concrete, have been proved to be good candidates as radiation shielding when considering planetary scenarios. In particular, they are behaving better than aluminum from a radiation protection prospective. In order to employ them in realistic exploration situations, the use of 3D printers to produce large structures for shielding purposes using ISRU materials should be further studied in a relevant environment, subjected to vacuum conditions, lower gravity and massive thermal excursions. The ability to 3D print lunar and martian soils would permit taking smaller amounts of materials in a journey to an outpost on another space body, using the resources already present on the destinations. A possibility could include the use of solar energy to power a laser sintering machine. For instance, Powder Bed Fusion (PBF) could be employed. They are advanced manufacturing technologies that can fabricate three-dimensional assets from CAD data, layer-by-layer by using thermal energy from a laser source.

Neutron shielding on satellites and planetary surface via ISRU or specific adsorbers (e.g. Boron launched from Earth and added to Moon regoliths) should be investigated, together with enabling technologies.

Finally, what we have already known, but further verified with the ROSSINI2 study, is in fact that every material/structure inside a habitat is contributing to the final secondary radiation field, therefore to the radiation risk to the crew. Lower exposure cannot be achieved only adding some shielding materials some places inside the habitat, but there must be a general design guideline, characterizing everything which comes inside the space structures.

7.1.2 Radiation tests

The experimental campaigns performed in this study confirmed that every candidate as shielding material or configurations should be tested with at least two beams with different characteristics as those selected in this study, before evaluating its ability to shield GCRs.

The results of the study indicate indeed that some materials with good shielding effectiveness against some beams, perform very poorly when irradiated with others. For instance, the majority of the irradiated materials providing a positive dose reduction when hit by heavy ion beams, were instead leading to an increase of the dose after the target when exposed to high energy alpha particles. Moreover, dose reduction alone does not represent the optimal approach for assessing the best material and thickness, but should be coupled with at least beam fragmentation or microdosimetry data to take into account also the quality of the radiation field behind the shield. Neutron production and beam fragmentation results, even if very expansive to obtain, are very useful to investigate the beam vs target behavior and also allows investigating the source of possible simulations disagreements.

Data analysis of the beam fragmentation tests made in ROSSINI2 is still on-going and will be the subject of a future dedicated publication.

The database of atomic, nuclear and particle interaction cross sections is fundamental to be able to simulate future exposure scenarios and it will have to be continuously updated, to accurately carry on transport simulations, decreasing important sources of design margins.

In particular, fragmentation studies of high-energy projectiles on targets based on different kinds of materials are fundamental, prioritizing relativistic protons and alpha particles, with high penetration power and high angular spread. Other dominant Galactic Cosmic Rays species, such as Carbon, Oxygen and Silicon ions, should be considered, too, together with experiments on the target-fragment build-up issue.

Future works should at first carry out an analysis of new literature data to identify high priority combinations of projectiles and targets, among the least known ones. After that, as in the past ROSSINI studies, some new targets will be procured, facility/facilities identified and a test plan will be produced and evaluated.

In parallel, Monte Carlo simulations and benchmarking campaigns for radiation shielding materials interaction with test beams will be performed using different MC codes; the experimental set-up will be simulated and results will be compared against experimental data.

7.1.3 3D Monte Carlo simulations

The work done in the ROSSINI2 study on 3D habitat and spacecraft simulations focused on highly shielded habitat configurations. In future, other habitats will be studied, with intermediate weights between the ones here considered, iterating with different material configurations. Different mission scenarios, such as a space station in a Lagrangian point or Mars surface exploration, could be considered, too.

Monte Carlo simulations of EVA and Intra Vehicular Activities (IVA) suits should be performed in the future, to determine hourly and daily radiation exposures of astronauts involved in a spacewalk or a planetary exploration mission, in operative conditions but also for emergency situations (such as SPEs).

Considering the cis-lunar missions planned in the next future, iterations should be made on different shielding options of the latest habitat design, considering different SPEs and GCRs models.

The creation of a “geometrical models database” compatible with Monte Carlo simulations should be considered. In particular, modeling variable space geometries (e.g. visiting vehicles, movable heavy items, spacecraft parts) could provide easy access to end-users looking for modular volumes to insert in their simulations, at the same time allowing the creation of a uniform and comparable results record.

Guidelines on SPE and GCR spectra to be used would also provide data to be easily benchmarked between different users.

List of Acronyms

AHP Analytic Hierarchy Process

Al2024 Aluminium 2024

ALARA As Low as Reasonably Achievable

ANMAC Active Nanostructured Magnetic Attenuation Composite

ARS Acute Radiation Syndrome

BIC BInary Cascade Model

BNL Brookhaven National Laboratory

BFO Blood Forming Organs

CFRP Carbon fiber–reinforced plastic

CG Combinational Geometry

CL Confidence Level

CME Coronal Mass Ejections

CNS Central Nervous System

EM ElectroMagnetic

ESA European Space Agency

ESP Emission of Solar Protons

EVA Extra Vehicular Activities

FB Fermi Breakup Model

FWHM Full Width at Half Maximum

GCRs Galactic Cosmic Rays

GDML Geometry Description Markup Language

Geant4 GEometry ANd Tracking

GG General Geometry

GRAS Geant4 Radiation Analysis in Space

GSI Gesellschaft für Schwerionenforschung

GUI Graphical User Interface

HDPE High Density PolyethylenE

HIT Heidelberg Ion-Beam Therapy Center

HZE High Z number and high Energy

IC Ionization Chamber

ICRP International Committee of Radiation Protection

ISS International Space Station

ISRU In Situ Re Utilization

IVA Intra Vehicular Activities

JSC Johnson Space Center

JUICE JUpiter ICy moons Explorer

LEO Low Earth Orbit

LET Linear Energy Transfer

LSS Life Span Studies

MDPS Micrometeoroid and Orbital Debris Protection Systems

MH Moon Habitat

MSL Mars Science Laboratory

NASA National Aeronautics and Space Administration

NEO Near Earth Orbit

NIEL Non Ionizing Energy Loss

NSRL NASA Space Radiation Laboratory

PBI PolyBenzimIdazole

PDF Probability Density Function

PE Polyethylene

PHITS Particle and Heavy Ion Transport code System

PMMA Poly(methyl methacrylate)

PPSU Polyphenylsulfone

PTFE Polytetrafluoroethylene

PU PolyUrethane

RAD Radiation Assessment Detector

RBE Relative Biological Effectiveness

REID Risk of Exposure Induced Death

REMSIM Radiation Exposure and Mission Strategies for Interplanetary Manned

SAA South Atlantic Anomaly

SMF Statistical MultiFragmentation Model

SPEs Solar Particle Events

TEPC Tissue Equivalent Proportional Chamber

TE Tissue Equivalent

TID Total Ionizing Dose

TIFPA Trento Institute for Fundamentals Physics Applications

TOF Time Of Flight

UNITO University of Turin

References

[1] John W Wilson, F.A Cucinotta, J.L Shinn, L.C Simonsen, R.R Dubey, W.R Jordan, T.D Jones, C.K Chang, and M.Y Kim. Shielding from solar particle event exposures in deep space. *Radiation Measurements*, 30(3):361 – 382, 1999.

[2] Hermann J. Schaefer. Radiation and man in space. In Frederick I. Ordway, editor, *Advances in Space Science*, pages 267 – 339. Academic Press, 1959.

[3] J. A. Simpson. Elemental and Isotopic Composition of the Galactic Cosmic Rays. *Annual Review of Nuclear and Particle Science*, 33:323–382, 1983.

[4] Francis A Cucinotta and Marco Durante. Cancer risk from exposure to galactic cosmic rays: implications for space exploration by human beings. *The Lancet Oncology*, 7(5):431 – 435, 2006.

[5] Tatsuhiko Sato, Akira Endo, and Koji Niita. Fluence-to-dose conversion coefficients for heavy ions calculated using the phits code and the icrp/icru adult reference computational phantoms. *Physics in Medicine Biology*, 55(8):2235, 2010.

[6] T. Sato, A. Endo, and K. Niita. Comparison of the mean quality factors for astronauts calculated using the q-functions proposed by icrp, icru, and nasa. *Advances in Space Research*, 52(1):79 – 85, 2013.

[7] Francis A. Cucinotta, Murat Alp, Blake Rowedder, and Myung-Hee Y. Kim. Safe days in space with acceptable uncertainty from space radiation exposure. *Life Sciences in Space Research*, 5:31 – 38, 2015.

[8] http://geant4.cern.ch/.

[9] R. Brun and F. Rademakers. ROOT: An object oriented data analysis framework. *Nucl. Instrum. Meth.*, A389:81–86, 1997.

[10] A.C. Tribble. *The Space Environment: Implications for Spacecraft Design*. Princeton University Press, 1995.

[11] D. Sawyer and J. Vette. Ap-8 trapped proton environment for solar maximum and solar minimum. *National Space Science Data Center*, Report 76-06, 1976.

[12] D. H. Brautigam and J. T. Bell. Crresele documentation. *Environmental Research Papers, Phillips Lab., Hanscom Air Force Base, Mass.*, PL-TR-95-2128(4):1178, 1995.

[13] A. S. Piet, S. Bourdarie, D. Boscher, and R. H. W. Friedel. A model for the geostationary electron environment: Pole, from 30 kev to 5.2 mev. *IEEE Transactions on Nuclear Science*, 53(4):1844–1850, 2006.

[14] Sicard-Piet A., Bourdarie S., Boscher D., Friedel R. H. W., Thomsen M., Goka T., Matsumoto H., and H. Koshiishi. A new international geostationary electron model: Ige-2006, from 1 kev to 5.2 mev. *Space Weather*, 6(7):n/a–n/a, 2008. S07003.

[15] G. P. Ginet, T. P. O'Brien, S. L. Huston, W. R. Johnston, T. B. Guild, R. Friedel, C. D. Lindstrom, C. J. Roth, P. Whelan, R. A. Quinn, D. Madden, S. Morley, and Yi-Jiun Su. Ae9, ap9 and spm: New models for specifying the trapped energetic particle and space plasma environment. *Space Science Reviews*, 179(1):579–615, 2013.

[16] J. D. Meffert and M. S. Gussenhoven. Crrespro documentation. *Environmental Research Papers, Phillips Lab., Hanscom Air Force Base, Mass.*, PL-TR-94-2218(4):1558, 1994.

[17] D. Heynderickx, M. Kruglanski, V. Pierrard, J. Lemaire, M. D. Looper, and J. B. Blake. A low altitude trapped proton model for solar minimum conditions based on sampex/pet data. *IEEE Transactions on Nuclear Science*, 46(6):1475–1480, 1999.

[18] M.V. Podzolko, I.V. Getselev, Yu.I. Gubar, I.S. Veselovsky, and A.A. Sukhanov. Charged particles on the earth–jupiter–europa spacecraft trajectory. *Advances in Space Research*, 48(4):651 – 660, 2011. Europa Lander: Science Goals and Implementation.

[19] O. Grasset, M.K. Dougherty, A. Coustenis, E.J. Bunce, C. Erd, D. Titov, M. Blanc, A. Coates, P. Drossart, L.N. Fletcher, H. Hussmann, R. Jaumann, N. Krupp, J.-P. Lebreton, O. Prieto-Ballesteros, P. Tortora, F. Tosi, and T. Van Hoolst. Jupiter icy moons explorer (juice): An esa mission to orbit ganymede and to characterise the jupiter system. *Planetary and Space Science*, 78:1 – 21, 2013.

[20] R.K. Tripathi, J.W. Wilson, F.F. Badavi, and G. De Angelis. A characterization of the moon radiation environment for radiation analysis. *Advances in Space Research*, 37(9):1749 – 1758, 2006. Space Life Sciences: Flight Measurements, Calibration of Detectors and Environmental Models for Radiation Analysis.

[21] L.W. Townsend, J.A. Porter, W.C deWet, W.J. Smith, N.A. McGirl, L.H. Heilbronn, and H.M. Moussa. Extreme solar event of ad775: Potential radiation exposure to crews in deep space. *Acta Astronautica*, 123:116 – 120, 2016. Special Section: Selected Papers from the International Workshop on Satellite Constellations and Formation Flying 2015.

[22] I. G. Usoskin, B.Kromer, F.Ludlow, J. Beer, M. Friedrich, G.A.Kovaltsov, S. K. Solanki, and L. Wacker. The ad775 cosmic event revisited: the sun is to blame. *Astronomy and Astrophysics*, 552:L3, 2013.

[23] L. J. Gleeson and W. I. Axford. Solar modulation of galactic cosmic ray. *Astrophysical Journal*, 1968.

[24] J.F. Valdés-Galicia and L.X. González. Solar modulation of low energy galactic cosmic rays in the near-earth space environment. *Advances in Space Research*, 57(6):1294 – 1306, 2016. Space and Geophysical Research related to Latin America - Part I.

[25] Z. Fujii and Frank B. McDonald. The radial intensity gradients of galactic and anomalous cosmic rays. *Advances in Space Research*, 23(3):437 – 441, 1999. The Transport of Galactic and Anomalous Cosmic Rays in the Heliosphere: Observations, Simulations and Theory.

[26] NCRP (National Council on Radiation Protection and Measurements). *Information Needed to Make Radiation Protection Recommendations for Space Missions Beyond Low-Earth Orbit*. 2006.

[27] A. J. Tylka, J. H. Adams, P. R. Boberg, and et al. Creme96: A revision of the cosmic ray effects on micro-electronics code. *IEEE Transactions on Nuclear Science*, 44:2150–2160, 1997.

[28] SPENVIS. https://www.spenvis.oma.be.

[29] Takashi Nakamura and Lawrence Heilbronn. Overview of secondary particle production and transport by high-energy heavy ions. *Nuclear Instruments and Methods in Physics Research Section A: Accelerators, Spectrometers, Detectors and Associated Equipment*, 562(2):706 – 709, 2006. Proceedings of the 7th International Conference on Accelerator Applications.

[30] S.K. Aghara, S.R. Blattnig, J.W. Norbury, and R.C. Singleterry. Monte carlo analysis of pion contribution to absorbed dose from galactic cosmic rays. *Nuclear Instruments and Methods in Physics Research Section B: Beam Interactions with Materials and Atoms*, 267(7):1115 – 1124, 2009.

[31] John W. Norbury, Jack Miller, Anne M. Adamczyk, Lawrence H. Heilbronn, Lawrence W. Townsend, Steve R. Blattnig, Ryan B. Norman, Stephen B. Guetersloh, and Cary J. Zeitlin. Nuclear data for space radiation. *Radiation Measurements*, 47(5):315 – 363, 2012.

[32] C. Zeitlin, D. M. Hassler, F. A. Cucinotta, B. Ehresmann, R. F. Wimmer-Schweingruber, D. E. Brinza, S. Kang, G. Weigle, S. Böttcher, E. Böhm, S. Burmeister, J. Guo, J. Köhler, C. Martin, A. Posner, S. Rafkin, and G. Reitz. Measurements of energetic particle radiation in transit to mars on the mars science laboratory. *Science*, 340(6136):1080 –1084, 2013.

[33] Francis A. Cucinotta, Hooshang Nikjoo, and Dudley T. Goodhead. The effects of delta rays on the number of particle-track traversals per cell in laboratory and space exposures. *Radiation Research*, 150(1):115–119, 1998.

[34] G. Heiken, D. Vaniman, and B. French. *Lunar sourcebook*. Cambridge University Press, 1991.

[35] N. R. Goins, A. M. Dainty, and M. N. Toksoz. Seismic Energy Release of the Moon. In *Lunar and Planetary Science Conference*, volume 11 of *Lunar and Planetary Science Conference*, pages 336–338, March 1980.

[36] Guenther Reitz, Thomas Berger, and Daniel Matthiae. Radiation exposure in the moon environment. *Planetary and Space Science*, 74(1):78 – 83, 2012. Scientific Preparations For Lunar Exploration.

[37] Yu.A. Surkov. Radioactivity of the moon and planets. *Advances in Space Research*, 1(8):21 – 38, 1981.

[38] J. Bernabeu and I. Casanova. Moon surface radiation environment analysis for february 1956 solar event conditions. *Advances in Space Research*, 42(12):1906 – 1912, 2008.

[39] NASA Mars atmosphere model. https://www.grc.nasa.gov/www/k-12/airplane/atmosmrm.html.

[40] Susan McKenna-Lawlor, P. Gonçalves, A. Keating, G. Reitz, and D. Matthiä. Overview of energetic particle hazards during prospective manned missions to mars. *Planetary and Space Science*, 63:123 – 132, 2012. Advances in Planetary Atmospheres and Exploration.

[41] L.W. Townsend, M. PourArsalan, M.I. Hall, J.A. Anderson, S. Bhatt, N. DeLauder, and A.M. Adamczyk. Estimates of carrington-class solar particle event radiation exposures on mars. *Acta Astronautica*, 69(7):397 – 405, 2011.

[42] L.W. Townsend, J.A. Anderson, A.M. Adamczyk, and C.M. Werneth. Estimates of carrington-class solar particle event radiation exposures as a function of altitude in the atmosphere of marsthis paper was presented during 62nd iac in capetown. *Acta Astronautica*, 89:189 – 194, 2013.

[43] Bent Ehresmann, Donald M. Hassler, Cary Zeitlin, Jingnan Guo, Jan Köhler, Robert F. Wimmer-Schweingruber, Jan K. Appel, David E. Brinza, Scot C.R. Rafkin, Stephan I. Böttcher, Sönke Burmeister, Henning Lohf, Cesar Martin, Eckart Böhm, Daniel Matthiä, and Günther Reitz. Charged particle spectra measured during the transit to mars with the mars science laboratory radiation assessment detector (msl/rad). *Life Sciences in Space Research*, 10:29 – 37, 2016.

[44] M. Vuolo, G. Baiocco, S. Barbieri, L. Bocchini, M. Giraudo, T. Gheysens, C. Lobascio, and A. Ottolenghi. Exploring innovative radiation shielding approaches in space: A material and design study for a wearable radiation protection spacesuit. *Life Sciences in Space Research*, 15:69 – 78, 2017.

[45] C. Leroy and P. Rancoita. *Principles of Radiation Interaction in Matter and Detection*. World Scientific Publishing Co. Pte. Ltd., 2004.

[46] H. L. Bradt and B. Peters. The Heavy Nuclei of the Primary Cosmic Radiation. *Physical Review*, 77:54–70, January 1950.

[47] L. W. Townsend and J. W. Wilson. Energy-dependent parameterization of heavy-ion absorption cross sections. *Radiation Research*, 106(3):283–287, 1986.

[48] G. Dietze, D.T. Bartlett, D.A. Cool, F.A. Cucinotta, X. Jia, I.R. McAulay, M. Pelliccioni, V. Petrov, G. Reitz, and T. Sato. Icrp publication 123: Assessment of radiation exposure of astronauts in space. *Annals of the ICRP*, 42(4):1 – 339, 2013. ICRP PUBLICATION 123:.

[49] The 2007 Recommendations of the International Commission on Radiological Protection. *ICRP Publication 103*. Elsevier, 2007.

[50] 1990 Recommendations of the International Commission on Radiological Protection. *ICRP Publication 60*. Pergamon Press, 1991.

[51] M. Durante and F. A. Cucinotta. Physical basis of radiation protection in space travel. *Reviews of Modern Physics*, 83:1245–1281, October 2011.

[52] F.A. Cucinotta, M.Y. Kim, and L. Chappel. Space radiation cancer risk projections and uncertainties. Technical report, NASA, 2013.

[53] Ann R. Kennedy. Biological effects of space radiation and development of effective countermeasures. *Life Sciences in Space Research*, 1:10 – 43, 2014.

[54] Francis A. Cucinotta, Khiet To, and Eliedonna Cacao. Predictions of space radiation fatality risk for exploration missions. *Life Sciences in Space Research*, 13:1 – 11, 2017.

[55] Tingting Liu, Dan Xu, He Li, Hailong Pei, Mingyue Zhu, Jufang Wang, and Guangming Zhou. Risk assessment of space radiation during manned space flights. *Rendiconti Lincei*, 25(1):17–21, Mar 2014.

[56] Thomas Saaty. Decision making with the analytic hierarchy process. *Int. J. Services Sciences Int. J. Services Sciences*, 1:83–98, 01 2008.

[57] ESA TRL Definition. http://sci.esa.int/sci-ft/50124-technology-readiness-level/.

[58] S. Bennington, S. Mcgrady, D. Royse, A. Lovell, L. Mooring, and T. Headen. Hydrogen storage pellet, 2014.

[59] C. Lobascio, M. Briccarell, R. Destefanis, M. Faraud, G Gialanella, G. Grossi, V. Guarnieri, L. Manti, M. Pugliese, A. Rusek, P. Scampoli, and M. Durante. Accelerator-based tests of radiation shielding properties of materials used in human space infrastructures. *Health Physics*, 2008.

[60] G. Cesaretti, E. Dini, X. De Kestelier, V. Colla, and L. Pambaguian. Building components for an outpost on the lunar soil by means of a novel 3d printing technology. *Acta Astronautica*, 2014.

[61] G. Vekinis. "composite material for protection against cosmic rays and other high energy charged particles. *Patent application GR 201101000595*, October 2011.

[62] S. Agostinelli, J. Allison, K. Amako, J. Apostolakis, H. Araujo, P. Arce, M. Asai, D. Axen, S. Banerjee, G. Barrand, F. Behner, L. Bellagamba, J. Boudreau, L. Broglia, A. Brunengo, H. Burkhardt, S. Chauvie, J. Chuma, R. Chytracek, G. Cooperman, G. Cosmo, P. Degtyarenko, A. Dell'Acqua, G. Depaola, D. Dietrich, R. Enami, A. Feliciello, C. Ferguson, H. Fesefeldt, G. Folger, F. Foppiano, A. Forti, S. Garelli, S. Giani, R. Giannitrapani, D. Gibin, J.J. Gómez Cadenas, I. González, G. Gracia Abril, G. Greeniaus, W. Greiner, V. Grichine, A. Grossheim, S. Guatelli, P. Gumplinger, R. Hamatsu, K. Hashimoto, H. Hasui, A. Heikkinen, A. Howard, V. Ivanchenko, A. Johnson, F.W. Jones, J. Kallenbach, N. Kanaya, M. Kawabata, Y. Kawabata, M. Kawaguti, S. Kelner, P. Kent, A. Kimura, T. Kodama, R. Kokoulin, M. Kossov, H. Kurashige, E. Lamanna, T. Lampén, V. Lara, V. Lefebure, F. Lei, M. Liendl, W. Lockman, F. Longo, S. Magni, M. Maire, E. Medernach, K. Minamimoto, P. Mora de Freitas, Y. Morita, K. Murakami, M. Nagamatu, R. Nartallo, P. Nieminen, T. Nishimura, K. Ohtsubo, M. Okamura, S. O'Neale, Y. Oohata, K. Paech, J. Perl, A. Pfeiffer, M.G. Pia, F. Ranjard, A. Rybin, S. Sadilov, E. Di Salvo, G. Santin, T. Sasaki, N. Savvas, Y. Sawada, S. Scherer, S. Sei, V. Sirotenko, D. Smith, N. Starkov, H. Stoecker, J. Sulkimo, M. Takahata, S. Tanaka, E. Tcherniaev, E. Safai Tehrani, M. Tropeano, P. Truscott, H. Uno, L. Urban, P. Urban, M. Verderi, A. Walkden, W. Wander, H. Weber, J.P. Wellisch, T. Wenaus, D.C. Williams, D. Wright, T. Yamada, H. Yoshida, and D. Zschiesche. Geant4—a simulation toolkit. *Nuclear Instruments and Methods in Physics Research Section A: Accelerators, Spectrometers, Detectors and Associated Equipment*, 506(3):250 – 303, 2003.

[63] Tatsuhiko Sato, Koji Niita, Norihiro Matsuda, Shintaro Hashimoto, Yosuke Iwamoto, Takuya Furuta, Shusaku Noda, Tatsuhiko Ogawa, Hiroshi Iwase, Hiroshi Nakashima, Tokio Fukahori, Keisuke Okumura, Tetsuya Kai, Satoshi Chiba, and Lembit Sihver. Overview of particle and heavy ion transport code system phits. *Annals of Nuclear Energy*, 82:110 – 115, 2015. Joint International Conference on Supercomputing in Nuclear Applications and Monte Carlo 2013, SNA + MC 2013. Pluri- and Trans-disciplinarity, Towards New Modeling and Numerical Simulation Paradigms.

[64] M Kalos and P. Whitlock. *Monte Carlo Methods*. WILEY-VCH Verlag GnibH and Co. KCiaA. Weinheini, 2004.

[65] http://space-env.esa.int/index.php/geant4-radiation-analysis-for-space.html.

[66] G. Santin, V. Ivanchenko, H. Evans, P. Nieminen, and E. Daly. Gras: a general-purpose 3-d modular simulation tool for space environment effects analysis. *IEEE Transactions on Nuclear Science*, 52(6):2294–2299, Dec 2005.

[67] R. Chytracek, J. Mccormick, W. Pokorski, and G. Santin. Geometry description markup language for physics simulation and analysis applications. *IEEE Transactions on Nuclear Science*, 53(5):2892–2896, Oct 2006.

[68] Ashavani Kumar, Summit Jalota, and Renu Gupta. Simulation of depth–dose distributions for various ions in polyethylene medium. *Advances in Space Research*, 49(12):1691 – 1697, 2012.

[69] http://PHITS.jaea.go.jp/.

[70] Koji Niita, Hiroshi Takada, Shin ichiro Meigo, and Yujiro Ikeda. High-energy particle transport code nmtc/jam. *Nuclear Instruments and Methods in Physics Research Section B: Beam Interactions with Materials and Atoms*, 184(3):406 – 420, 2001.

[71] http://simplegeo.web.cern.ch/.

[72] Xapsos M. A., J.L. Barth, E.G. Stassinopoulos, E.A. Burke, and G.B. Gee. Space environment effects: Model for emission of solar protons (esp) – cumulative and worst-case event fluences. *NASA/TP-1999-209763*, 1999.

[73] J.H. King. Solar proton fluences for 1977-1983 space missions. *Journal of Spacecrafts and Rockets*, 11:401, 1974.

[74] Lynch G. R. and Dahl O. I. Approximations to multiple coulomb scattering. *JNucl. Instrum. Methods Phys. Res. B*, 58:6–10, 1991.

[75] G. Fehrenbacher, F. Gutermuth, E. Kozlova, T. Radon, and R. Schuetz. Neutron dose measurements with the gsi ball at high-energy accelerators. *Radiation Protection Dosimetry*, 125(1-4):209–212, 2007.

[76] L. Sihver, A. Kohama, K. Iida, K. Oyamatsu, S. Hashimoto, H. Iwase, and K. Niita. Current status of the Hybrid Kurotama model for total reaction cross sections. *Nuclear Instruments and Methods in Physics Research B*, 334:34–39, September 2014.

[77] Kei Iida, Akihisa Kohama, and Kazuhiro Oyamatsu. Formula for proton–nucleus reaction cross section at intermediate energies and its application. *Journal of the Physical Society of Japan*, 76(4):044201, 2007.

[78] Heiken G. H., Vanniman D. T., and French B. M. *Lunar Sourcebook*. Cambridge University Press, 1991.

[79] C. Cougnet, N. B. Crosby, S. Eckersley, C. Foullon, V. Guarnieri, S. Guatelli, D. Heynderickx, A. Holmes-Siedle, C. Lobascio, S. Masiello, P. Nieminen, G. Parisi, P. Parodi, M. A. Perino, M. G. Pia, R. Rampini, P. Spillantini,

V. Tamburini, and E. Tracino. Radiation exposure and mission strategies for interplanetary manned missions (remsim). *Earth, Moon, and Planets*, 94(3):279–285, Jun 2004.

[80] A.N. Denisov, N.V. Kuznetsov, R.A. Nymmik, M.I. Panasyuk, and N.M. Sobolevsky. Assessment of the radiation environment on the moon. *Acta Astronautica*, 68(9):1440 – 1447, 2011. 17th IAA Humans in Space Symposium.